TEMPORARILY COHERENT POINT SAR INTERFEROMETRY

LEI ZHANG

The thesis presented for the Degree of Doctor of Philosophy

The Hong Kong Polytechnic University

2012

The Hong Kong Polytechnic University

Department of Land Surveying and Geo-Informatics

Temporarily Coherent Point SAR Interferometry

Lei Zhang

A thesis submitted in partial fulfillment of the requirements for the degree of Doctor of Philosophy

June 2011

Declaration

Hereby I declare that I wrote this thesis myself with the help of no more than the mentioned literature and auxiliary means.

Up to now, this thesis was not published or presented to another examinations office in the same or similar shape.

Hong Kong, 2011

signature (Lei Zhang)

Abstract

Spaceborne Interferometric Synthetic Aperture Radar (InSAR) has been proven very useful in assessing remotely ground displacements. InSAR measurements have contributed to better understanding of the processes and mechanisms of geohazards such as earthquakes, volcanoes and landslides. There are two major error sources in InSAR measurements, i.e., decorrelation due to temporal and geometric effects and phase errors introduced by spatial and temporal variations of the atmosphere. The error sources can in extreme cases render the InSAR technology useless.

To reduce the errors in InSAR measurements, a relatively new technique, multi-temporal (MT) SAR interferometry, was proposed in the late 1990s. The technique has since then evolved into three categories. The first is commonly referred to as Persistent Scatterers InSAR (PSInSAR or PSI) and it deals with a time series of interferograms generated based on a single-master image. The second makes use of multi-master interferograms including the stacking analysis method and the Small BAseline Subset (SBAS) approach. The last category is an integration of the single- and multi-master interferogram analysis methods. Over the past ten years multi-temporal InSAR has been widely applied for monitoring ground deformation in urban and rural areas and for monitoring infrastructures such as dams, buildings, motorways, and pipelines. However one important limitation in current MT-InSAR methods is the difficulty in estimating correctly the phase ambiguities. Besides, the lack of methods to evaluate the accuracy of MTInSAR results when external data (e.g., levelling and GPS observations) are unavailable is also an issue of concern.

A novel InSAR data analysis method termed Temporarily Coherent Point InSAR (TCPInSAR) is proposed in the thesis. The method can estimate deformation parameters reliably by avoiding the process of phase ambiguity estimation. The method arises from the fact that for a set of **multi-**

master interferograms with short baselines, there are usually a sufficient number of arcs on which the double-difference phase components due to topographic errors and atmospheric artifacts are very small and the relative deformation rates between pairs of connected points are low. Therefore, the double-difference phase components of many such arcs are free from phase ambiguities. If only these arcs are taken as observations in estimating DEM errors and deformation rates, the complexity of parameter estimation can be reduced significantly. Included in the method are a series of innovations. To improve the density of TCPs, especially in areas with a small set of SAR images, we have developed a new TCP identification method based on offset statistics in range and azimuth directions. To make sure the selected TCPs can be connected extensively with relatively short arcs we have proposed an efficient point connection strategy that performs Delaunay triangulation locally. To retrieve the deformation rates reliably we have designed a least squares estimator with an outlier detector that can remove the arcs with phase ambiguities efficiently. To better consider the quality of individual interferograms we have improved the method of variance covariance estimation under the framework of least squares.

After validating TCPInSAR technique using simulated datasets, we have applied the TCPInSAR method to the Los Angeles basin in southern California where structurally active faults such as Newport-Inglewood fault are believed capable of generating damaging earthquakes. Both the estimated long-term average subsidence and seasonal deformation in the basin are in good agreement with GPS observations from the Southern California Integrated GPS Network (SCIGN), indicating that the TCPInSAR method is effective for the retrieval of ground motions especially in areas where abundant multi-temporal SAR data are available and dense coherent points can be isolated. To demonstrate the performance of TCPInSAR method on changing landscapes where both the persistently and partially coherent points are available, we also applied the method to the southern part of Macau which is undergoing fast redevelopment.

Acknowledgments

I would like to express sincere gratitude to my supervisor Professor Xiaoli Ding, for his constant guidance and support, without which this dissertation would not have been possible. His remarkable insight and knowledge have been pillars of strength that I could always rely on. I count myself greatly lucky to have had the opportunity to study at US Geological Survey's Cascades Volcano Obervatory (CVO) under Dr. Zhong Lu's direction for half a year. I am extremely indebted to his valuable advice and friendship. I have also very much enjoyed the time shared with him and his family.

My sincere thanks go to Professor Hyung-Sup Jung, University of Seoul, for sharing the details of his patented MAI technique and for several inspiring and joyful discussions we had during my stay at CVO. I am also grateful to Dr. Chang-Wook Lee, my office and roommate at CVO for his great help. He made my life in USA very colorful and memorable.

I deeply thank two external examiners, Professor Hui Lin at Chinese University of Hong Kong and Professor Ramon Hanssen at Delft University of Technology for their invaluable comments and suggestions. Detailed comments from Prof. Ramon Hanssen are specially appreciated, which inspired me a lot and enriched my perspectives and talks with him also gave me new insights to look at problems. I would also like to thank the chair of my oral exam committee, Professor Huseyin Baki IZ.

I wish to specially thank Dr. Bofeng Li, Curtin University of Technology for the constructive suggestions on VCE and mathematical analysis of linear model. I would like to thank all group members at the Department of Land Surveying and Geo-Informatics (LSGI). Special thanks go to Dr. Lingguo Yuan for the many fun talks on the philosophy of life, Dr. Guangcai Feng for the discussions on SAR data processing, Mi Jiang for sharing his understanding of coherence analysis and InSAR signal simulation, Jun Hu for inspiring arguments on retrieving 3D deformation from SAR data with Kalman filtering, and Peng Ti who is also my roommate and always prepared to help me. I am also thankful to previous group members, especially Professor Guoxiang Liu, Professor Zhiwei Li and Associate Professor Ping Zhong, and Dr. Yanling Chen for their encouragements and supports.

I would like to take this opportunity to acknowledge the guidance of my Master's advisor Professor Jicang Wu, Tongji University. Many thanks also go to Mr. Chunis Deng, Atheros Communications Inc. for the support on Shell and Python programming. The financial support of the Hong Kong Polytechnic University is humbly acknowledged.

Finally, I am grateful for the persisting support of my parents.

Contents

1 Introduction

"Discovery conceits in seeing what everyone else has seen and thinking what no one else has thought."
--Albert Szent-Gyorgi

The study of Earth's surface deformation has made some major breakthroughs in the last century with the development of space-based observation techniques. An important breakthrough has been the advent of satellite interferometric synthetic aperture radar (InSAR) that has revealed details of crustal deformation fields despite the many problems that the technique still has. This research considers the development of a robust multi-temporal (MT) InSAR analysis method and its applications to the retrieval of deformation parameters in tectonically active areas.

1.1 Background

Interferometric synthetic aperture radar (InSAR) techniques exploit the phase differences between two temporally separated SAR images over an area, providing measurements of deformation along the radar line of sight (LOS) with centimeter to millimeter level of accuracy[Gabriel et al., 1989]. Since the launch of the ERS-1 satellite by the European Space Agency (ESA) in 1991, high quality SAR images of the Earth have become increasingly available which contributed greatly to the success of radar interferometry. InSAR has been widely applied to investigate single deformation events, for example, earthquakes [e.g., Massonnet et al., 1993; Zebker et al., 1994; Zhang et al., 2008; Feng et al., 2010] , volcano eruptions [e.g., Lu, 1998; Amelung et al., 2000; Lu et al., 2003] , and glacier changes [e.g., Mattar et al., 1998; Strozzi et al., 2008]. In most of these applications the coherence of the interferograms is high and nuisance components of phases can either be modeled independently or practically ignored. However noise effects arising from the temporal and spatial decorrelation [Zebker and

Villasensor, 1992] as well as the atmospheric fluctuation [Zebker and Rosen, 1996 ; Ding et al., 2008; Li et al., 2010] commonly exist in interferograms, often greatly limiting the application of InSAR technique.

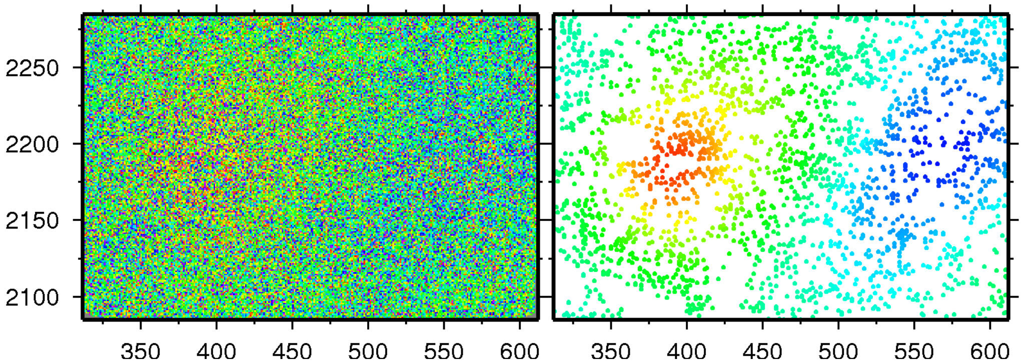

Fig. 1.1: A simulated illustration indicating that extracted coherent points from highly decorralated area can be used to determine reliable deformation. In the left figure the phase noise at a large number of pixels hinder us extracting reliable deformation signal while if the coherent points are well isolated, shown in the right figure, the extraction of deformation signal becomes rather easy.

The multi-temporal SAR data analysis methods (also called advanced InSAR methods) have ushered in a new era of advanced radar remote sensing because of their emphasis on reducing or even eliminating the limitations in the conventional InSAR technique, thereby improving the precision of InSAR measurements. Since Usai [1997] first suggested that useful information can be retrieved from points that keep high coherence for a long time, an enormous amount of efforts has been expended on the development of robust algorithms and applications of the technique to detect time varying deformation patterns in urban and non-urban areas. Technical progresses can be seen from two aspects (1) phase-coherent point identification [e.g., Ferretti et al., 2001; Werner et al., 2003; Hooper, 2004; Adam and Bamler, 2005; Shanker and Zebker, 2007]; and (2) parameter (i.e., DEM error, deformation time series) estimation [Ferretti et al., 2000; Usai, 2000; Berardino et al., 2002; Kampes and Hanssen, 2004; Lanari et al., 2004; Hooper and Zebker, 2007; Hooper, 2008; Adam and Parizzi, 2009; Liu et al., 2009;]. Indeed by exploring the coherent points in SAR images (e.g., Fig. 1.1) and analyzing their phases as a function of time and space, one can precisely estimate the long-term time varying patterns of deformation signals at an expense of losing considerable spatial resolution. The unique capability of multi-temporal SAR data analysis methods has given rise to new tools for studying dynamic processes of geophysical and engineering activities.

1.2 Motivation

When applying the multi-temporal InSAR (MT-InSAR) methods in real cases, we have realized that reliable results can only be achieved with a solid understanding of the core processing algorithms and the parameters that need to set (e.g., the threshold for coherent point selection is often set based on experience). The estimation of phase ambiguities that is usually performed in the spatial and/or temporal domain is a vital step for all current MT-InSAR methods, however the success of phase ambiguity estimation cannot be guaranteed in practice. In many cases there are often pixels or areas that are placed on the wrong multiple of 2π , and it is difficult to identify these points without additional information. The limitations motivate the search for advanced algorithms for retrieving deformation parameters more reliably.

1.3 Contributions

The aim of this study is to develop a reliable MT-InSAR analysis method for estimating displacement parameters more efficiently and reliably. It is comprised of the following five principal components.

Temporarily Coherent Point (TCP) identification and coregistration. The reliability of current coherent point selection methods depends on the amount of SAR data and their temporal resolution, the characteristics of the deformation and the threshold used. In this study we propose an effective method which can identify coherent points from a small set of SAR images based on the spatial statistics of offsets in azimuth and range direction at the step of coregistration. We call the selected points "temporarily coherent points (TCPs)" that do not need to be coherent during the whole time span of the data series. Moreover since the starting point of current MT-InSAR methods is the coregistered SAR images, there is no special emphasis on the coregistration of coherent points. However the method that employs evenly distributed patches over the whole interested area to estimate a polynomial to resample the slave images may not be optimal for coregistering coherent points. This is mainly due to the fact that the standard deviation of the estimated offsets at scatterers with low coherence is higher than those from high-coherent points. Here as a by-product of TCP selection the offsets at TCPs are used for coregistering themselves. By coregistering the coherent points improvement in the interferometric coherence of these points can be observed especially in heavily decorrelated areas.

TCP Networking. How to connect the TCPs to form a spatial network is vital for efficient estimation of deformation parameters as well as DEM errors. Since Delaunay triangulation has no control on the edge length of the triangles, global Delaunay triangulation over the interested area will result in unnecessarily long arcs which for areas undergoing fast deformation, may cause a large amount of arcs having phase ambiguities. Although arcs with lengths longer than the threshold can be removed after the network construction, the density of the network sometimes can not be ensured. In this study we propose to perform the triangulation in distributed patches of the area with limited sizes which can connect the TCPs extensively without increasing the computational complexity.

TCP Parameter estimation with no need of phase ambiguity estimation. With the help of dense TCPs and TCP pairs, the estimation of deformation parameters becomes rather simple. Since we only select the interferograms with short spatial and temporal baselines as observations, a sufficient number of the phase differences at arcs will not have ambiguities. If we only focus on these arcs the estimation of the phase ambiguities can be avoided and thereby the reliability and efficiency of the algorithm can be improved. In this study we take the deformation parameter estimation as a linear inversion problem and design a phase ambiguity detector based on the examination of least squares residuals to eliminate the effects of arcs that have phase ambiguities.

TCP variance component estimation. Kampes and Hanssen[2004] first introduced the variance component estimation (VCE) for their single-master based persistent scatterer InSAR technique to better consider the quality of the interferograms and to evaluate the precision of the estimated parameters. In this study we integrate VCE into the multi-master based TCPInSAR technique with an emphasis on a reliable and efficient estimating strategy. Since it is not necessary to estimate the phase ambiguities in our method, the efficiency of VCE can be significantly improved.

TCP orbital error correction. Due to inaccurate determination of the satellite orbits, orbital contributions to interferograms commonly exist. For obvious orbital fringes, previous studies usually estimate them an interferogram by an interferogram [Wright et al., 2004]. However this approach is time consuming and the results are easily distorted by atmospheric artifacts and/or phase unwrapping errors. In this study we propose to determine the orbital errors after the parameter estimation since in the estimated deformation map, the atmospheric component is rather limited (the effect of atmospheric delay has been largely suppressed during the parameter estimation procedure) and the orbital error can still be modeled by a simple polynomial.

1.4 Outline

The rest of this thesis is organized as follows. In Chapter 2 we will review the state of the art of the methods for coherent point selection and parameter estimation to provide motivation for undertaking a fresh effort to develop a novel MT-InSAR technique. The theory and algorithm needed for identifying TCP are the subject matter of Chapter 3, and Chapter 4 lays the theoretical foundations for our least squares estimator used in the TCPInSAR method. The algorithms as well as the study of correcting orbital errors under the framework of TCPInSAR are also validated with simulated data in this chapter, while the practical issues that need addressed for robust implementation of TCPInSAR are considered in Chapter 5 where a comparison between the result from the TCPInSAR method and that from GPS observations over Los Angeles basin is also performed to enable a quantitative assessment of the performance of TCPInSAR method. In chapter 6 we demonstrate the performance of TCPInSAR method on changing landscapes by applying the method to the southern Macau, China. Finally in chapter 7 we summarize the contribution of the thesis and suggest some directions for future research.

2 Multi-Temporal InSAR

Since the late 1990's, there has been a growing interest in understanding the properties of coherent points in SAR interferometric images and their applications. This has been mainly motivated by the realization that coherent points are extremely useful in estimating long-term and time-varying deformation patterns. The employed techniques are termed multi-temporal InSAR (MT-InSAR) which involves joint processing of multiple SAR acquisitions. In the following we will give a brief review of the MT-InSAR approaches where two lines of efforts placed on the current MT-InSAR methods for the identification of coherent points (2.1) and parameter estimation (2.2) are introduced respectively.

2.1 Coherent point identification

2.1.1 Introduction

Coherent points are pixels that can keep high phase quality in a certain time span. The identification of coherent points is usually the first step and plays an important role in MT-InSAR analysis since the quality and density of coherent points affects the parameter estimation. Over the years several criteria have been proposed and the selected coherent points are coined interchangeably as permanent scatterer [Ferretti et al., 2001], persistent scatterers [Adam, 2004], coherent point targets [Mora et al., 2003] et al.

2.1.2 Coherence stability

Coherence has long been used to evaluate the quality of interferograms, and can be used as a criterion for selecting coherent points from which signals of interest can be estimated precisely.

The complex coherence of two zero-mean complex signals s_1 and s_2 is defined as (Hanssen, 2001)

$$\gamma = \frac{E(s_1 s_2^*)}{\sqrt{E(|s_1|^2)\, E(|s_2|^2)}} \tag{2.1}$$

where $E(x)$ is the expected value of x. Under the assumption that the processes involved in Eq. (2.1) are ergodic, the maximum likelihood estimator of the coherence magnitude $|\hat{\gamma}|$ over an estimation window of $n \times m$ (range,azimuth)pixels can be expressed as

$$|\hat{\gamma}| = \frac{\left| \sum_{i=1,\, j=1}^{n,m} s_1(i,j)\, s_2{}^*(i,j) \right|}{\sqrt{\sum_{i=1,\, j=1}^{n,m} s_1(i,j)\, s_1{}^*(i,j) \sum_{i=1,\, j=1}^{n,m} s_2(i,j)\, s_2{}^*(i,j)}} \tag{2.2}$$

The coherence criterion is used for example by short baseline (SB) MT-InSAR techniques[e.g., Berardino et al., 2002; Mora et al., 2003; Usai, 2003]. After eliminating the phase components related to topography and flat earth, the magnitude of the coherence of each pixels ($|\hat{\gamma}_i|$) in selected interferograms can be estimated. A mean coherence map can then be generated by

$$\gamma_{mean} = \frac{1}{N} \cdot \sum_{i=0}^{N-1} |\hat{\gamma}_i| \tag{2.3}$$

where N is the number of interferograms. All pixels with a mean coherence over a selection threshold are accepted as coherent point candidates. Mora [2003] suggested a minimum value of mean coherence of 0.25 for coherence maps estimated by a window of 4 by 16 or 5 by 20 (range by azimuth) with C-band ERS-1/2 and Envisat/ASAR data. It is worth noting that since the interferometric combinations might share identical images, the estimated coherence might be correlated which should should not be ignored during the calculation of the mean coherence map.

2.1.3 Amplitude dispersion index

The amplitude dispersion index was first introduced by Ferretti and his colleagues for their patented Permanent Scatterer (PS) InSAR technique which employs the single- master interferogram stacks without considering the baseline limitations. Since interferograms can be highly effected by spatial decorrelation it is impossible to use the spatially estimated coherence criterion to select pixels with good phase quality. With the PSInSAR technique, the phase dispersion (σ_ϕ) of pixels can be estimated starting from the amplitude dispersion which is defined in [Ferretti et al., 2001] as

$$\sigma_\phi \simeq \frac{\sigma_A}{m_A} = D_A \tag{2.4}$$

where m_A and σ_A are the temporal mean and the standard deviation of the amplitude at a pixel. Simulation test indicates that the amplitude dispersion index (D_A) is a good approximation for phase dispersion of pixels with high signal to noise ratio (SNR) [Ferretti et al., 2001]. With enough radiometrically calibrated SAR images (>30) the points are selected as PS candidates if D_A is below a threshold (e.g., 0.25). Compared with coherence stability, the amplitude dispersion index does not average the data inside an estimation window, enabling the monitoring of localized deformation at the highest spatial resolution.

In order to identify sufficiently dense coherent points in non-urban areas where scatterers usually have low signal to noise ratio (SNR), Hooper [2004] proposed a new selection method based on the phase stability which first relies on an identification via the amplitude dispersion. Phase stability is analyzed under the assumption that deformation is spatially correlated. The phase observations of neighboring PS candidates are averaged, and those with lowest residual noise are selected. Given a set of topographically corrected interferograms, a measure of phase stability can be defined as

$$\gamma_x = \frac{1}{N}\left|\sum_{i=1}^{N} \exp\{j(\Phi_{int,x,i} - \overline{\Phi}_{int,x,i} - \Delta\hat{\Phi}_{\epsilon,x,i})\}\right| \tag{2.5}$$

where N is the number of interferograms, $\Phi_{int,x,i}$ is the differential phase of the xth interferogram and $\overline{\Phi}_{int,x,i}$ is the mean phase of all PS candidates within a circular patch centered on pixel x with radius L and $\Delta\hat{\Phi}_{\epsilon,x,i}$ is the estimated phase component contributed by DEM errors. For calculating the mean phase of patches efficiently, PS candidates selected based on amplitude dispersion using a high threshold value can be taken as an initial selection. With this approach the threshold value of γ_x is selected in a probabilistic fashion assuming that the coherence with values less than 0.3 corresponds to noisy non-PS pixels[Shanker, 2010].

2.1.4 Signal-to-clutter ratio

The signal-to-clutter ratio (SCR) approach was first suggested by Adam to select coherent points for their Persistent Scatterer InSAR (PSI) processor. With an assumption that a PS observation consists of a deterministic signal that is disturbed by random circular Gaussian distributed clutter, the SCR can be estimated by computing the ratio of the power of a PS candidate over that of its immediate neighboring pixels. The relationship between the SCR and the phase standard variance(σ_ϕ) can be defined as[Adam, 2004]:

$$\sigma_\phi = \frac{1}{\sqrt{2 \cdot SCR}}, SCR = \frac{s^2}{c^2} \tag{2.6}$$

Where s represents the amplitude of the dominant scatterer and c the clutter in the surroundings. Eq. (2.5) can be used to determine a reasonable threshold of SCR. For example, if a phase standard variance of 0.5 rad^2 is desired, the minimum of SCR value is 2. It is shown in (Adam et al., 2004) that both the SCR and D_A are based on the same signal model for a dominant point scatterer surrounded by incoherent background clutter, and a direct relationship between them can be expressed as:

$$D_A = \frac{1}{\sqrt{2 \cdot SCR}} \tag{2.7}$$

Since the SCR estimation can be performed with a single SAR image, compared with amplitude dispersion index the SCR threshold has far less requirement on the size of datasets. A pixel with a high SCR at each acquisitions is selected as a PS candidate.

2.1.5 Summary

Although the approaches for coherent point identification mentioned earlier have been widely adopted by current MT-InSAR techniques, there are limitations of current methods as summarized below:

(1) The settings of the threshold values as well as patch sizes heavily depend on experiences. In other words it is difficult to know the optimized value of these settings that can balance the phase quality and spatial density of the selected points. For example, Figure 2.1 shows the location maps of coherent point candidates over Macau area selected by coherence stability and amplitude dispersion index with different threshold values respectively. A total of 41 Envisat/ASAR images covering a time span from 20030406 to 20100926 are used. It is clear that the density of the coherent point candidates is quite different, which largely depends on the thresholds. This might raise confusion to the users. Another example is that with the method of phase stability the

selection of the patch size for calculating the mean phase is not an easy task, especially in areas undergoing spatially complex deformation.

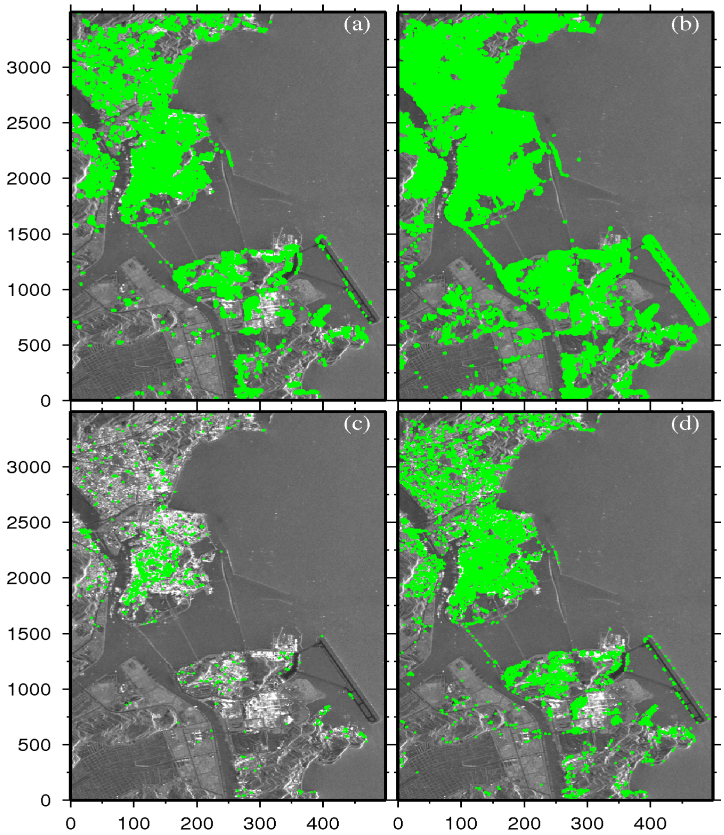

Fig. 2.1: Coherent point selection with coherent stability and amplitude dispersion index for Macau area. (a) coherence threshold=0.5;(b) coherence threshold=0.3; (c) amplitude dispersion index less than 0.4; (d) amplitude dispersion index less than 0.6. The green dots are the selected coherent points using different thresholds.

(2) Coherent points are not coregistered with special consideration. The starting points of current MT-InSAR methods are the interferograms or resampled SLC images resulted from a global coregistration procedure for the whole slave images. However this global coregistration procedure which employs the offsets estimated from distributed windows over the images to determine polynomials for resampling the slaves is not necessarily optimal for the coherent points. This is mainly due to the fact that the standard deviation of the estimated offsets at the distributed scatterers is larger than that of strong scatterers. Therefore coregistration especially designed for the coherent points should be developed.

To overcome these limitations, it is necessary to develop an algorithm capable of identifying the coherent points reliably from a small set of images where no parameter needs to be set based on experience, which is the focus of the Chapter 3.

2.2 Parameter estimation

After the identification of coherent points, the deformation parameters as well as DEM errors can be estimated from them. To date several effective algorithms have been proposed, each with its own advantages and potential disadvantages. Broadly speaking, these algorithms may be classified into the following two categories:

Algorithms with single-master interferograms ---- The algorithms stimate the deformation parameters from interferograms without considering the limitation of critical baselines, e.g., PSInSAR [Ferretti et al., 2000; Colesanti et al., 2003], STUN [Kampes and Hanssen, 2004], StaMPS [Hooper and Zebker, 2007], IPTA [Werner et al., 2003].

Algorithms with multi-master interferograms ---- The algorithms estimate the deformation parameters from short baseline interferograms in which the spatial decorrelaton is relatively small, e.g., Usai's algorithm [Usai, 2003], SBAS [Berardino et al., 2002] and Mora's algorithm [Mora et al., 2003].

The starting point of all the algorithms is the wrapped differential phase which contains the phase components contributed by deformation, DEM error, atmospheric artifacts, orbital error, Doppler centroid difference and noise. We will introduce below two typical algorithms i.e., PSInSAR and

SBAS with emphasis on how these algorithms deal with the phases of the coherent points. The shortcomings of the methods will also be discussed.

2.2.1 PSInSAR

Since the PSInSAR algorithm has been patented, the details of the algorithm are not always clear. The description here is based on [Ferretti et al., 2000; Colesanti et al., 2003].

Differential interferogram formation with single-master

With $N+1$ SAR images, a reference digital elevation model (DEM) and precise orbit data, we can obtain N full-resolution differential interferograms with respect to the same master image. For a permanent scatterer candidate (PSC) (x) in the ith interferogram with temporal baseline t_i , the differential phase Φ^k can be written as

$$\Phi(x,t_i)=W\{\phi_{topo}(x,t_i)+\phi_{defo}(x,t_i)+\phi_{atmo}(x,t_i)+\phi_{noise}(x,t_i)\} \quad i=1\cdots N \tag{2.8}$$

where $W\{\cdot\}$ represents the wrapping operator, $\phi_{topo}(x,t_i)$ is the phase caused by DEM error, $\phi_{defo}(x,t_i)$ is the phase due to displacement of the point, $\phi_{atmo}(x,t_i)$ is the phase raised by atmospheric delay, $\phi_{noise}(x,t_i)$ is decorrelation noise. The topographic phase is a linear function of the perpendicular baseline, i.e.,

$$\phi_{topo}(x,t_i)=\beta(x,t_i)\cdot\Delta h_x \tag{2.9}$$

where $\beta(x,t_i)$ is the height-to-phase conversion factor, and Δh_x is the DEM error at the point. The deformation phase can be separated into two terms, i.e.,

$$\phi_{defo}(x,t_i)=\frac{4\pi}{\lambda}\cdot v(x)\cdot t_i+\phi_{NL}(x,t_i) \tag{2.10}$$

where $v(x)$ is the mean deformation rate of target x, λ is the wavelength of the radar signal, and $\phi_{NL}(x,t_i)$ is the phase component due to non-linear motion. The interferometric phase at point x can be finally written as

$$\Phi(x,t_i)=W\{\beta(x,t_i)\cdot\Delta h_x+\frac{4\pi}{\lambda}\cdot v(x)\cdot t_i+\omega(x,t_i)\} \quad i=1\cdots N \tag{2.11}$$

where $\omega(x,t_i)$ is the phase sum of three contributions, atmospheric delay, noise and non-linear motion.

Considering two neighboring PSCs x and y, the phase difference between them can be expressed as

$$\Delta\Phi(x,y,t_i)=W\{\beta(x,t_i)\cdot\Delta h_{x,y}+\frac{4\pi}{\lambda}\cdot\Delta v(x,y)\cdot t_i+\Delta\omega_i\} \tag{2.12}$$

where $\Delta h_{x,y}$ is the difference of the DEM errors at the two points, $\Delta v(x,y)$ is the velocity difference; and $\Delta\omega_i$ is the difference of the residual phase, which is assumed to be small, since all its components(i.e., differential atmospheric signal, non-linear deformation and random noise) are small.

Preliminary estimation

In the PSInSAR technique the estimation of the parameters from the observed wrapped phase pairs is performed by a search through the solution space. Under the condition

$$|\Delta\omega_i|<\pi \tag{2.13}$$

the absolute value of the complex ensemble coherence

$$\hat{\gamma}_{x,y}=\left|\frac{1}{N}\sum_{i=1}^{N}e^{j\Delta\omega_i}\right| \tag{2.14}$$

can be adopted as a reliable norm [Ferretti et al., 2000]. The coherence value lies in the range [0,1]. A high coherence value implies a good estimation of the differential DEM errors and the differential velocity. In practice the coherence is maximized by sampling the two-dimensional solution space with a certain resolution and up to certain bounds, each time evaluating the norm [Kampes, 2006]. It should be noted that Eq. (2.13) is satisfied under the assumption that the differential atmospheric effect between the two neighboring points is small, the relative non-linear deformation is small and phase noise at points is also small. If the condition i.e., Eq. (2.1.3) is wrongly assumed, the parameters estimated from Eq. (2.1.4) are no more reiliable.

After obtaining the maximum coherence values for all the arcs, a threshold is needed to remove the unreliable arcs. Unfortunately the determination of this threshold is not practically straightforward. In other words, users have to select the threshold based on experience. AS a reference, 0.75 was used in Ferretti et al. [2000]. The parameters (DEM error and the mean deformation rate) at PSCs can then be obtained by integrating the DEM error and rate differences between all pairs of PSCs with respect to a reference point.

Atmospheric phase

After removing the phase components contributed by DEM errors and linear motions on arcs, the residual phase at the PSCs can be unwrapped by a weighted least-squares integration. The residual phase contains the components due to atmospheric delays, the non-linear motion and random noise. Under the assumption that the atmospheric signal behaves randomly in time and is correlated in space, it can be isolated from other components by low-pass filtering in the spatial domain and high-pass filtering in the temporal domain.

First a mean value($\bar{\omega}(x)$) of the residual phase is calculated for each arc, which is an estimation for the atmospheric phase in the master acquisition. Since this master-related atmospheric phase will not pass the high-pass filter, it should be subtracted from the residual phase.

$$\omega'(x,t_i)=\omega(x,t_i)-\bar{\omega}(x) \tag{2.15}$$

Then the temporal high-pass filtering is performed to remove the possible temporally correlated displacement from the residual phase. Finally a spatial low-pass filter is applied to the temporally filtered residuals to remove the random noise component[Kampes, 2006]. Note that the order of the filtering steps can be interchangeable. The estimated atmospheric phase ($\hat{\phi}_{atmo}(x,t_i)$) at a point (x) in the ith interferogram can be expressed symbolically as

$$\hat{\phi}_{atmo}(x,t_i)=\left[[\omega'(x,t_i)]_{HP-time}\right]_{LP-space}+\left[\bar{\omega}(x)\right]_{LP-space} \tag{2.16}$$

In the implementation of the filters, to make it simple, Ferretti [2000] used a triangular window with the length of 300 days for the temporal filter and a 2×2 km^2 averaging window for the spatial filter for a data set containing 41 ERS SAR images acquired from 19920617 to 19990116.

Final estimation

After the estimation of the atmospheric phase at the PSCs, the full resolution atmospheric component can be determined by Kriging interpolation, which is referred to as “atmospheric phase screen” (APS) [Ferretti et al., 2000]. From the differential interferograms without APSs, the DEM errors and displacement can be estimated on a pixel by pixel basis. More PS can now be identified. The time series deformation can be estimated by the low-pass temporal filtering mentioned earlier.

2.2.2 SBAS

The Small Baseline Subset (SBAS) algorithm[Berardino et al., 2002] is a post-processing method to determine the deformation parameters as well as DEM error from a set of multi-master differential interferograms with short spatial baselines. Compared with PSInSAR technique, this algorithm can be easily implemented. Since the starting point of SBAS method is the unwrapped phases, one of the main error sources is the phase unwrapping error. In this section we will review the key issues behind the algorithm. More technical details about the algorithm can be found in [Berardino et al., 2002; Lanari et al., 2004; Casu et al., 2006]

The algorithm starts from a set of $N+1$ coregistered single look complex (SLC) SAR images acquired at the ordered times($t_0, \cdots, t_N$). Assuming that each image can be involved in at least one interferogram, a number of differential interferograms can be generated. In order to mitigate the decorrelation phenomena, M interferograms with small spatial and temporal baseline as well as small Doppler centroid differences are selected as observations. It should be noted that SAR images involved in the interferograms might be grouped in several independent small baseline subsets that must be properly combined to retrieve the deformation time series.

Since the SBAS algorithm relies on the absolute phase values of high coherent points, the interferometric phase in all the M interferograms restricted to the interval of ($-\pi, \pi$] must b unwrapped. Minimum Cost Flow (MCF) based unwrapping method proposed by Constantini [1998] is most widely used for spatially sparse data. As noted in Berardino et al. [2002], other 2D unwrapping method [Agram and Zebker, 2009]can also be adopted to retrieve the absolute values from single interferograms. After phase unwrapping, a best fit plane is commonly derived to remove the possible phase component caused by imprecise satellite orbit.

Once the phase signal of each unwrapped interferogram with the same reference point is available, the SBAS algorithm can be performed as a follow-up procedure. Considering a generic interferogram j generated from SAR images acquired at times t_B and t_A, the interferometric signal for a coherent pixel located at (x, r) coordinates can be expressed as

$$\begin{aligned}\delta\phi_j(x,r) &= \phi(t_B,x,r)-\phi(t_A,x,r)\\ &\approx \frac{4\pi}{\lambda}\left[d(t_B,x,r)-d(t_A,x,r)\right]+\beta(j,x,r)\Delta z+\delta\phi_{j,atm}(x,r)+\delta n_j \\ &\forall\, j=1,\cdots,M\end{aligned} \tag{2.17}$$

where $\phi(t_B,x,r)$ and $\phi(t_A,x,r)$ are the phases acquired at t_B and t_A respectively, $d(t_B,x,r)$ and $d(t_A,x,r)$ are the LOS cumulative deformation at t_B and t_A with respect to the first scene(i.e., t_0). $\beta(j,x,r)$ and Δz are the height-to-phase conversion factor and the topography error which are the same as in PSInSAR technique. Phase differences caused by the dispersion of the atmosphere at t_B and t_A are included in the term $\delta\phi_{j,atm}(x,r)$. The last term δn_j stands for the phase component contributed by possible decorrelation effects and other noise sources.

Retrieval of low pass deformation and DEM error

InBerardino et al. [2002], the so-called low pass (LP) deformation can be expressed by a cubic model.

$$d(t_i,x,r)=\bar{v}\cdot(t_i-t_0)+\frac{1}{2}\bar{a}\cdot(t_i-t_0)^2+\frac{1}{6}\Delta\bar{a}\cdot(t_i-t_0)^3 \tag{2.18}$$

where $\bar{v}$, $\bar{a}$ and $\Delta\bar{a}$ are the unknowns. Hence Eq. (2.14) can be rewritten as

$$\delta\phi_j(x,r)=\boldsymbol{M}_j\boldsymbol{P}+\delta N_j \tag{2.19}$$

where $\boldsymbol{M}_j$ is the design vector containing the coefficients corresponding to the unknown parameters (i.e., the mean velocity, the mean acceleration, the mean acceleration variation and topography error) and $\boldsymbol{P}$ is the parameter vector having the following form

$$\boldsymbol{P}^T=[\bar{v},\bar{a},\Delta\bar{a},\Delta z] \tag{2.20}$$

δN_j contains phase components contributed by the non-modeled displacement, atmospheric signals as well as other noise. Considering M interferograms, the system of observations for a generic coherent point can be written as

$$\boldsymbol{\delta\Phi}=\boldsymbol{M}\boldsymbol{P}+\boldsymbol{\delta N} \tag{2.21}$$

where $\boldsymbol{\delta\Phi}$ represents the unwrapped and ramp removed phase vector, $\boldsymbol{M}$ is an $M\times4$ design matrix corresponding to the parameters in $\boldsymbol{P}$, and $\boldsymbol{\delta N}$ is the non-modeled phase vector. Assuming $\boldsymbol{\delta N}$ behaves randomly in temporal space, Eq. (2.18) can be solved under the framework of least squares.

It is important to note that in SBAS technique the LP displacement model no matter a cubic pattern or a linear model is only used for the estimation of the DEM error. In other words, the estimated LP displacement component(s) will not be used in the following displacement time series analysis.

Preliminary estimation of displacement time series

To simplify the phase unwrapping procedure, the estimated LP phase component as well as the topographic error are subtracted from the wrapped input interferograms. The remaining phase can be easily unwrapped since the fringe rate has been reduced significantly. The LP phase component is then added back to the unwrapped phase forming the phase observations that can be expressed as

$$\Phi_j = \sum_{k=IS_j+1}^{IE_j} \frac{4\pi}{\lambda}(t_k - t_{k-1}) v_k + \delta N'_j \quad \forall j = 1, \cdots, M \tag{2.22}$$

where v_k is the mean motion velocity between time-adjacent acquisitions, and $\delta N'_j$ represents the phase related to atmospheric artifacts and noise. Accordingly a system of M equations in N unknown can be organized as

$$\boldsymbol{\Phi} = \boldsymbol{B}\boldsymbol{v} + \boldsymbol{\delta N}' \tag{2.23}$$

where $\boldsymbol{B}$ is an $M \times N$ matrix corresponding to the unknown vector $\boldsymbol{v}$. Once again the parameters corresponding to the velocities can be resolved by least squares. Unfortunately at this stage the matrix $\boldsymbol{B}$ has a risk to be rank deficient since it represents the cumulative time between each interferometric pair and depends on the combination of SLC images for interferograms. To overcome this problem, the pseudoinverse of $\boldsymbol{B}$ is used, which can be calculated by singular value decomposition (SVD) (see[Berardino et al., 2002] for details). The displacement time series can be directly achieved according to the velocities and time intervals. However it should be noted here that the assumption that the atmospheric artifacts and decorrelation noise follow Gaussian distribution in temporal domain does not always hold in real cases. Therefore the estimated displacement time series contains possible atmospheric errors and needs to be further processed.

Final displacement time series estimation

In the SBAS technique the mitigation of atmospheric effect is performed by a filtering operation which is derived by Ferretti [2001] for the PS technique (see section 2.2.1 for the details). After removing the undesired atmospheric signal, the displacement time series is finally achieved from the remained phases based on the minimum norm least squares.

2.2.3 Summary

The aforementioned algorithms for deformation parameter estimation in MT-InSAR techniques are quite classical and have been successfully applied to numerous real cases. However there is still room for improvement. Phase unwrapping, a vital step in both algorithms, currently can not be always reliably performed no matter by searching through the solution space or by 2D spatial methods. Kampes [2006] first proposed a stochastic model for single-master MT-InSAR system and described the precision of the estimated parameters by the full variance-covariance (VC) matrix, however there is a lack of similar work for multi-master MT-InSAR system. Moreover since the SBAS technique takes the phase components at pixels rather than the phase differences between two neighboring pixels as observations, the effect of the atmospheric artifacts on parameter estimation can be more serious. For these reasons, the work presented in Chapter 4 is geared towards the development of innovative processing algorithms aimed at estimating deformation parameters from a multiple master MT-InSAR system without phase unwrapping and providing the VC matrix for precision evaluation.

3 Temporarily Coherent Point

In this chapter an approach is presented for identifying and extracting temporarily coherent points (TCP) that exist between two SAR acquisitions which can be applied for such as ground settlement monitoring. TCP are identified based on the spatial characteristics of the range and azimuth offsets of coherent radar scatterers. A method for coregistering TCP based on the offsets of TCP is also given to reduce the coregistration errors at TCP. The proposed algorithms are validated using a test site in Hong Kong. The test results show that the algorithm works satisfactorily for various ground features and is a plausible candidate of methods for the identification of coherent points based on a small number of SAR data.

3.1 Introduction

As mentioned in Chapter 1 temporal decorrelation is a major limitation for the application of interferometric synthetic aperture radar (SAR) (InSAR) [e.g., Zebker and Villasensor, 1992]. Persistent Scatterer (PS) Interferometry (PSI), an extension to the conventional InSAR, is a proven effective technique for measuring displacement in areas of low correlation. Since Ferretti [2000] first suggested an algorithm to exploit PS pixels, similar algorithms have been developed by various groups. These methods identify PS from a time-series of interferograms either using a temporal functional model [Ferretti et al., 2000; Colesanti et al., 2003; Werner et al., 2003] or spatial correlation of phase measurements [Hooper et al., 2004]. However all these methods can only obtain reliable deformation measurements in regions with enough SAR acquisitions. In areas where the number of interferograms does not meet the minimum requirement, the methods usually fail to identify a dense network of PS pixels. Signal-to-Clutter Ratio (SCR) [Adam, 2004] is another type of method for PS identification that requires a spatial estimation window around a point scatterer. The method does not need to calibrate the amplitude data to estimate the SCR and it does not require many SAR images, however the method also has its disadvantages when multiple point scatterers are present in nearby pixels.

Although accurate coregistration of PS is critical in PSI, there is usually no special consideration for precise PS coregistration in current PSI methods. All the slave SAR images are typically coregistered to a common SAR image based on range and azimuth offsets of distributed windows over the images. However, since the majority (typically 90% or more) of the pixels in the images are distributed scatterers (non-PS pixels) [Kampes, 2006] and errors in their estimated offsets are in general larger than those in the estimated offsets of the PS, the coregistration accuracy of PS has a potential risk of being affected by the less optimal coregistration methods. Although the results from the conventional coregistration method are usually verified by rigorous testing, the errors in the offsets estimated from distributed scatterers have effects on the estimated coregistration polynomials. In other words, the coregistration polynomials are only optimal for the overall samples but not necessarily optimal for each sample.

In this chapter a new InSAR analysis approach is presented. It includes algorithms for identifying and coregistering coherent points, named as temporarily coherent points (TCPs). Under the framework of MTInSAR, the TCPs stand for the points that do not necessarily keep coherent during the whole observation time span, therefore the TCPs include both the persistently coherent points and partially coherent points. The identification of TCPs is based on the standard deviation of the estimated offsets derived by Bamler [2000] and the fact that the offsets estimated from strong scatterers are less sensitive to the window size and oversampling factor used than those from distributed scatterers. The approach is validated using a test site located in Hong Kong.

3.2 Methodology

3.2.1 Offset estimation

Estimation of offsets between two SAR images with an accuracy of better than 0.1 pixel is critical in interferogram generation to avoid significant loss of phase coherence [Hanssen, 2001]. Several factors contribute to image offsets, including different timing along the satellite orbit, baseline variation, pulse repetition frequency (PRF) variation, ground deformation and varying satellite velocity [Ferretti et al., 2007]. Offsets between a pair of SAR images can be typically described by such geometric changes between the two images as range and azimuth shifts, range and azimuth stretches, and range and azimuth skews. The effects of stretch and skew are limited for ERS and Envisat data [Gatelli et al., 1994]. In theory the offsets are also related to local ground elevation although the offsets from this effect are insignificant for ERS and Envisat data due to the limited bandwidth of the data [Arikan et al., 2007].

The commonly used methods for estimating offsets between two SAR images are based either on cross-correlation between the two amplitude images [Gray et al., 1998; Rott et al., 1998; Michel and Ftignot, 1999] or on fringe visibility (also referred to as coherence optimization) algorithm [Lin et al., 1992] that is mainly suitable for images of high coherence. For image pairs with long baselines the geometrical approach aided by a reference DEM and orbit information [Fornaro and Manunta, 2005] can also be considered. In the amplitude correlation method, the estimation of the local image offsets is reliable only when the features in the two SAR image patches are identical [Strozzi et al., 2002]. Therefore unstable features usually make the offsets vary randomly. This property will be used in the algorithm for TCP identification to be presented below.

3.2.2 Identification of TCP

For areas undergoing gentle deformation the offsets estimated from patches of images with stable ground features should be nearly identical. For image patches with unstable ground features, on the other hand, the location of the correlation peak varies, leading to random changes in the estimated offsets. Figure 3.1 shows the estimated offset vectors for an area over the Hong Kong Airport. It is clear that after removing the initial offsets estimated based on the satellite orbits the remaining offsets in the sea and in the mountainous areas appear very random due to the low correlation which result in errors in the estimated offsets while the offsets of the strong scatterers are very consistent (red dots without apparent offset vectors). It is therefore possible to distinguish stable image patches (coherent scatterers) from the unstable ones (distributed targets) based on the offset information.

The estimated offsets of points with high coherence are less sensitive to the size of the patches and to the oversampling factor. This property can also be verified theoretically [Bamler, 2000]. When estimating the offsets with the cross-correlation method, the standard deviation of an estimated offset ($\delta_{r,a}$) (in range or azimuth) for a homogenous image patch is

$$\sigma(\delta_{r,a})=\sqrt{\frac{3}{2\mathrm{N}}}\cdot\frac{\sqrt{1-\gamma^2}}{\pi\gamma}\chi^{\frac{3}{2}} \tag{3.1}$$

where σ is the standard deviation expressed as a fractional number of pixels; N is the number of samples in a patch; γ is the coherence of the patch that is also related to N

$$|\hat{\gamma}|=\frac{\left|\sum_{i=1,\,j=1}^{n,m} s_1(i,j)\,s_2^{\,*}(i,j)\right|}{\sqrt{\sum_{i=1,\,j=1}^{n,m} s_1(i,j)\,s_1^{\,*}(i,j)\sum_{i=1,\,j=1}^{n,m} s_2(i,j)\,s_2^{\,*}(i,j)}} \tag{3.2}$$

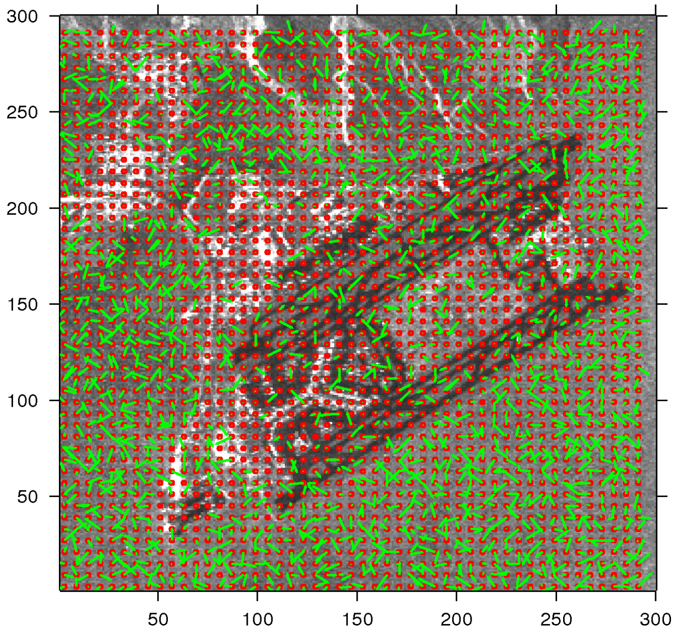

Fig. 3.1: Offset vectors over the area of Hong Kong Airport as determined by the method of cross correlation

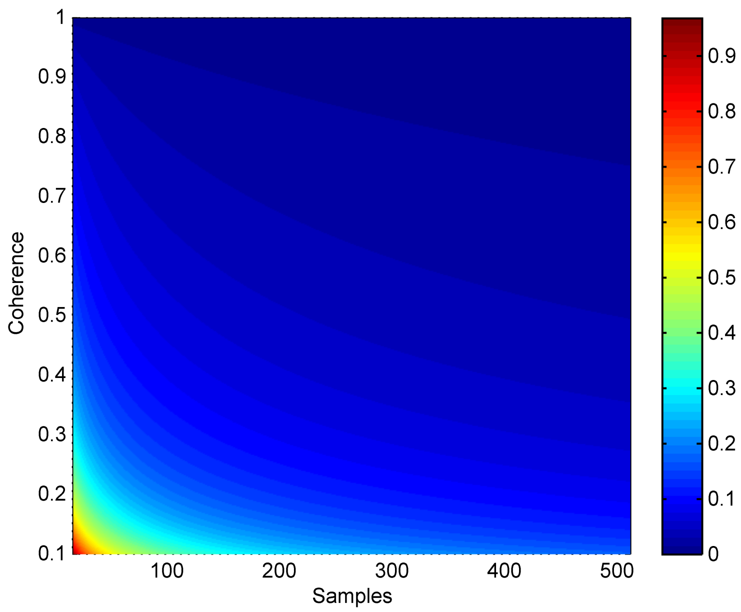

Fig. 3.2: The standard deviation of the measured offset as a function of the number of samples in a patch and the coherence of the patch (unit: pixel). See Eq. (3.1).

$N=m\times n$,and χ is the oversampling factor. In Eq. (3.1), considering the χ as a constant, we plot the σ as a function of N and γ (Fig. 3.2). We can find that the standard deviation of the measured offset varies obviously in the areas with low coherence (i.e. unstable patches) when the number of samples changes, whereas it remains relatively stable in high coherence areas. Therefore coherent scatterers can be identified by calculating and examining the offsets while changing the size of the image patches. Compared with the conventional coherence threshold, the proposed method can be applied more reliably. This is mainly because the conventional coherence estimator itself is biased (especially under low coherence conditions the estimator is shown to be significantly biased [Touzi et al., 1999]) and its performance depends on the window size, the threshold and the assumption of ergodicity within the estimation window. Theoretically the bias B in the coherence magnitude is derived as [Touzi et al., 1999]

$$B=\frac{\Gamma(N)\Gamma(1+1/2)}{\Gamma(N+1/2)}\times {}_3F_2(3/2,N,N;N+1/2;1;\gamma^2)\times(1-\gamma^2)^N-\gamma \tag{3.3}$$

where $\Gamma(\cdot)$ is the gamma function and ${}_qF_p$ is the generalized hypergeometric function. Figure 3.3 presents the bias in the coherence magnitude as a function of independent samples for $\gamma=0.1,0.5,0.8$ respectively together with the corresponding offset standard deviations with fixed oversampling factor.

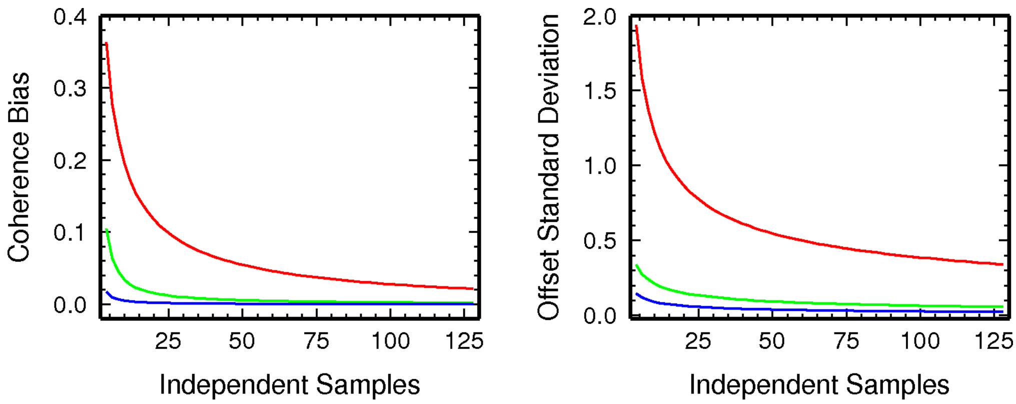

Fig. 3.3: The relationship between independent samples with coherence bias (left) and offset standard deviation (right) for difference coherence magnitude. Red line:0.1;Green:0.5;Blue:0.8.

It is clear that in areas with low coherence, improper window size used by the coherence estimator will result in large bias. In real cases it is quite often to see that due to the biased estimation of coherence, even in non-coherent areas (like water body) there are still points mistakenly selected. It indicates that when using the conventional coherence map to select the coherent points, the window size and threshold should be carefully selected, which currently is largely based on experience. However it is worth noting that since Fig. 3.3 shows a similar pattern between the coherence bias and offset standard deviation with changing samples,the strategy to be presented, i.e., estimation with different window sizes, can also be applied on the coherence map to enhance its reliability.

After calculating the initial image offsets based on satellite orbits, the proposed method for identifying TCP starts first by dividing the scene into a set of large patches (e.g., 256×256) and the range and the azimuth offsets of each of the patches are estimated and used to determine the coefficients of an offset polynomial. Second, the estimated offsets are used as initial inputs and the method of cross-correlation is implemented at every pixel using smaller patches (e.g., 5×5). An offset matrix can be obtained from the estimated offset values.

$$\boldsymbol{O}_{l\times m}=\begin{bmatrix} o_{1,1} & o_{1,2} & \cdots & a_{1,m} \\ o_{2,1} & o_{2,2} & \cdots & a_{2,m} \\ \vdots & \vdots & & \vdots \\ o_{l,1} & o_{l,2} & \cdots & o_{l,m} \end{bmatrix} \tag{3.4}$$

where $o_{i,j}, i=1,2,\cdots,l; j=1,2,\cdots,m$ is the offset of pixel (i,j) which contains the offset components in both the azimuth and the range directions. The pixels with identical offsets are selected as TCP candidates using a 2-D histogram.

$$\begin{gathered} o_c = peak\{hist_{2d}(O_{l\times m})\} \\ |o_{i,k}-o_c|<A \end{gathered} \tag{3.5}$$

where A is the tolerance interval. To ensure most of the strong scatterers to be selected as TCP candidates, A can be set to 1 pixel or larger. The 2-D histogram gives a statistics on the consistency of the offsets with a tolerance threshold value determined based on the quickhull algorithm [Barber et al., 1996] that improves the computational efficiency significantly compared with the iteration searching method. Third, the TCP candidates are further evaluated by changing the size of the image patches in cross-correlation estimation (e.g.,from 4×4 to 64×64) and the oversampling factor to find sub-pixel offsets. A fixed oversampling factor can be used for simplicity. A set of offsets can be obtained accordingly for any given TCP candidate (j). The TCP candidates whose offset standard deviations are smaller than 0.1 pixels are selected.

$$\boldsymbol{OT}_{\boldsymbol{j}}=\begin{bmatrix} ot_{j1} & ot_{j2} & \cdots & ot_{jN} \end{bmatrix} \tag{3.6}$$

Fourth, the offsets of the TCP candidates are fit to a smooth polynomial and the TCP candidates whose offsets do not fit the polynomial well are discarded. The remaining candidates are finally selected as TCP. A 6-point truncated sinc interpolator kernel [Hanssen, 2001] is employed to resample TCP in the slave image based on the polynomial determined. A block diagram showing the procedure of selecting TCP is given in Fig. 3.4.

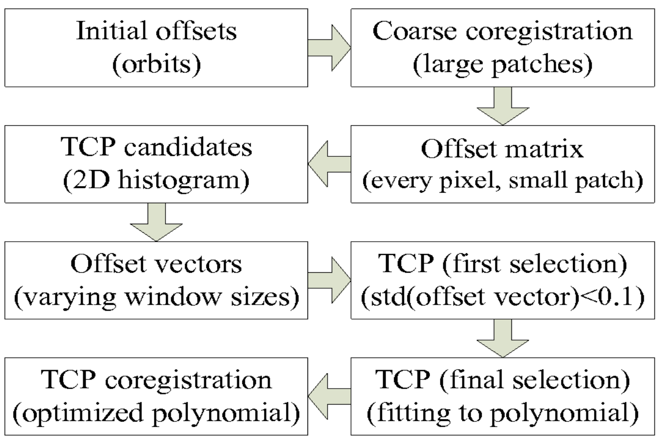

Fig. 3.4: Block diagram of the proposed method for coherent point identification.

It is important to note that in the above process, since the cross-correlation is estimated each time from an image patch and a strong scatterer within a patch may dominate the cross-correlation estimation in several neighbouring patches, pixels near a stable scatterer may be mistakenly identified as TCP candidates. Although such errors should have been considerably reduced at the stage of sub-pixel offset estimation using very small image patches, pixels seriously affected by side lobes of strong scatterers may still be wrongly identified. The phase components of these points should mainly be from the neighboring stable pixels so that they can be considered as one pixel. In addition, for the time series data analysis these points can be further removed based on the least squares residuals during the parameter estimation (i.e., DEM error and deformation rates) if the phases contain large bias [*Zhang et al.*, 2011b].

3.3 Experiments

3.3.1 Validation of the method for TCP identification

The proposed TCP selection method is validated with two corner reflectors (CRs), two buildings, and two regions of distributed scatterers in Hong Kong (see Fig.3.5). The locations of the objects in radar coordinate system are carefully determined and the proposed method is then applied. For simplicity, when calculating the offsets of the points a fixed oversampling factor of 2 is used and the window size is changed gradually from 5×5 to 125×125. The offsets of the points in the azimuth direction are shown in Fig. 3.6, where the offsets of the CRs as well as the two buildings appear to be consistent on **a pixel level** but considerable dispersion within one pixel can also be observed, indicating that the quality of the coherent points are different. On the other hand, due to the change in the surface features between the two SAR acquisitions, offsets estimated for the point in the sea and that on the hill fluctuate randomly for up to 60 pixels. The results from these typical scatterers have shown that the proposed method can identify coherent points successfully.

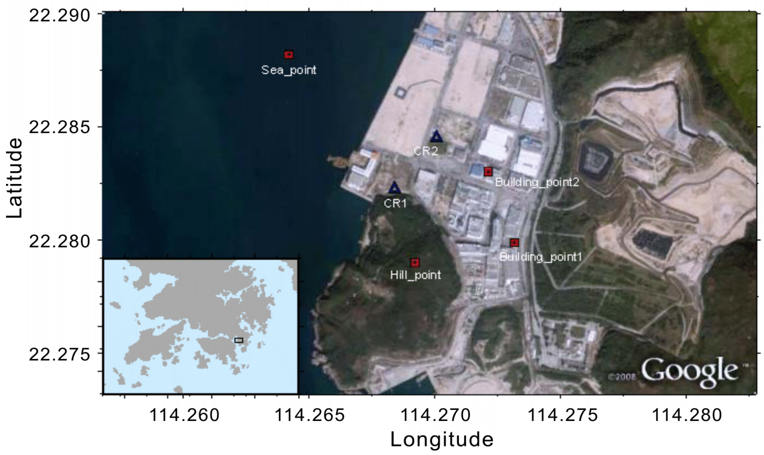

Fig. 3.5: The location map of corner reflectors together with other 4 test points superimposed on the Google Earth map.

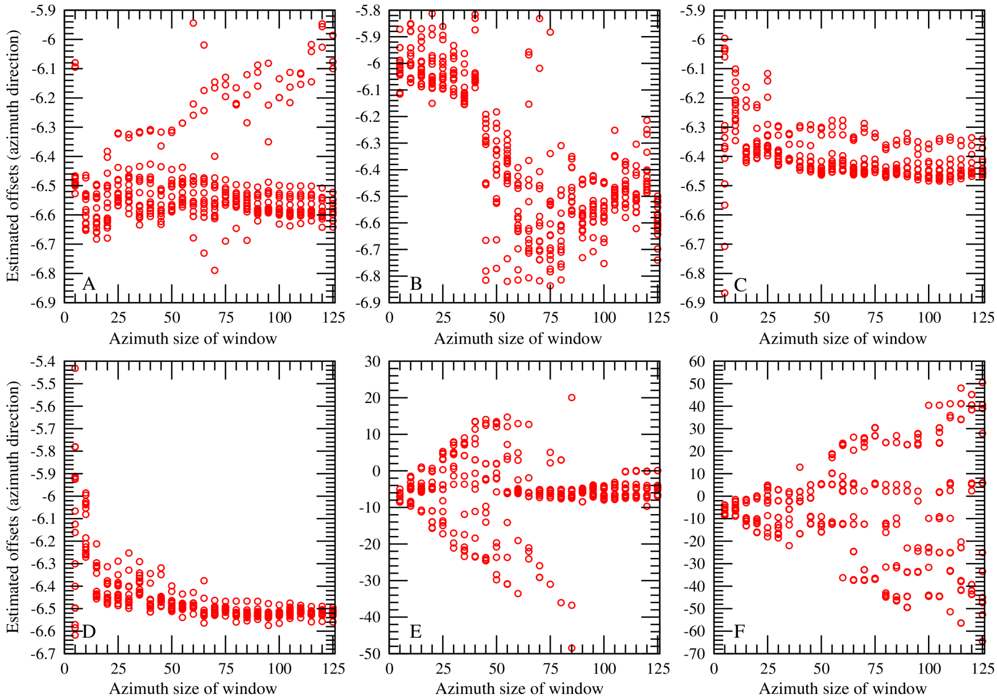

Fig. 3.6: Estimated azimuth offsets of two CR and other types of scatterers. The window size varies from 5-by-5 to 125-by-125 in the offset estimation. (A) CR1; (B) CR2; (C) Building point 1; (D) Building point 2; (E) Hill point; (E) Sea point.

3.3.2 Comparison of point selection methods

The SCR threshold [Adam, 2004], the coherence threshold [e.g., Berardino et al., 2002; Mora et al., 2003] and the newly proposed method (referred to as offset method hereafter for simplicity) are used for identifying coherent scatterers in the study area. For the offset method the range and the azimuth offsets at every pixel are estimated using image patch size of 3×15 . The 2-D histogram of the estimated offsets is shown in Fig. 3.6, indicating that the consistent range and azimuth offsets are -8 pixels and -5310 pixels respectively. After multilooking operation with a factor of 1×5 , 5613 TCP are finally selected (Fig. 3.8A). When the SCR method is used, 7355 points are selected with the threshold value set to be SCR>2 (Fig. 3.8B). 12153 points are selected with the coherence method (Fig. 3.8C), when the threshold is set to 0.4.

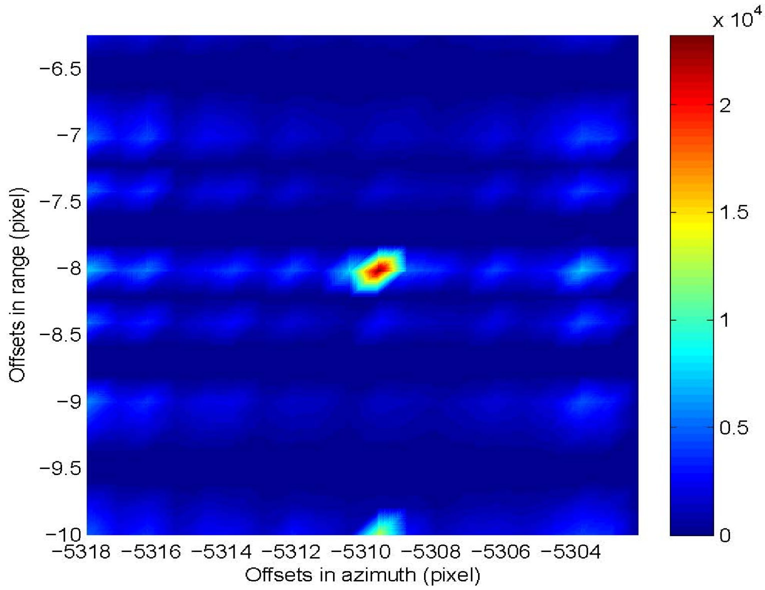

Fig. 3.7: 2D histogram of offsets at all pixels estimated using a window size of 3×15. The colour indicates the number of pixels whose offsets in range and azimuth direction locate in the corresponding intervals.

It can be seen from the results that all the three methods work well with strong scatterers. The number of points wrongly identified however varies considerably among the methods. Apparently the offset method works best in such areas as open water as no points is wrongly selected.

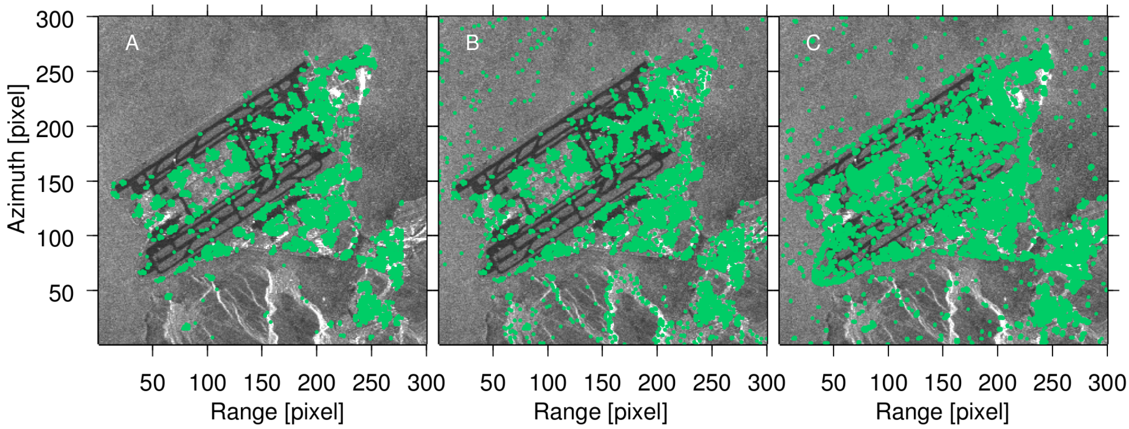

Fig. 3.8: Coherent scatterers identified with three different methods: (A) 5613 TCP identified with the offset method; (B) 7355 point identified with the SCR method when SCR>2; and (C) 12153 points identified with coherence method when the coherence threshold = 0.4 (coherence estimation window: 5×20).

3.3.3 TCP Coregistration

The identified TCP are resampled according to the polynomial determined based on the offsets of the TCP (referred to as TCP polynomial for simplicity). Errors in the polynomial will introduce phase noise as the polynomial gives the location of the TCP in the slave image where the interpolation kernel will be applied. For comparison, we also determine a polynomial with offsets from evenly distributed windows over the whole image and resampled the TCP with this polynomial (referred to as global polynomial for simplicity). It is found that the interferometric phases of the resampled TCP from the two polynomial approaches are different (Fig. 3.9A). The phase differences have a mean of 0.25 rad and a standard deviation of 2.3 rad. Since the global polynomial was estimated from offsets on distributed windows over the whole image where most of the pixels are distributed scatterers, the offsets from the distributed scatterers are unreliable and can affect the polynomial determination, resulting errors in the polynomial and phase noises. Fig. 3.9B shows the improvement in coherence when the TCP polynomial is used. It should be noted here that since the coherence estimator is biased, the estimated coherence is not as precise as expected, which is shown just for reference.

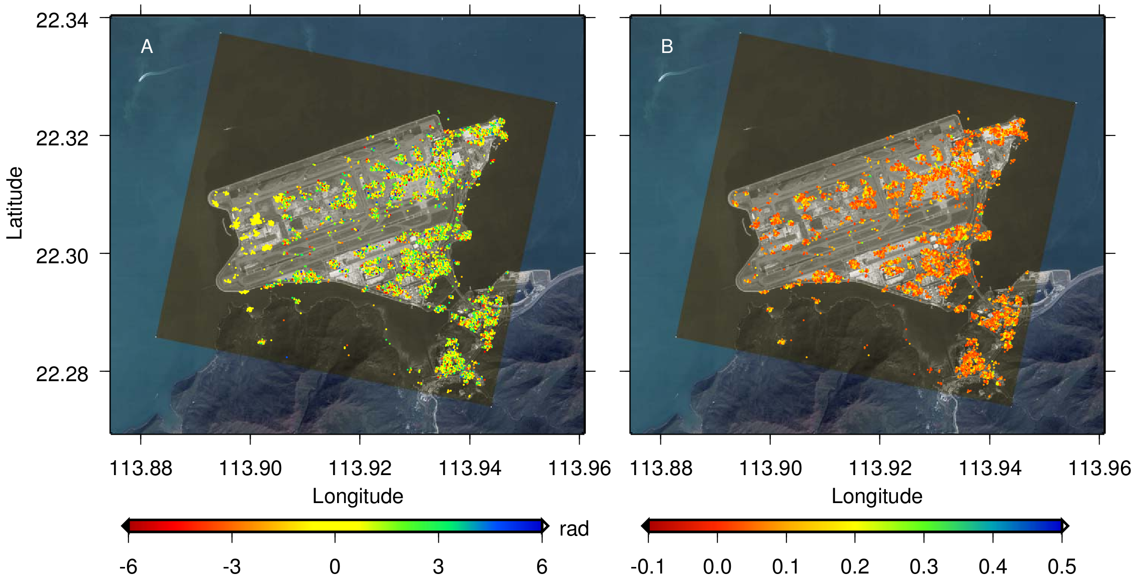

Fig. 3.9: (A) Phase differences between interferograms coregistered with different polynomials (unit: radian); and (B) Improvement in the coherence of the selected TCP when using the proposed coregistration strategy

3.3.4 TCP in MT-InSAR System

Since the TCPs are identified an interferogram by an interferogram, both the points that keep coherent in the whole time span of the observations and the points that only keep coherent in a subset of observation time span can be picked up. In areas undergoing rapid development, the number of points that keep coherent consistently is usually limited and the deformation pattern over the study area sometimes is hard to be fully reflected by these sparse points. Therefore it is necessary to explore points that only are coherent in a subset of the SAR data. The identification of such partially coherent points by the method proposed earlier is straightforward. Fig. 3.10 shows a location map of TCPs that appeared in at least 42 interferograms over Macau area. In this case a total of 81 interferograms with baselines less than 150m and 250 days respectively were generated from 38 Envisat/ASAR images. The details on the parameter estimation from these TCPs can be found in chapter 6.

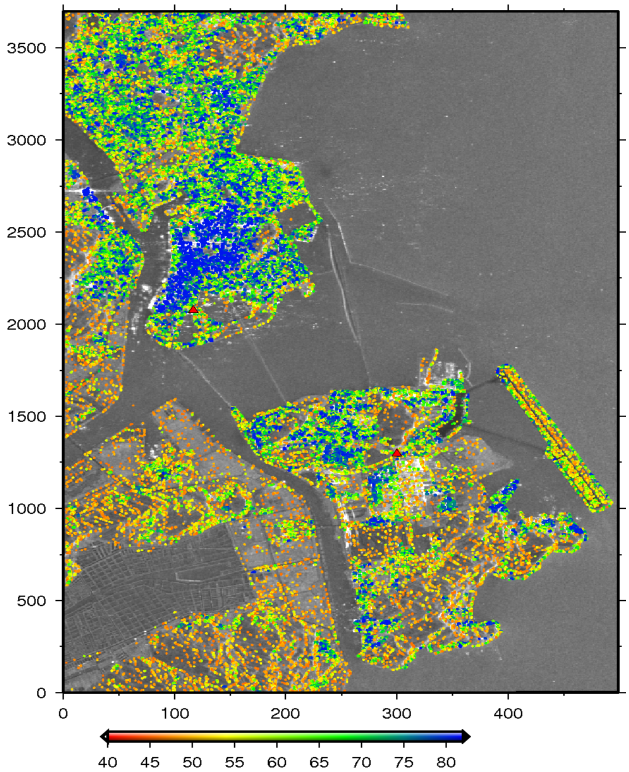

Fig. 3.10: TCPs that appeared in at least 42 interferograms over Macau area. The color shows in how many interferograms the points keep coherent.

3.4 Conclusion

A method for identifying temporarily coherent points (TCP) that exist between at least two SAR acquisitions has been presented in this chapter. The method is useful in areas where there are not enough SAR images to perform PSI analysis. The major advantage of the method is that it can identify coherent scatterers from a subset of interferograms without the need of setting the threshold based on operator's experience. The increased density of TCPs can reflect more deformation details especially in areas that undergo fast development. Moreover, an improved method for coregistering TCP has also been proposed by estimating the offset polynomial based on the TCP offsets only. The proposed algorithms have been validated using test data sets.

4 Deformation Parameter Estimation

After retrieving the phase components of the coherent points, MT-InSAR technique is required to estimate the deformation parameters. A careful literature survey has revealed that phase unwrapping is a vital step in all current MT-InSAR techniques. However the success in doing this can never be guaranteed. The performance of any MT-InSAR technique will be compromised if the phase ambiguities are wrongly estimated. Furthermore there is a lack of research on evaluating the precision of the estimated parameters in multiple master MT-InSAR system. For these reasons, it is desirable to develop an algorithm capable of estimating deformation patterns with no need of determining phase ambiguities and of providing the variance-covariance matrix of the estimated parameters. The algorithm to be presented in this chapter has the salient features:

» Multi-master interferograms with short spatial and temporal baselines are taken as basic observations

» The algorithm focuses on phase differences at TCP pairs (arcs) densely constructed by local triangulation.

» A phase ambiguity detector is proposed for removing arcs with phase ambiguities according to least squares residuals.

» Variance components of SLC images are estimated for evaluating the precision of deformation parameters.

4.1 Introduction

The emergence of techniques for analyzing multi-temporal SAR images has enhanced the ability of deformation mapping with InSAR [Lu et al., 2007]. Multi-temporal InSAR techniques, involving the processing of multiple-temporal InSAR images, provide a means to address issues in conventional InSAR techniques such as decorrelation and atmospheric artifacts. Over recent years, a multitude of approaches has been proposed in this domain, which can be broadly classified into two categories, permanent scatterers (PS) (or persistent scatterers as used in some literature) methods [Colesanti et al., 2003; Ferretti et al., 2000; Hooper, 2004; Shanker and Zebker, 2010; Werner et al., 2003] and small baseline subset (SBAS) InSAR methods [Berardino et al., 2002; Usai, 2003]. Since both types of techniques require the reliable estimation of phase ambiguities which is still a tough problem in the InSAR field, errors induced from phase unwrapping will make current MTInSAR techniques fail to correctly estimate the parameters (deformation, DEM error, and atmospheric delay) from a stack of interferograms.

How to reduce or avoid errors on the estimation of phase ambiguities is therefore a challenge that all multi-temporal InSAR methods need to overcome. In applying such techniques we have found that for a set of multi-master interferograms with short baselines, there are usually a sufficient number of arcs in which the double-difference phase components are immune from phase ambiguities provided that the selected coherent points are densely connected. Especially considering that fact that the high-resolution SAR data with rather short repeating cycles acquired by modern SAR sensors (such as TerraSAR-X, COSMO-SkyMed, and Radarsat-2) are increasingly available, the dense arcs without phase ambiguities can be largely ensured even for areas with rapid ground deformation. If only these arcs are taken as observations for estimating the DEM errors and deformations, the complexity of parameter estimation can be reduced significantly since there is no need of estimating phase ambiguities anymore. In this chapter we propose a least squares based method that can identify arcs without phase ambiguities (or on which the phase ambiguity equals to zero) and resolve reliably the deformation parameters (linear or non-linear) at coherent points. We first use a network construction strategy that performs Delaunay triangulation locally to ensure that coherent points can be connected as much as possible while not significantly increasing the computational complexity. A least squares based model is then proposed for parameter estimation during which an phase ambiguity detector is used to identify and remove arcs with phase ambiguities according to the least squares residuals. Considering the stochastic nature of SAR observations, we introduce a weighting scheme for the interferometric phases at arcs by applying the law of variance propagation [Koch, 1988; Teunissen, 2000; Kampes, 2006]. The parameters at the coherent points are then estimated by applying a least squares model constrained by reference points. The proposed approach is tested with a set of simulated SAR data to ensure the proposed method functions as expected under controlled circumstances.

4.2 Modeling SAR interferograms

4.2.1 TCP network

Once the TCP are identified, a network is constructed to connect pairs of TCPs where each connected pair is termed an arc as in PSInSAR terminology. Delaunay triangulation has been widely used for this purpose. However Delaunay triangulation defines a triangular network under the condition that the circumcircles of all the triangles in the network are empty without considering the lengths of the arcs (see Fig. 4.1(a)). Although arcs longer than a certain length can be removed in the final step, the points are not connected densely enough. If only points in a small region (i.e. 1500 m×1500 m) are connected, the problem of arc length can be solved without increasing significantly the computational complexity and the density of arcs can also be improved. Fig. 4.1(c) shows a local Delaunay triangulation where a grid with 100 m spacing is placed over an interferogram and points in a circle with a radius of 750 m centered at each grid node are selected and connected. It should be noted that high density of arcs is important for the parameter estimation to be presented in the following section, since denser network ensures at more arcs the phase ambiguity is zero.

4.2.2 Multi-master Interferogram stacking

Considering $J+1$ SAR images acquired in an ordered time sequence, we generate I interferograms with short baselines (say, less than 150 m). In each interferogram i, the line-of-sight (LOS) displacement of TCP (l,m) can be described by a linear combination of the mean deformation rate between the acquisitions and the corresponding time span. Given two acquisitions, one is the master (M) image and the other is the slave (S) image and M is acquired later than S, i.e., $t_{M_i} > t_{S_i}$. The LOS deformation ($\Delta r_{l,m}^i$) during this time period can be expressed as

$$\Delta r_{l,m}^i = r(t_{M_i}, l, m) - r(t_{S_i}, l, m) = \sum_{k=1}^{C_i - 1} (t_k - t_{k-1}) v_k \tag{4.1}$$

Where (l,m) are the pixel coordinates of the TCP; $r(t_{M_i}, l, m)$ and $r(t_{S_i}, l, m)$ are the slant range distances from the master and the slave sensors respectively to the target; and C_i is the number of SLC acquisitions in the time sequence from S_i to M_i (including M_i and S_i).

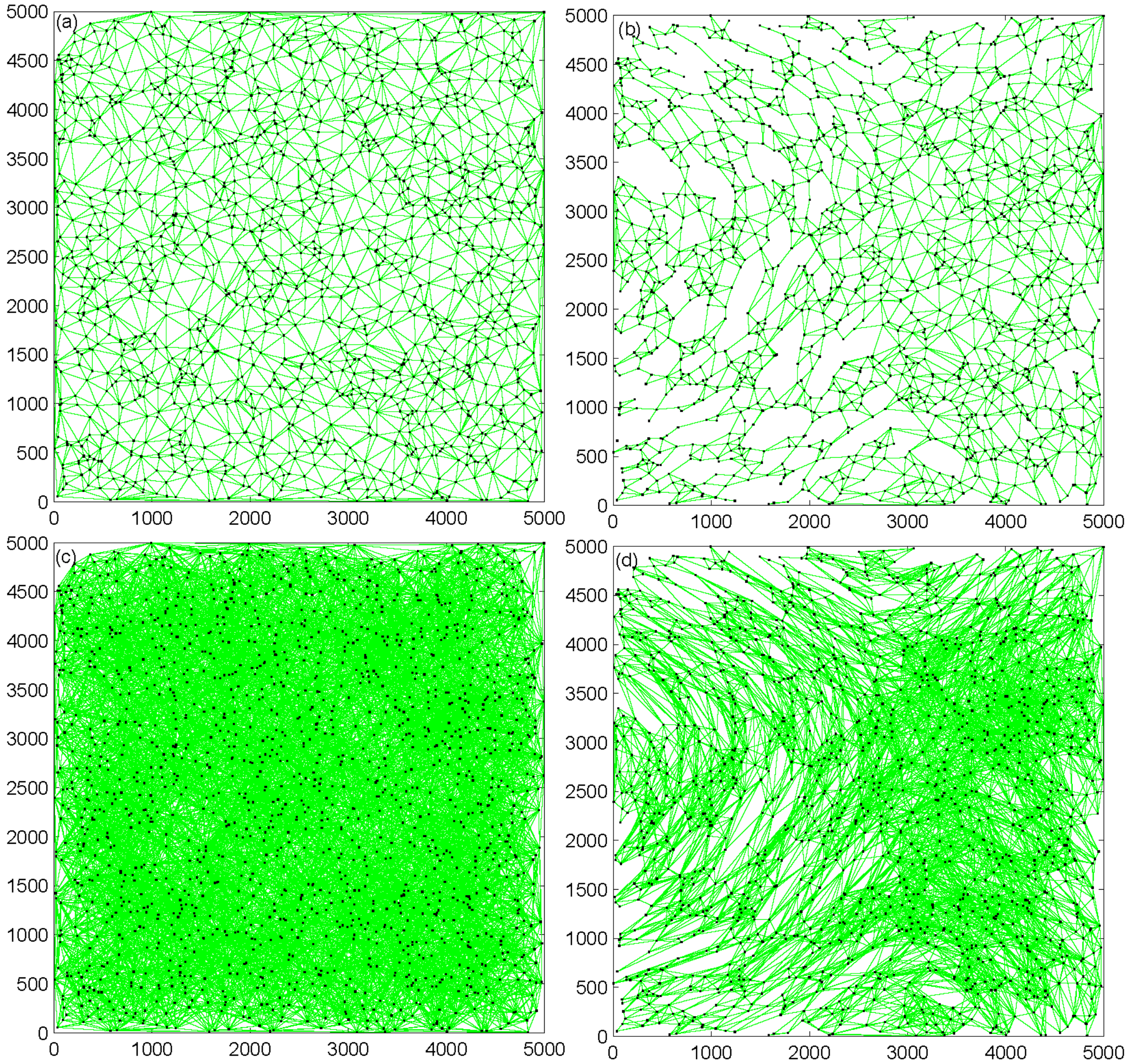

Fig. 4.1: (a) Global Delaunay triangulation network of coherent points; (b) Network after removing arcs with phase ambiguities detected from (a); (c) Local Delaunay triangulation network of coherent points; (d) Network after removing arcs with phase ambiguities detected from (c).

As Eq. (4.1) is a combination of LOS deformation estimates at the full time resolution, there is a risk of over-parameterization in the equation, which should be carefully dealt with in a real application. If a linear deformation rate (v) during the whole time span is assumed, then $v_1 = \cdots = v_k = \cdots = v$. Eq. (4.1) can also be tailored as any combination of deformation rates and time intervals in order to compare with field measurements that, for example, are performed annually. The corresponding phase is

$$\phi^{i}_{defo,l,m} = -\frac{4\pi}{\lambda}\sum_{k=1}^{C_i-1}(t_k - t_{k-1})v_k = \beta_i \boldsymbol{V} \tag{4.2}$$

where λ is the radar wavelength; $\boldsymbol{V}$ is a vector of deformation rates; β_i is the coefficient corresponding to the unknown deformation rates that can be expressed as $\beta_i = -(4\pi/\lambda)\boldsymbol{T_i}$ and $\boldsymbol{T_i}$ is a vector of time combinations whose elements correspond to the deformation rates within the respective time intervals .

$$\boldsymbol{T_i} = \begin{bmatrix} t_1 - t_0 & t_2 - t_1 & \cdots & t_k - t_{k-1} & \cdots & t_J - t_{J-1} \end{bmatrix}_{I\times J} \tag{4.3}$$

The wrapped phase of a TCP with a pixel coordinate (l,m) can be written as

$$\phi^{i}_{l,m} = W\{\phi^{i}_{topo,l,m} + \phi^{i}_{defo,l,m} + \phi^{i}_{atmo,l,m} + \phi^{i}_{orbit,l,m} + \phi^{i}_{dop,l,m} + \phi^{i}_{noise,l,m}\} \tag{4.4}$$

where $W\{\cdot\}$ represents the wrapping operator, $\phi^{i}_{topo,l,m}$ is the phase related to the topographic error; $\phi^{i}_{atmo,l,m}$ is the phase due to the differential atmospheric delays between the acquisitions; $\phi^{i}_{orbit,l,m}$ is the phase due to the orbit errors; $\phi^{i}_{dop,l,m}$ is the phase component due to azimuth Doppler centroid difference between the acquisitions; and $\phi^{i}_{noise,l,m}$ is the noise term that includes potentially the thermal noise, processing errors and decorrelation errors. The $\phi^{i}_{topo,l,m}$ term has a direct relationship with the height error $\Delta h_{l,m}$

$$\phi^{i}_{topo,l,m} = -\frac{4\pi}{\lambda}\frac{B^{i}_{perp,l,m}}{r^{i}_{l,m}\sin\theta^{i}_{l,m}}\Delta h_{l,m} = \alpha^{i}_{l,m}\Delta h_{l,m} \tag{4.5}$$

where $B^{i}_{perp,l,m}$ is the local perpendicular baseline; $r^{i}_{l,m}$ is the slant range distance from the master sensor to the target; $\theta^{i}_{l,m}$ is the local incidence angle.

The phase difference between two TCPs located at (l,m) and (l',m') is given by

$$\begin{aligned} \Delta\phi^{i}_{l,m,l',m'} &= W\{\alpha^{i}_{l,m,l',m'}\Delta h_{l,m,l',m'} + \beta_i \Delta \boldsymbol{V} + \omega^{i}_{l,m,l',m'}\} \\ \omega^{i}_{l,m,l',m'} &= \Delta\phi^{i}_{atmo,l,m'l',m'} + \Delta\phi^{i}_{orbit,l,m,l',m'} + \Delta\phi^{i}_{dop,l,m,l',m'} + \Delta\phi^{i}_{noise,l,m,l',m'} \end{aligned} \tag{4.6}$$

where $\Delta\boldsymbol{V} = \left[\Delta v^{1}_{l,m,l',m'} \quad \Delta v^{2}_{l,m,l',m'} \quad \cdots \quad \Delta v^{I}_{l,m,l',m'}\right]^{T}$. Since the atmospheric artifacts are strongly correlated in space, the differential atmospheric contributions between a pair of nearby TCP are exptected to be small [Li et al., 2006; Williams et al., 1998]). The differential orbital component generally has a similar characteristic. Since the differencing operation can also significantly reduce the effects of Doppler centroid differences, the magnitude of $\Delta\phi^{i}_{dop,l,m,l',m'}$ should be very small. Moreover, if neither of the two connected TCPs is significantly affected by decorrelation, $\Delta\phi^{i}_{noise,l,m,l',m'}$ will also show a low variance. Therefore $\omega^{i}_{l,m,l',m'}$ can be safely taken as a random variable with an expectation $E(\omega^{i}_{l,m,l',m'})=0$. For a given arc, the system of observation equations can be written as

$$\begin{aligned} \boldsymbol{\Delta\Phi} &= \boldsymbol{A}\begin{bmatrix}\Delta h_{l,m,l',m'} \\ \boldsymbol{\Delta V} \\ \boldsymbol{K}\end{bmatrix} + \boldsymbol{W} \\ \boldsymbol{\Delta\Phi} &= \left[\Delta\phi^{1}_{l,m,l',m'} \quad \Delta\phi^{2}_{l,m,l',m'} \quad \cdots \quad \Delta\phi^{I}_{l,m,l',m'}\right]^{T} \\ \boldsymbol{A} &= \left[\alpha \quad \beta \quad 2\pi\right] \\ \boldsymbol{\alpha} &= \left[\alpha^{1}_{l,m} \quad \alpha^{2}_{l,m} \quad \cdots \quad \alpha^{I}_{l,m}\right]^{T} \\ \boldsymbol{\beta} &= \left[\beta_1 \quad \beta_2 \quad \cdots \quad \beta_I\right]^{T} \\ \boldsymbol{W} &= \left[\omega^{1}_{l,m,l',m'} \quad \omega^{2}_{l,m,l',m'} \quad \cdots \quad \omega^{I}_{l,m,l',m'}\right]^{T} \end{aligned} \tag{4.7}$$

where $\boldsymbol{\Delta\Phi}$ is a vector containing the phase differences between two adjacent pixels in a total of I interferograms; $\boldsymbol{A}$ is the design matrix including height-to-phase conversion factors, the time combination matrix and 2π ; $\boldsymbol{K}$ is the integer vector containing the number of phase ambiguities and $\boldsymbol{W}$ is a stochastic vector.

4.3 Least squares solution

Assuming that at all arcs the phase ambiguity equals to zero, i.e., $\boldsymbol{K}=\boldsymbol{0}$, the system of observations can be simplified as

$$\boldsymbol{\Delta\Phi} = \boldsymbol{A}\begin{bmatrix}\Delta h_{l,m,l',m'} \\ \boldsymbol{\Delta V}\end{bmatrix}+\boldsymbol{W} \tag{4.8}$$

Where $\boldsymbol{A}=[\alpha \quad \beta]$. The functional and the stochastic models of the system of observations can be expressed as

$$\begin{aligned} E\{\boldsymbol{\Delta\Phi}\} &= \boldsymbol{A}\begin{bmatrix}\Delta h_{l,m,l',m'} \\ \boldsymbol{\Delta V}\end{bmatrix} \\ D\{\boldsymbol{\Delta\Phi}\} &= \boldsymbol{Q^{arc}} \end{aligned} \tag{4.9}$$

where ($E\{\boldsymbol{\Delta\Phi}\}$) and ($D\{\boldsymbol{\Delta\Phi}\}$) are operators for expectation and dispersion respectively, and $\boldsymbol{Q^{arc}}$ is an $I\times I$ covariance matrix of differential phases at arcs. This functional model reflects the linear or linearized relationship between the observations and the unknown parameters while the stochastic model describes the precision of the observations and the correlation between them. In this section a weighted least squares estimator is used to resolve the parameters in Eq. (4.8) and (4.9).

4.3.1 Priori variance components

In the conventional MT-InSAR analysis techniques, all pixels or the double difference observations are assumed to have equal weights. This assumption may not be valid since SAR images are acquired under different conditions with which the atmospheric artifacts and random noises vary. For the SAR images considered, the VC matrix of the random noises ($\boldsymbol{Q}_{noise}$) can be expressed as

$$\boldsymbol{Q}_{noise} = \begin{bmatrix} \sigma^2_{noise_0} & & \\ & \ddots & \\ & & \sigma^2_{noise_{J0}} \end{bmatrix}_{(J+1)\times(J+1)} \tag{4.10}$$

where it is assumed that the noise of TCPs not including the atmospheric artifacts is uncorrelated and equals to the average noise level of the SLC images . When I interferograms are formed from the $J+1$ images, the VC matrix of the interferogams ($\boldsymbol{Q}^{\mathbf{in}}_{noise}$) is given according to the law of variance propagation

$$\boldsymbol{Q}^{in}_{noise} = \boldsymbol{D}\,\boldsymbol{Q}_{noise}\,\boldsymbol{D}^T \tag{4.11}$$

where $\boldsymbol{D}$ is a combination matrix indicating which pair of SLC images are used to generate the interferograms. The combination matrix has the following form.

$$\boldsymbol{D} = \begin{bmatrix} -1 & 0 & 1 & \cdots & 0 \\ 0 & -1 & \cdots & 1 & 0 \\ \vdots & \ddots & & & \\ 0 & 0 & -1 & \cdots & 1 \end{bmatrix}_{I\times(J+1)} \tag{4.12}$$

Since the phase differences at a given arc is the observations of the model, in the ith interferogram the VC matrix of the phase difference is strictly given as

$$Q^{arc}_i = \begin{pmatrix} 1 & -1 \end{pmatrix} \begin{bmatrix} \sigma^2_{l,m,i} & \sigma_{l,m,l',m'i} \\ \sigma_{l,m,l',m'i} & \sigma^2_{l',m',i} \end{bmatrix} \begin{pmatrix} 1 \\ -1 \end{pmatrix} \tag{4.13}$$

Where $\sigma^2_{l,m,i}$ and $\sigma^2_{l',m',i}$ are the variance component of the points (l,m) and (l',m') ; $\sigma_{l,m,l',m'i}$ is their corresponding covariance component. It is clear that the two points at the ends of the arc are correlated due to the signals caused by the atmospheric delay and orbital inaccuracy. Here we assume that for an arc with short distance, spatially correlated signals at the two ends are the same, i.e., $\sigma_{l,m,l',m'i}=0$. In addition, for the seek of simplicity, we follow the assumption raised by Kampes [2006] that all points in an interferogram have the same inherent noise level, i.e., $\sigma^2_{l,m,i} = \sigma^2_{l',m',i} = \sigma^2_{noise,i}$. The VC matrix of the double-difference phases then reduces

$$\boldsymbol{Q}^{arc} = 2\boldsymbol{Q}^{in}_{noise} = 2\boldsymbol{D}\boldsymbol{Q}_{noise}\boldsymbol{D}^T \tag{4.14}$$

It is worth noting that this simplicity is not strictly correct, however it is helpful to estimate the average noise level of the whole coherent points (i.e., $\boldsymbol{Q}_{noise}$) [Kampes, 2006] (rather than each single point) at an acceptable precision without much computational complexity. The weights ($\boldsymbol{P}^{arc}$) of the double-difference phases can be obtained by taking the inverse of the VC matrix. Since it is possible that the VC matrix is singular, a pseudo inverse of the VC matrix, i.e., $\boldsymbol{P}^{arc} = (\boldsymbol{Q}^{arc})^+$, can be obtained by singular value decomposition (SVD) [Rao and Mitra, 1971].

4.3.2 Initial estimation

The least squares solution of the observation equations is

$$\begin{aligned} \begin{bmatrix} \Delta\hat{h}_{l,m,l',m'} \\ \Delta\hat{\boldsymbol{V}} \end{bmatrix} &= (\boldsymbol{A}^T\boldsymbol{P}^{arc}\boldsymbol{A})^{-1}\boldsymbol{A}^T\boldsymbol{P}^{arc}\Delta\boldsymbol{\Phi} \\ \Delta\hat{\boldsymbol{\Phi}} &= \boldsymbol{A}(\boldsymbol{A}^T\boldsymbol{P}^{arc}\boldsymbol{A})^{-1}\boldsymbol{A}^T\boldsymbol{P}^{arc}\Delta\boldsymbol{\Phi} \\ \hat{\boldsymbol{w}} &= \Delta\boldsymbol{\Phi} - \boldsymbol{A}(\boldsymbol{A}^T\boldsymbol{P}^{arc}\boldsymbol{A})^{-1}\boldsymbol{A}^T\boldsymbol{P}^{arc}\Delta\boldsymbol{\Phi} \end{aligned} \tag{4.15}$$

where the circumflex $\hat{}$ denotes estimated quantities; and $\hat{\boldsymbol{w}}$ is the least squares residuals. The corresponding VC matrices of the estimated quantities are

$$\begin{aligned} D\left\{\begin{bmatrix} \Delta\hat{h}_{l,m,l',m'} \\ \Delta\hat{\boldsymbol{V}} \end{bmatrix}\right\} &= (\boldsymbol{A}^T\boldsymbol{P}^{arc}\boldsymbol{A})^{-1} \\ D\{\Delta\hat{\boldsymbol{\Phi}}\} &= \boldsymbol{A}(\boldsymbol{A}^T\boldsymbol{P}^{arc}\boldsymbol{A})^{-1}\boldsymbol{A}^T \\ D\{\hat{\boldsymbol{w}}\} &= \boldsymbol{Q}_{arc} - \boldsymbol{A}(\boldsymbol{A}^T\boldsymbol{P}^{arc}\boldsymbol{A})^{-1}\boldsymbol{A}^T \end{aligned} \tag{4.16}$$

4.3.3 Phase ambiguity detection

A basic assumption of least squares estimation is that all the gross errors and systematic effects have been eliminated before the adjustment computation is performed. However during the initial least squares estimation we assume that at all arcs phase ambiguity equals to zero, which is absolutely wrong for arcs with non-zero ambiguities. Therefore it is necessary to detect the arcs with non-zero phase ambiguities and remove them from the solution. Since it is observed that phase ambiguities can result in abnormally large residuals during least squares, they can be taken as “outliers”. Methods based on statistical tests of the estimated least squares residuals are often used for the detection of oultiers [*Koch*, 1988]. However, they are inefficient as statistical testing should be carried out for each of the iterative least squares solutions. Because double difference phases with phase ambiguities ($N \cdot 2\pi, N \in \mathbb{Z}$) render the magnitude of the corresponding residuals to increase significantly as shown in Fig.4.2. It is obvious that the abnormally large residuals can be used to isolate the arcs having phase ambiguities. In addition since we are just interested in whether the arcs have ambiguities or not and there is no need to detect exactly which interferograms have ambiguities, we use a simplified phase ambiguity detector [*Jia*, 1984]

$$Max\left(\left|\hat{w}_i\right|\right) > c\sqrt{Max\left(\left(\mathbf{Q}_{arc}\right)_{ii}\right)} + 2\sqrt{Max\left(\left(\mathbf{Q}_{\Delta\hat{\Phi}\Delta\hat{\Phi}}\right)_{ii}\right)} \tag{4.17}$$

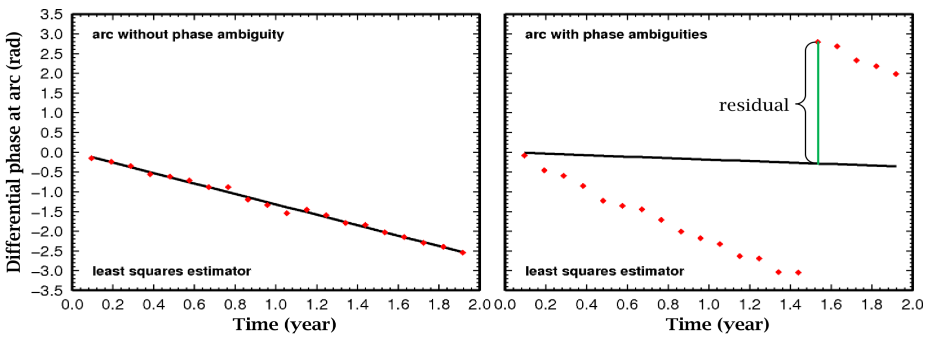

Fig. 4.2: Residuals arose from least squares at an arc without phase ambiguity (left) and the one with ambiguities (right)

where $Max(\cdot)$ means the maximum value in a vector or matrix. According to [*Jia*, 1984] the constant can be 3 or 4. When the threshold value in Eq. (4.17) is reached, the i-th observation is considered an outlier at 95% confidence level. It should be noted that since currently only the priori VC matrix is available, the detector should be performed in a conservative manner by setting a small constant c to ensure arcs with phase ambiguities can be removed. Once the precise VC matrix is obtained based on the method to be introduced in the next section, we will perform the detection again. As an alternative, since the arcs possessing phase ambiguities can introduce large residuals, they can also be removed according to the histogram of residuals. It should also be noted that in areas where there are not abundant SAR data and the deformation undergoes rapidly the removing of arcs might result in a set of sub-networks which will bring difficulties to the integration operation from arcs to points. To overcome this problem we can increase the density of arcs and/or remove the image pairs with large deformation signal. We can also employ the robust method (like L1 norm) to estimate the parameters. As shown in (Zhang et al., 2011c), with a robust estimator, parameters can be resolved without removing arcs.

4.3.4 Variance component estimation

During the initial estimation since the stochastic model for the observation system is not known adequately, we simply assumed a priori model under the assumption that the interferometric phase error for TCPs is expected to be below a certain value (say, 20° [Kampes, 2006]) to estimate the parameters in the context of least squares. However optimal estimation can never be achieved without a correct stochastic model. In this Section an approach of variance component estimation (VCE) is proposed for the multiple master MT-InSAR system aiming to precisely describe the qualities of the measurements and to reliably evaluate the precision of the estimated parameters. The following derivation of VCE is based on

(Li, 2009), which, compared with the quadratic norm based method, is easier to be implemented.

The residual expression in Eq. (4.15) which is the fundamental equation for VCE, can be rewritten as

$$\begin{aligned}\hat{\boldsymbol{w}} &= \boldsymbol{R}\Delta\boldsymbol{\Phi}\\ \boldsymbol{R} &= \boldsymbol{I}_I - \boldsymbol{A}\left(\boldsymbol{A}^T(\boldsymbol{Q}^{\boldsymbol{arc}})^{+}\boldsymbol{A}\right)^{-1}\boldsymbol{A}^T(\boldsymbol{Q}^{\boldsymbol{arc}})^{+}\end{aligned} \tag{4.18}$$

where $\boldsymbol{I}_I$ is the $I\times I$ identity matrix, and $\boldsymbol{R}$ is an idempotent matrix satisfying

$$\begin{gathered}\boldsymbol{R}\boldsymbol{R}=\boldsymbol{R},\ \ \boldsymbol{RA}=\boldsymbol{0},\ \ \boldsymbol{R}^T(\boldsymbol{Q}^{\boldsymbol{arc}})^{+}=(\boldsymbol{Q}^{\boldsymbol{arc}})^{+}\boldsymbol{R}\\ tr(\boldsymbol{R})=rk(\boldsymbol{R})=r\end{gathered} \tag{4.19}$$

where $tr(\cdot)$ and $rk(\cdot)$ are operators for computing the trace and rank of a matrix, and r is the redundancy of the system of observations. Based on the LS residuals, the equation for VCE can be established as

$$\boldsymbol{R}\boldsymbol{Q}^{arc}\boldsymbol{R}^T=\boldsymbol{R}E(\boldsymbol{W}\boldsymbol{W}^T)\boldsymbol{R}^T=E(\hat{\boldsymbol{w}}\hat{\boldsymbol{w}}^T) \tag{4.20}$$

where $E(\cdot)$ represents the expectation of a variable. It should be noted that the VCE has to be preformed iteratively and an initial covariance matrix $\boldsymbol{Q}_0^{arc}$ (which can be determined based on the priori standard errors of SLC images)must be given. The fundamental equation for the iterative VCE becomes

$$\begin{gathered}\boldsymbol{R}_0\boldsymbol{Q}^{arc}\boldsymbol{R}_0^T=\hat{\boldsymbol{w}}_0\hat{\boldsymbol{w}}_0^T\\ \boldsymbol{R}_0=\boldsymbol{I}_I-\boldsymbol{A}\left(\boldsymbol{A}^T(\boldsymbol{Q}_0^{arc})^{+}\boldsymbol{A}\right)^{-1}\boldsymbol{A}^T(\boldsymbol{Q}_0^{arc})^{+}\end{gathered} \tag{4.21}$$

where $\hat{\boldsymbol{w}}_0=\boldsymbol{R}_0\Delta\boldsymbol{\Phi}$. The linear relationship between $\boldsymbol{Q}^{arc}$ and its elements can be expressed as

$$\boldsymbol{Q}^{arc}=\boldsymbol{U}_{\boldsymbol{1}}^{\boldsymbol{arc}}\theta_1^{arc}+\boldsymbol{U}_{\boldsymbol{2}}^{\boldsymbol{arc}}\theta_2^{arc}+\cdots+\boldsymbol{U}_{\boldsymbol{m}}^{\boldsymbol{arc}}\theta_m^{arc}=\sum_{i=1}^{m}\boldsymbol{U}_{\boldsymbol{i}}^{\boldsymbol{arc}}\theta_i^{arc} \tag{4.22}$$

where θ_i^{arc} is the ith unknown variance or covariance of interferometric phase and $\boldsymbol{U}_{\boldsymbol{i}}^{\boldsymbol{arc}}$ is the given definite matrix for the variance component of θ_i^{arc} having the form as

$$\boldsymbol{U}_{\boldsymbol{i}}^{\boldsymbol{arc}}=\begin{bmatrix}0 & 0 & 0\\ 0 & 1_{i,i} & 0\\ 0 & 0 & 0\end{bmatrix}\ (i\leqslant k);\ \ \boldsymbol{U}_{\boldsymbol{i}}^{\boldsymbol{arc}}=\begin{bmatrix}0 & 0 & 0 & 0 & 0\\ 0 & 0 & 0 & 1_{j,l} & 0\\ 0 & 0 & 0 & 0 & 0\\ 0 & 1_{l,j} & 0 & 0 & 0\\ 0 & 0 & 0 & 0 & 0\end{bmatrix}\ (k<i\leqslant m) \tag{4.23}$$

Under the assumption that the first k elements are variance components and the $(m-k)$ elements are covariance components. Since $\hat{\boldsymbol{w}}_0\hat{\boldsymbol{w}}_0^T$ is a matrix, Eq. (4.21) can be transformed into a vector form as

$$vec\left(\boldsymbol{R}_0\boldsymbol{Q}^{arc}\boldsymbol{R}_0^T\right)=vec\left(\hat{\boldsymbol{w}}_0\hat{\boldsymbol{w}}_0^T\right) \tag{4.24}$$

where $vec(\cdot)$ denotes the vector operator that converts a matrix t a column by stacking one column of this matrix underneath the previous one. It should be noted the number of residuals for a given arc is $\boldsymbol{I}$ while the number of variance and covariance elements of $\boldsymbol{Q}^{arc}$ is $\boldsymbol{I}(\boldsymbol{I}+1)/2$ indicating that the residuals cannot provide enough information for the estimation of VC-matrix of double difference observations. Since there is a simplified relationship between VC-matrix of double difference observations and the variance matrix of the SLC images shown in section 4.3.1, according to the variance propagation, we can estimate the variance matrix of the SLC images instead, which can be expressed as

$$\boldsymbol{Q}_{noise}=\boldsymbol{U}_{\boldsymbol{1}}\theta_1+\boldsymbol{U}_{\boldsymbol{2}}\theta_2+\cdots+\boldsymbol{U}_{J+1}\theta_{J+1}=\sum_{j=1}^{J+1}\boldsymbol{U}_j\theta_j \tag{4.25}$$

Where θ_j is the variance component of the jth unknown parameter. According to the relationship between $\boldsymbol{Q}_{noise}$ and $\boldsymbol{Q}^{arc}$ shown in Eq.(4.12), we have

$$\boldsymbol{Q}^{arc}=\sum_{i=1}^{m}\boldsymbol{U}_{\boldsymbol{i}}^{\boldsymbol{arc}}\theta_i^{arc}=\sum_{j=1}^{J+1}\boldsymbol{U}_j^{slc}\theta_j \tag{4.26}$$

where $\boldsymbol{U}_j^{slc}=2\boldsymbol{D}\boldsymbol{U}_{\boldsymbol{j}}\boldsymbol{D}^T$ .Let $(\boldsymbol{Q}_0^{arc})$ be the initial VC-matrix of double-difference observations. The corresponding weight matrix $(\boldsymbol{Q}_0^{arc})^+$ can be expanded as

$$(\boldsymbol{Q}_0^{arc})^+=(\boldsymbol{Q}_0^{arc})^+(\boldsymbol{Q}_0^{arc})(\boldsymbol{Q}_0^{arc})^+=(\boldsymbol{Q}_0^{arc})^+\sum_{j=1}^{J+1}\boldsymbol{U}_j^{slc}\theta_j^0(\boldsymbol{Q}_0^{arc})^+=\sum_{j=1}^{J+1}\tilde{\boldsymbol{P}}_j\theta_j^0 \tag{4.27}$$

where $\tilde{\boldsymbol{P}}_j=(\boldsymbol{Q}_0^{arc})^+\boldsymbol{U}_j^{slc}(\boldsymbol{Q}_0^{arc})^+$. Considering Eq. (4.19), we have

$$(\boldsymbol{Q}_0^{arc})^+\boldsymbol{R}_0\boldsymbol{Q}^{arc}\boldsymbol{R}_0^T=(\boldsymbol{Q}_0^{arc})^+\hat{\boldsymbol{w}}_0\hat{\boldsymbol{w}}_0^T \tag{4.28}$$

Substituting Eq. (4.26) and Eq. (4.27) into Eq. (4.28), we have

$$\sum_{j=1}^{J+1}\tilde{\boldsymbol{P}}_j\boldsymbol{R}_0\boldsymbol{Q}^{arc}\boldsymbol{R}_0^T=\sum_{j=1}^{J+1}\tilde{\boldsymbol{P}}_j\hat{\boldsymbol{w}}_0\hat{\boldsymbol{w}}_0^T \tag{4.29}$$

By taking the trace of both sides of Eq. (4.29), a linear system of observation equations with $J+1$ unknown variance components arises as

$$\begin{bmatrix} tr\left(\boldsymbol{R}_0^T\tilde{\boldsymbol{P}}_1\boldsymbol{R}_0\boldsymbol{U}_1\right) & \cdots & tr\left(\boldsymbol{R}_0^T\tilde{\boldsymbol{P}}_1\boldsymbol{R}_0\boldsymbol{U}_{J+1}\right) \\ \vdots & \ddots & \vdots \\ tr\left(\boldsymbol{R}_0^T\tilde{\boldsymbol{P}}_{J+1}\boldsymbol{R}_0\boldsymbol{U}_1\right) & \cdots & tr\left(\boldsymbol{R}_0^T\tilde{\boldsymbol{P}}_{J+1}\boldsymbol{R}_0\boldsymbol{U}_{J+1}\right)\end{bmatrix}\begin{bmatrix}\hat{\theta}_1 \\ \vdots \\ \hat{\theta}_{J+1}\end{bmatrix}=\begin{bmatrix}\hat{\boldsymbol{w}}_0^T\tilde{\boldsymbol{P}}_1\hat{\boldsymbol{w}}_0 \\ \vdots \\ \hat{\boldsymbol{w}}_0^T\tilde{\boldsymbol{P}}_{J+1}\hat{\boldsymbol{w}}_0\end{bmatrix} \tag{4.30}$$

The vector of variance components of the SLC images can be directly estimated from Eq. (4.30) by least squares. The reasons that we estimate the variance components of the SLC images instead of the variance and covariance of interferograms are (1) interferograms are the linear combination of SLC images; (2) the number of components to be estimated for SLC images is far fewer than that for interferograms; (3) the number of residuals (i.e., the observations for VCE) is not enough for the estimation of unknown VC components of interferograms.

Here we adopted a similar strategy used in [Kampes, 2006] for variance component estimation. First we construct arcs from the TCPs ensuring each TCP is used only once. Then we estimate the parameters with the a priori variance components for these arcs and remove arcs having phase ambiguities by the outlier detector presented in the previous Section. Finally we use the LS residuals of all the remaining arcs to perform the VCE.

4.3.5 Final estimation

With the estimated variance components of the SLC images, the least squares estimator can be performed again for all the arcs constructed by local triangulation and the outlier detector can also be updated to remove the arcs with phase ambiguities using the estimated VC matrix. Compared with the integer least squares estimator and the method based on maximization of the ensemble coherence, the proposed method determines more efficiently and reliably the DEM errors and the differential deformation rates along the arcs since there is no need to perform a search of phase ambiguities in the solution space. Once the parameters along the arcs are determined, parameters at the points can be obtained by spatial integration, which can also be performed under a least squares framework. The arcs and the points can be linked by a design matrix $\boldsymbol{U}$

$$\boldsymbol{L} = \boldsymbol{U}\,\boldsymbol{X}_{\mathbf{0}} \tag{4.31}$$

where $\boldsymbol{L}$ is the parameters at the arcs, and $\boldsymbol{X}_{\mathbf{0}}$ is the parameters at the points

$$\begin{aligned}
\boldsymbol{X}_{\mathbf{0}} &= \begin{bmatrix} \boldsymbol{x}_{\mathbf{1}} & \boldsymbol{x}_{\mathbf{2}} & \cdots & \boldsymbol{x}_{\boldsymbol{i-1}} & \boldsymbol{x}_{\boldsymbol{i}} & \boldsymbol{x}_{\boldsymbol{i+1}} & \cdots & \boldsymbol{x}_{\boldsymbol{H}} \end{bmatrix}^T \\
\boldsymbol{x}_{\boldsymbol{i}} &= \begin{bmatrix} h_i & \boldsymbol{V}_{\boldsymbol{i}} \end{bmatrix} \\
\boldsymbol{U} &= \begin{bmatrix} 1 & -1 & 0 & 0 & \cdots & 0 \\ 1 & 0 & -1 & 0 & \cdots & 0 \\ \vdots & & & & & \\ 0 & 0 & 1 & -1 & \cdots & 0 \\ \vdots & & & & & \\ 0 & 0 & 0 & \cdots & 1 & -1 \end{bmatrix}_{G\times H}
\end{aligned} \tag{4.32}$$

where G is the number of arcs and H is the number of points. $\boldsymbol{U}$ is built according to the records of the starting and the ending point for each arc during network construction. We set 1 for the starting point,-1 for the stopping point and 0 otherwise in the matrix $\boldsymbol{U}$. The rank of the design matrix $\boldsymbol{U}$ is always one less than the number of the TCPs. As a result, the system must be solved relative to a reference point at which the parameters are known. Let the ith point be the reference point with known parameters ($\boldsymbol{R}_i$), and its corresponding column in $\boldsymbol{U}$ is $\boldsymbol{S}_i$. By introducing $\boldsymbol{L}_L$ with $\boldsymbol{L}_L = \boldsymbol{L} - \boldsymbol{S}_i \boldsymbol{R}_i$, we obtain

$$\boldsymbol{L}_L = \boldsymbol{U}_U \boldsymbol{X} \tag{4.33}$$

where $\boldsymbol{U}_U$ is an updated design matrix in which the ith column has been removed and $\boldsymbol{X}$ is the parameter matrix for all the points except the reference point. The least squares solution is

$$\hat{\boldsymbol{X}} = \left(\boldsymbol{U}_U{}^T \boldsymbol{P} \boldsymbol{U}_U \right)^{-1} \boldsymbol{U}_U{}^T \boldsymbol{P} \boldsymbol{L}_L \tag{4.34}$$

where $\boldsymbol{P}$ is the weight matrix which can be determined according to the VC-matrix of arcs. It should be noted that when determining the VC-matrix of arcs, the correlation among arcs should be considered. For example given two adjacent arcs, (l, m, l', m') and (l', m', l'', m'') the VC-matrix of these two arcs has the form as

$$D \begin{bmatrix} \Delta \phi_{l,m,l',m'} \\ \Delta \phi_{l',m',l'',m''} \end{bmatrix} = \begin{bmatrix} Q^{arc}_{l,m,l',m'} & Q_{l,m,l',m',l',m',l'',m''i} \\ Q_{l,m,l',m',l',m',l'',m''i} & Q^{arc}_{l',m',l'',m''} \end{bmatrix} \tag{4.35}$$

When the noise level of the TCPs is available, the VC-matrix of arcs can be conveniently generated based on the network construction matrix (U)according to the variance prorogation law. If more than one reference points (say N , $N \geqslant 2$,) are available, the parameters can be solved by adding constraints

$$\underset{\boldsymbol{N-1,hH,1}}{\boldsymbol{C} \quad \boldsymbol{X}} + \underset{N-1,1}{\boldsymbol{M}_x} = 0 \tag{4.36}$$

where $\boldsymbol{C}$ is a design matrix indicating the positions of the $N-1$ reference points; and $\boldsymbol{M}_x$ are the known parameters at the $N-1$ reference points. The solution is

$$\hat{\boldsymbol{X}}=\left(\boldsymbol{N}_{BB}^{-1}-\boldsymbol{N}_{BB}^{-1}\boldsymbol{C}^T\boldsymbol{N}_{CC}^{-1}\boldsymbol{C}\boldsymbol{N}_{BB}^{-1}\right)\boldsymbol{Z}-\boldsymbol{N}_{BB}^{-1}\boldsymbol{C}^T\boldsymbol{N}_{CC}^{-1}\boldsymbol{M}_x \tag{4.37}$$

where $\boldsymbol{N}_{BB}=\boldsymbol{U}_U{}^T\boldsymbol{P}\boldsymbol{U}_U$, $\boldsymbol{Z}=\boldsymbol{U}_U{}^T\boldsymbol{P}\boldsymbol{L}_L$, and $\boldsymbol{N}_{CC}=\boldsymbol{C}\boldsymbol{N}_{BB}^{-1}\boldsymbol{C}^T$.

4.4 Validation with simulated data

A dataset consisting of 21 simulated C-band images are used to validate the proposed approach. The advantage of using simulated data is that the estimated parameters can be compared with their true values that are often not known in case of real datasets [Kampes, 2006]. During the simulation, we adopt the similar noise and atmospheric parameters used by Kamples (2006) for the test of the STUN method. Namely, the mean of the random phase noise is set to 15° with a standard deviation of 5° for all the SLC images and within each SLC image the noise follows the norm distribution. The atmospheric phase is simulated using fractal surfaces with a dimension of 2.67. More details about the simulation can be found in [Kampes, 2006] and [Hanssen, 2001].

An example of the simulated noise and atmospheric signal is shown in Fig. 4.3. 44 interferograms with perpendicular and temporal baselines shorter than 150 m and two years, respectively, are produced from the 21 images (Fig. 4.4). 1,500 TCPs are selected within an area of 5×5 km^2. The simulated DEM errors at the TCP that follow a uniform distribution between -10m and 10m are shown in Fig. 4.5(a). Both linear and non-linear deformation models are simulated to test the robustness of the proposed method.

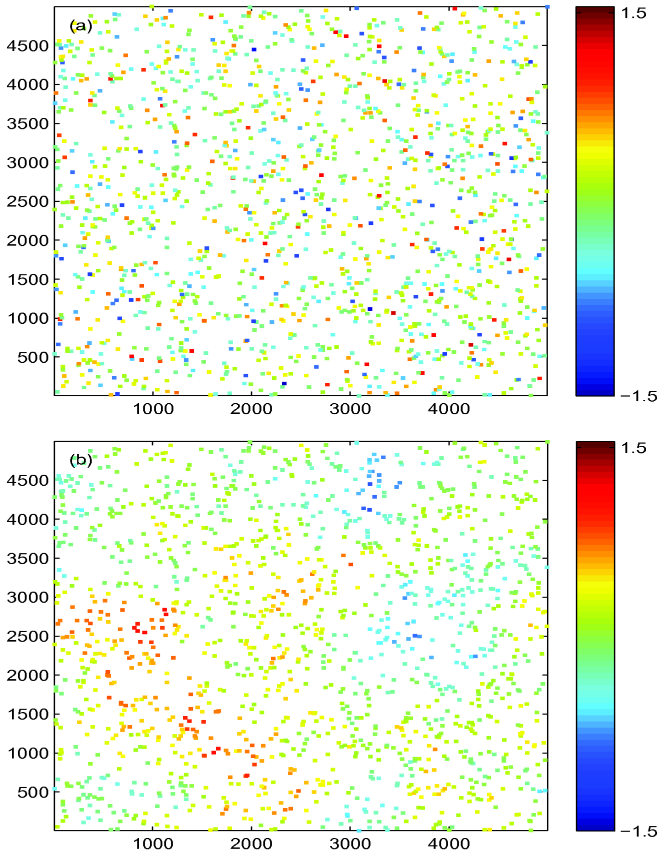

Fig. 4.3: Examples of simulated signals. (a) Simulated noise in an SLC image, and (b) simulated atmospheric artifact. The unit is rad.

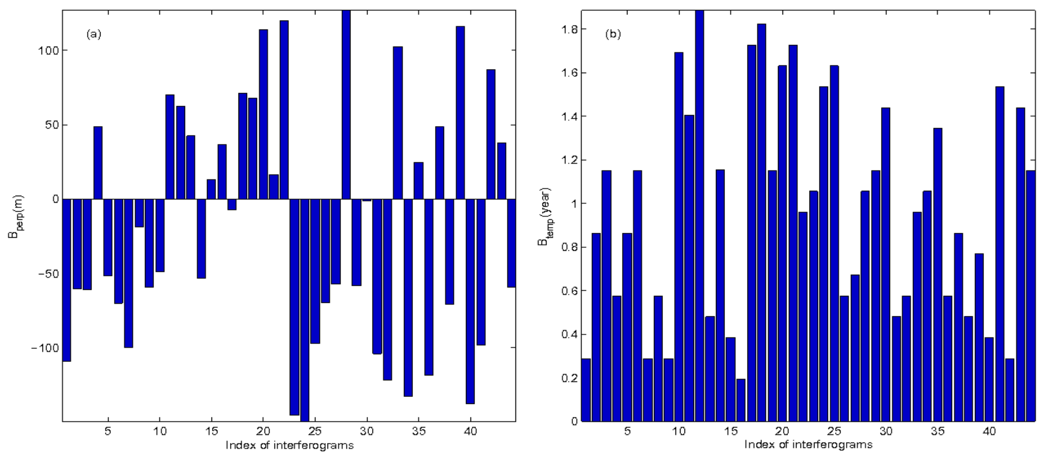

Fig. 4.4: (a) Perpendicular baselines and (b) temporal baselines of the 44 simulated interferograms

4.4.1 Estimation of linear deformation signal

Linear deformation rates with a maximum magnitude of 72 mm/year whose spatial pattern is shown in Fig.4.5 (b) are first simulated to test the performance of the proposed method. The phase contributions from the DEM errors, deformation, noise, atmospheric artifacts and orbital inaccuracy are shown in Fig. 4.6. For testing purpose, we first connect the 1500 TCP by a global Delaunay triangulation network (Fig. 4.1(a)). After removing the arcs with phase ambiguities by the outlier detector, it is found that the network constructed by the remaining arcs is too sparse to estimate the parameters at all the points. We then adopt the local triangulation strategy as described in Section 4.2.1 to generate a network of 20091 arcs (Fig. 4.1(c)). The longest arc has a distance of 1454 m.

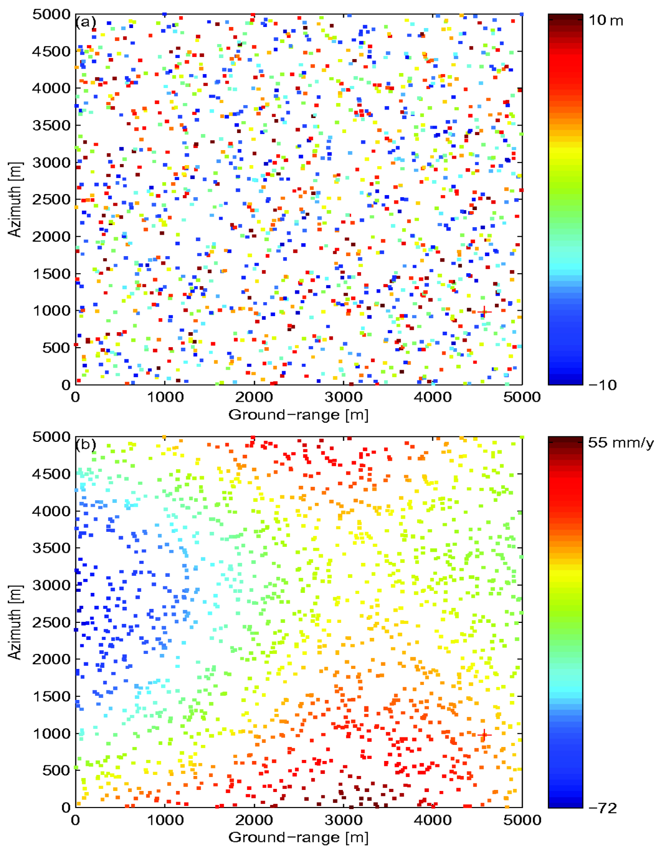

Fig. 4.5: (a) Simulated DEM errors, and (b) simulated linear deformation rates. The red cross indicates the position of the reference point

A histogram of the absolute residuals from the first least squares estimation is shown in Fig. 4.7(a). 9711 arcs are detected as outliers by applying the outlier detector and removed from the network. The actual number of arcs with phase ambiguities is 9535, all of which have been successfully identified. This also means that 176 arcs have been misidentified. After removing the detected arcs, the least squares estimator is performed again. Fig. 4.7(b) shows the updated histogram of the residuals at the remaining arcs.

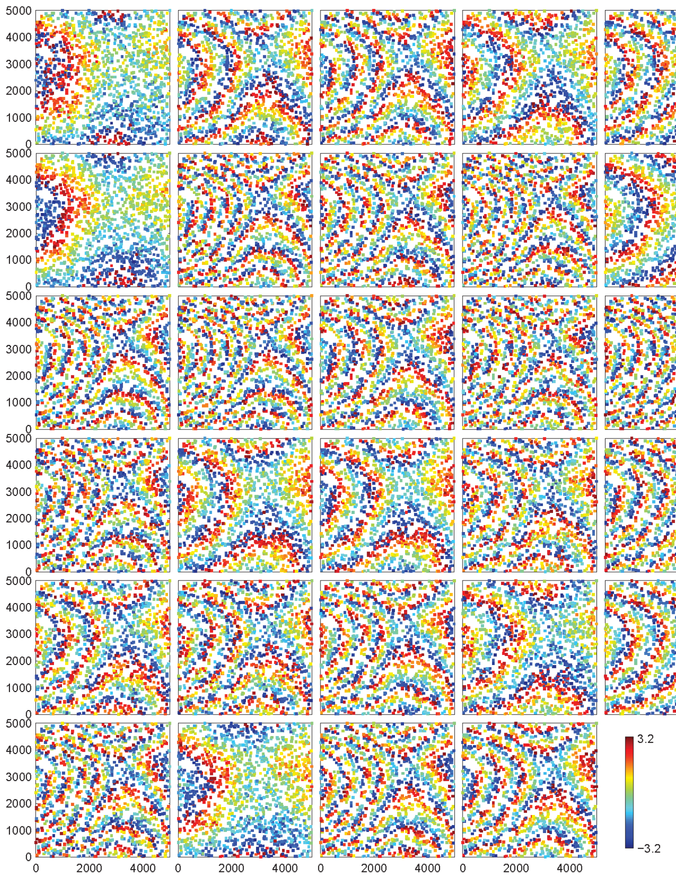

Fig. 4.6:The simulated wrapped phase at coherent points in the 44 interferograms. Phase values contain components corresponding to DEM errors, deformation, atmospheric artifacts and random noise. The unit is rad

Using the a priori VC matrix for the double-difference phase observations, the VC matrix of the estimated parameters (the differential DEM error and the differential deformation rate) is (see Eq. (4.14))

$$Q_{\Delta h,\Delta v}=\begin{bmatrix} 2.7 & -0.09 \\ -0.09 & 0.02 \end{bmatrix} \tag{4.38}$$

Here, the DEM error (first parameter) is in meters and the deformation rate (the second parameter) is in millimeters/year. It is seen therefore from Eq. (4.33) that the standard deviations of the estimated parameters are 1.6 m and 0.14 mm/year respectively.

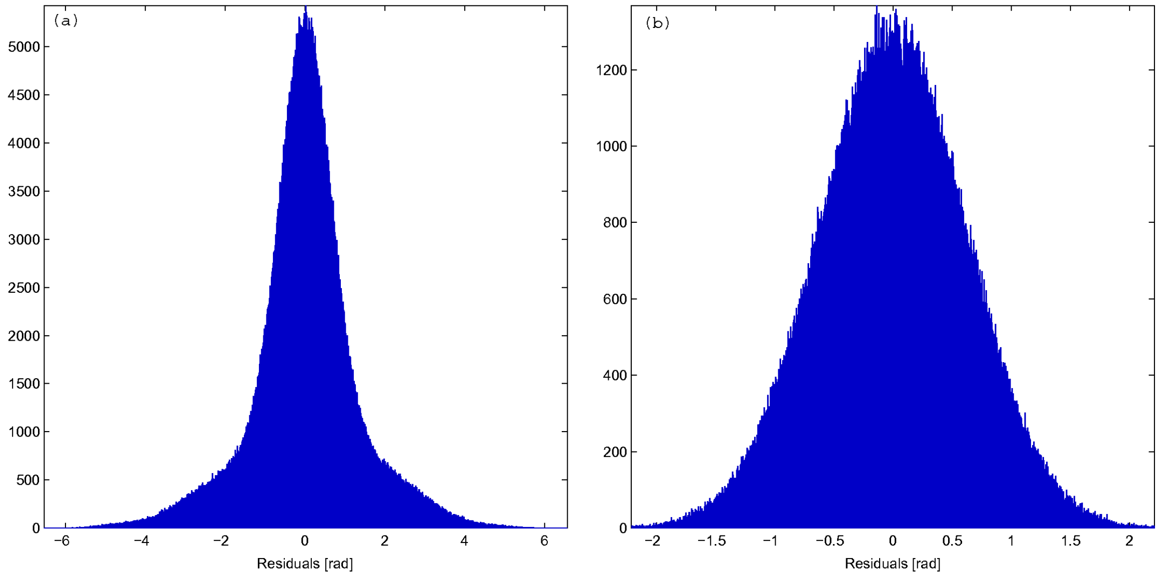

Fig. 4.7: (a) Histogram of least squares residuals for all observations. (b) Histogram of least squares residuals after removing arcs with ambiguities

Table 1. Statistics of errors in the estimated parameters

	Min	Max	Mean	Std
DEM error (m)	-8.1	2.4	-2.6	1.72(1.64)
Linear defo. rate (mm/y)	-0.45	0.41	-0.01	0.164(0.137)

Once the double difference parameters at the arcs are determined, the parameters at the points can be obtained by spatial integration (when one reference point is assumed). Fig. 4.8 shows the errors in the estimated DEM and the deformation rates at the TCP, i.e., difference between the estimated and the true values. A statistics of the errors is given in Table 4.1. It can be seen from the results that the estimated DEM accuracy is not as high as that typically estimated with PSInSAR. This is mainly due to the fact that only interferograms with short baselines are used in the solution.

4.4.2 Estimation of non-linear deformation signal

Non-linear deformation signal is simulated to assess the performance of the proposed method in areas experiencing complex deformation. The model for ground deformation in the LOS direction takes the following form

$$d(T) = -15\mathrm{T} + 3\mathrm{T}^2 + 0.2\mathrm{T}^3 \tag{4.39}$$

The coefficients to be estimated at the TCP are shown in Fig. 4.9 (a)-(c). By updating the design matrix, i.e., in Eq. (4.7), the least squares model can be used directly for non-linear parameter estimation. The errors in the estimated coefficients (compared with the simulated input) are shown in Fig.4.8 (e)-(f). A statistics of the errors at the TCP is given in Table 4.2. It is seen from the results that the proposed method works well with the non-linear deformation signal although the estimation accuracy is not as high as in the case of the linear signals. This is mainly due to the limited number of observations available, i.e., interferograms. In order to get more accurate estimation of complex deformation signals, more interferograms should be used.

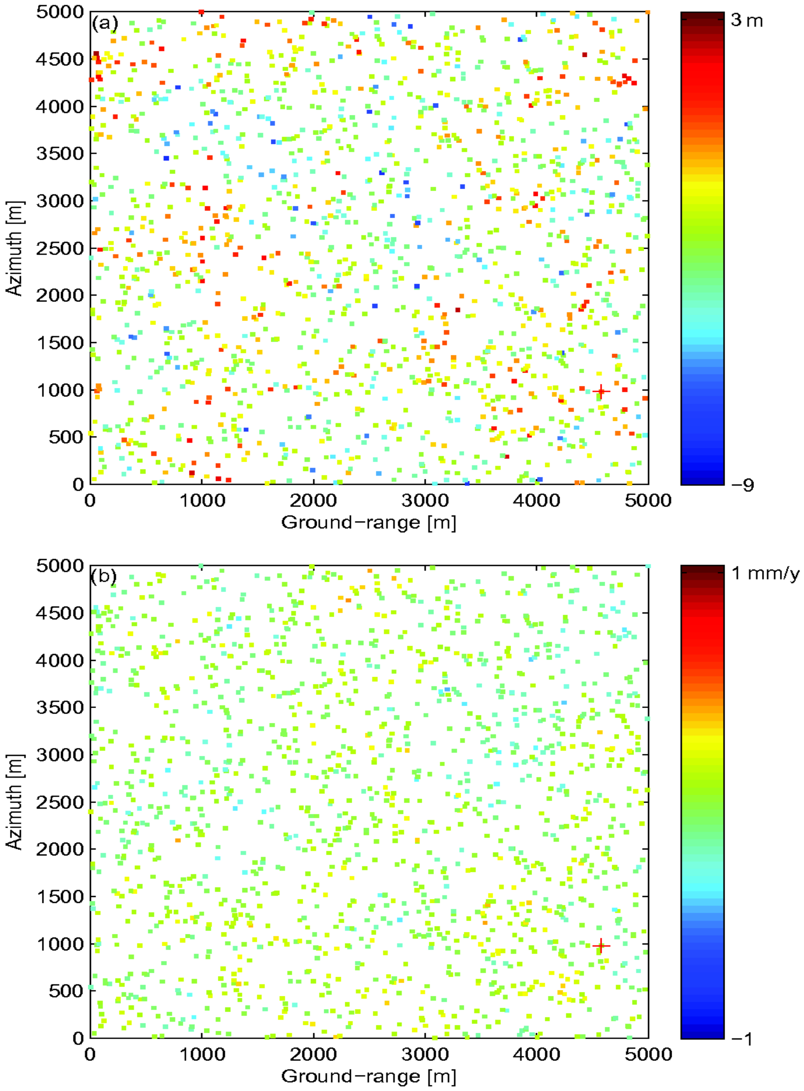

Fig. 4.8: (a) Errors in the estimated DEM at the TCP; (b) Errors in the estimated deformation rate at the TCP

Table 4.2. Statistics of errors in the estimated coefficients

Coefficient	Min	Max	Mean	Std
Linear term (mm/y)	-6.58	2.63	-1.94	1.43(1.25)
Quadratic term (mm^2/y^2	-0.91	1.46	0.35	0.35(0.31)
Cubic term (mm3/y^3)	-0.09	0.07	-0.02	0.024(0.021)

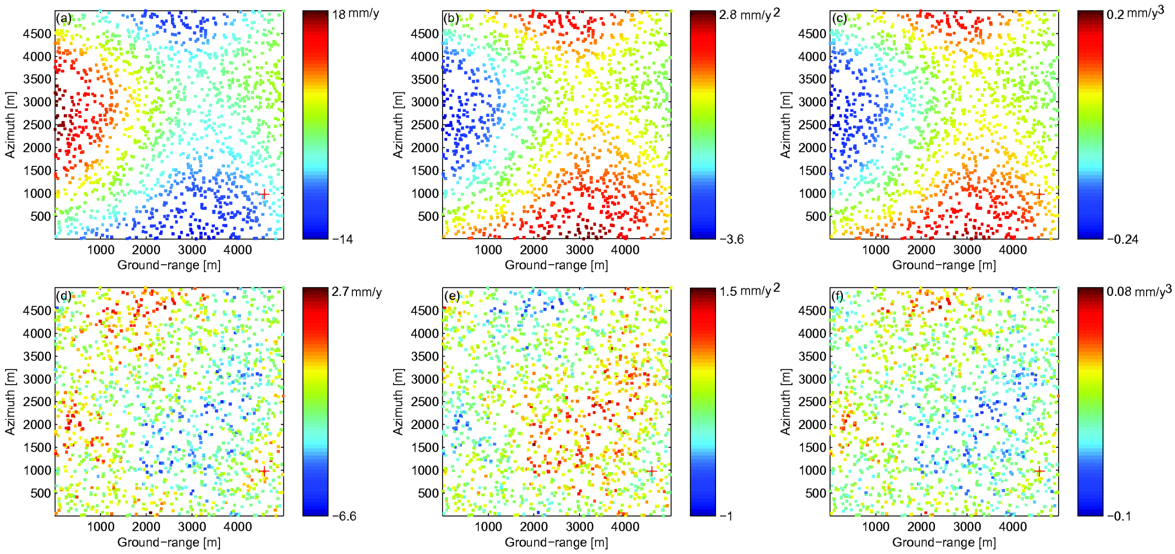

Fig. 4.9: (a)-(c): Coefficients to be estimated at each TCP, linear term, quadratic term and cubic term respectively. (d)-(f): Corresponding errors in the estimated coefficients

4.4.3 Comparison with unweighted LS solution

A least squares solution is derived without using the weight matrix to assess the impact of applying the weight matrix. It is found from the results obtained that the standard deviation of the estimated deformation rates is degraded from 0.16 mm/year to 0.41 mm/year (Table 4.3) when no weight matrix is used. The results also become worse for the case of non-linear deformations. This indicates that a proper weighting scheme is important and should be used for modeling multiple SAR acquisitions.

Table 4.3. Comparison between errors in estimated deformation rates using weighted and non weighted models

		Min	Max	Mean	Std
Linear defo. rate	With weight	-0.45	-0.41	-0.01	0.16
(mm/y)	No weight	-1.14	1.49	0.04	0.41

4.4.4 VCE validation

In the previous Section the LS estimator is performed with a priori variance matrix of the SLC images. Although the quality of the estimated parameters is good, their precision can not be reliably evaluated with no presence of a proper stochastic model. The values in Eq. (4.33) and in the parentheses of Table 4.1 and Table 4.2 are actually meaningless if the noise level of SLC acquistions is not adequately known. We verified here the VCE algorithm with simulated data sets having larger and more fluctuated noises for the multi-master MT-InSAR system.

As stated in Section 4.3.4, the starting point of VCE is the LS residuals of the isolated arcs (see Fig. 4.10). The variance components of SLC images are estimated iteratively with an initial weight matrix where the noise level of each SLC image is set equally to 12°. The results are shown in Fig. 4.11. In general the estimated variance components are consistent with the simulated noise, implying that the proposed VCE algorithm is valid. There are however noticeable differences on several images which are caused by the existence of the atmospheric artifacts and the assumption that the two points at the ends of the arc share the same noise varaince. The VC-matrix of the estimated parameters in this case is obtained by error propagation using the estimated variance factors of the stochastic model.

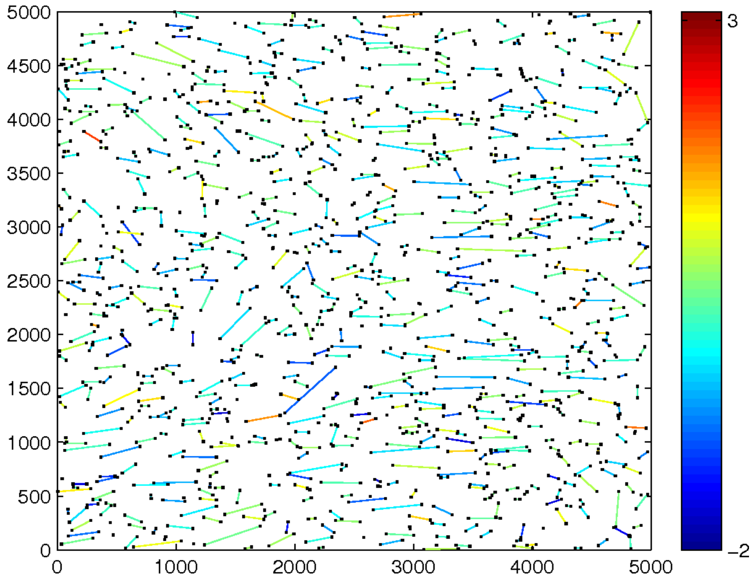

Fig. 4.10: An example of LS residuals at arcs for VCE. There are a total of 701 arcs for the estimation.

$$Q_{\Delta h,\Delta v} = \begin{bmatrix} 4.5650 & -0.1713 \\ -0.1713 & 0.0347 \end{bmatrix} \tag{4.40}$$

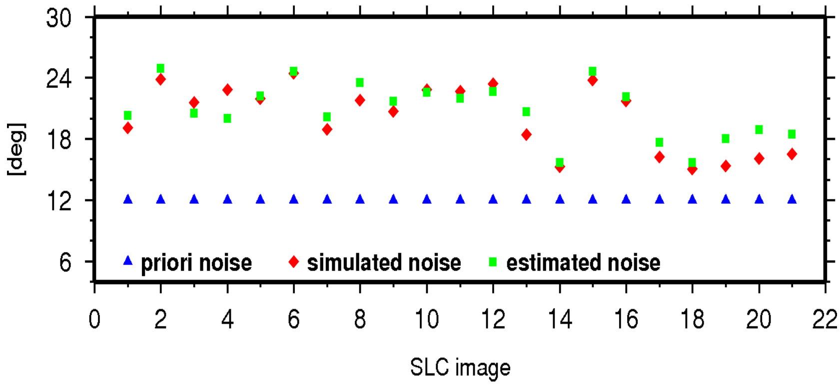

Fig. 4.11: Estimated variance components of SLC acquisitions with the presence of atmospheric signals.

A comparison of deformation rates with a priori variance components and estimated variance components is shown in Table 4.4.

Table 4.4. deformation rate determined with a priori VC and an estimated VC

		Min	Max	Mean	Std
Linear defo. rate (mm/y)	With a priori VC	-0.88	0.71	0.07	0.2 (0.137)
	With an estimated VC	-0.75	0.68	0.03	0.17 (0.186)

It is clear from the results that the precision of the parameters estimated in this case is not improved greatly after the implementation of the VCE. However the VC-matrix of the estimated parameters is more realistic which can be used to evaluate the precision of the results.

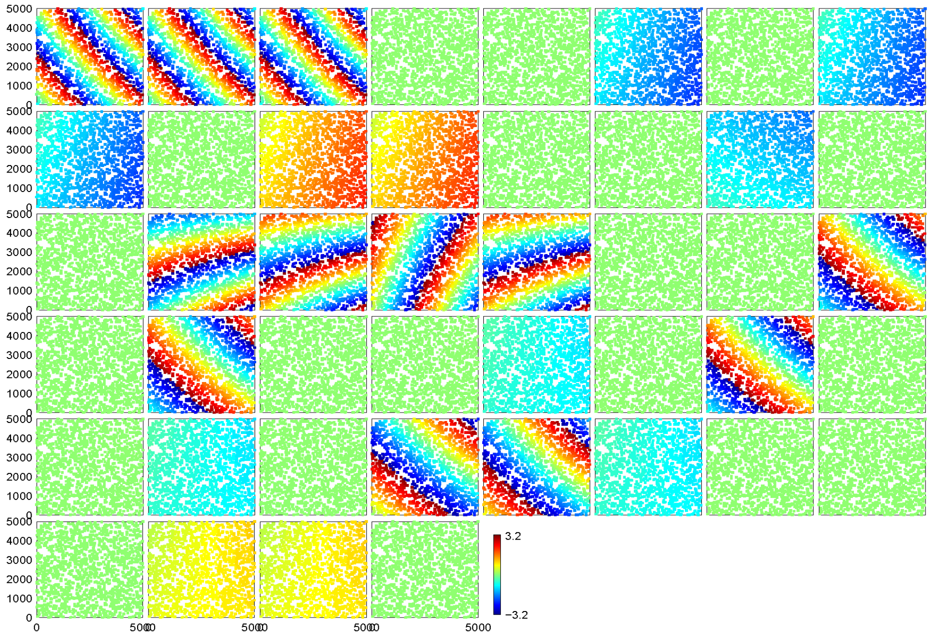

Fig. 4.12: Wrapped orbital errors used in the simulation test (unit: rad).

4.4.5 Orbital error refinement

The satellite orbital errors can be modeled by a low-order polynomial in spatial domain and usually taken as random noise (at arcs) in temporal domain. Current methods for orbital error correction are usually performed interferogram by interferogram, which obviously will reduce the processing efficiency for a large set of data. More importantly, single interferogram based methods can be effected by the atmospheric artifacts. Our simulation test has indicated that the stacking of interferograms in temporal domain will not change the spatial feature of the orbit errors. In other words the stacked orbital errors can still be modeled by a best-fitting phase ramp. Therefore, it is possible to remove the orbit error by the ground truth (e.g., GPS data) after the application of the proposed LS estimator. Orbital errors shown Fig.4.12 have been added into the simulated data to test the performance of this strategy.

After removing the arcs with phase ambiguities, the deformation parameters at arcs are estimated (see Fig.4.13). An example of the LS residuals at the arcs is shown in Fig. 4.14, which indicates that the differential orbital error at arcs does not contribute much to the residuals due to its feature of high spatial correlation.

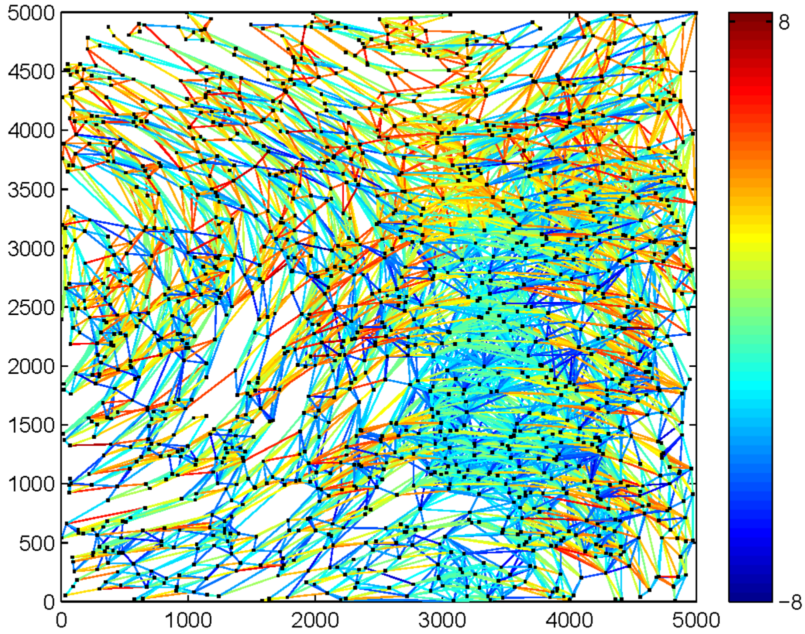

Fig. 4.13: Estimated rate differences at arcs (unit:mm/y)

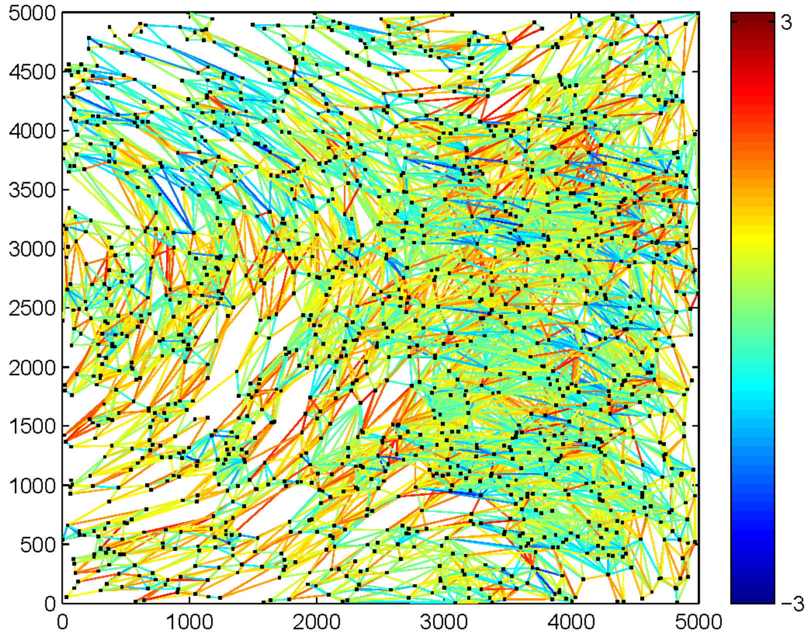

Fig. 4.14: LS residual at arcs of the first interferogram (unit: rad)

The estimated deformation rates of TCPs are shown in Fig. 4.15. Assuming that ground measurements are available over a study area or it is known that some parts of the area are stable, we can select several points to model a best-fit polynomial for the deformation rate map. We employ in this simulation 8 ground points to fit a low order polynomial as follows

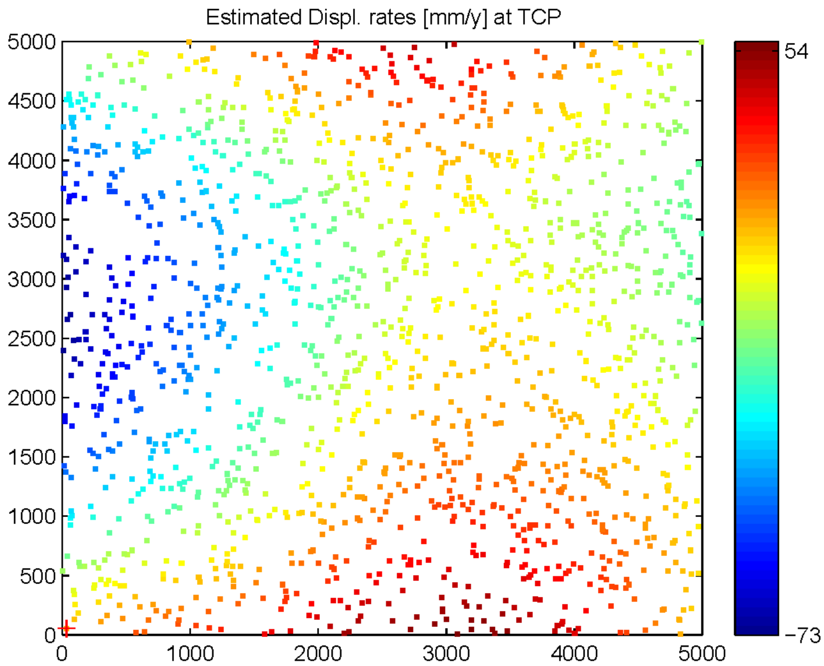

Fig. 4.15: Estimated deformation rates from data with orbital errors

$$V_{orb} = ax + by + cxy + d \tag{4.41}$$

Where V_{orb} is the velocity difference between the estimated and the ground measurement, x and y are the pixel location of the given ground point. Again under the framework of least squares, the coefficiencies of the linear function (i.e., a, b, c, d) can be estimated, resulting in a rate map contributed by the orbital error (Fig. 4.16).

Once the velocity map caused by orbital errors is determined, the final estimates can be achieved by subtracting this component directly from the results shown in Fig 4.15. The residuals compared with the “true” deformation rates are presented in Fig. 4.17, indicating that the proposed approach is adequate for eliminating the orbital effects on the deformation parameter estimation and can be performed efficiently. Since the effect of the differential atmospheric signals at arcs that behave randomly in the temporal domain can be successfully suspended during the LS estimation, their contributions to the estimated mean rates are rather limited. Under this circumstance, the orbital error can be precisely modeled by a low order polynomial, leading to a better estimation of the parameters.

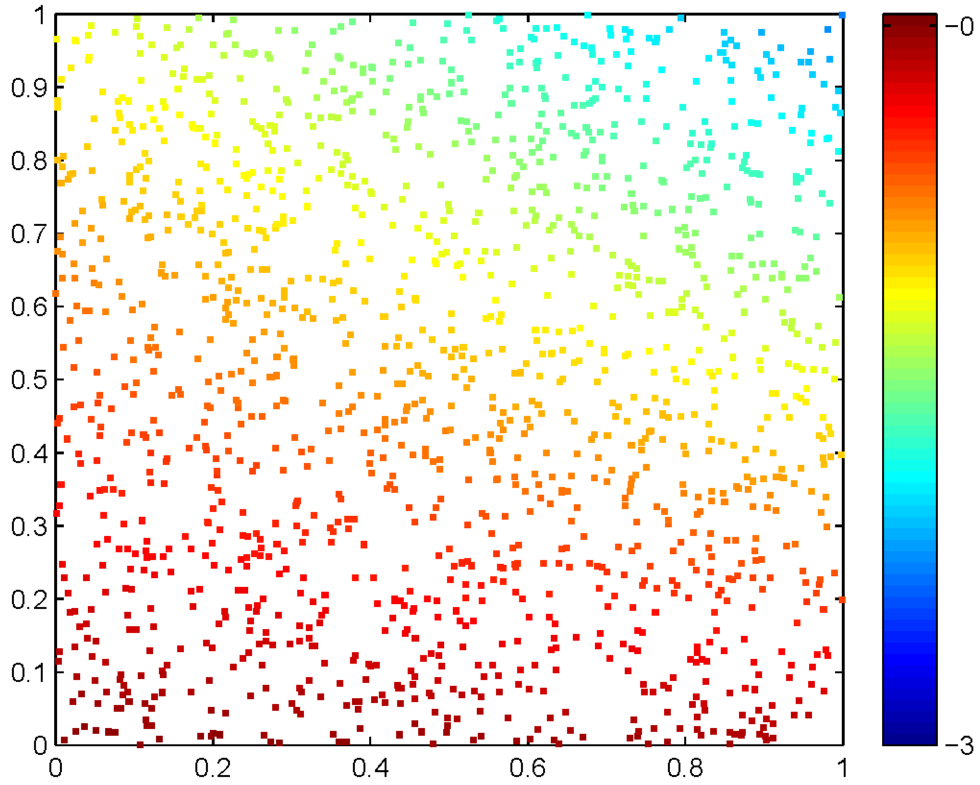

Fig. 4.16: Velocity map caused by orbital errors (unit: mm/y)

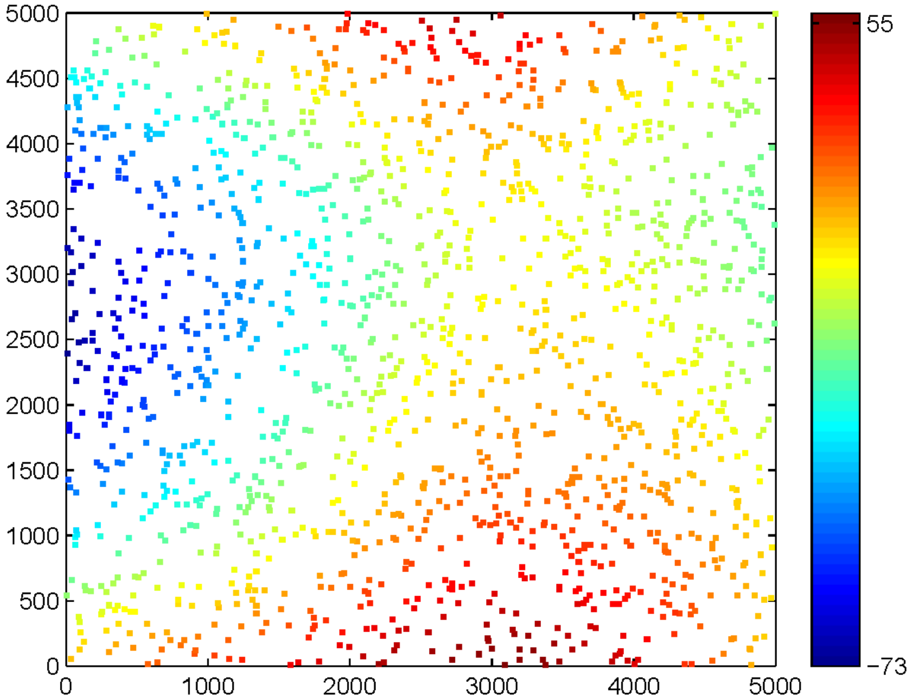

Fig. 4.17: Final errors of the estimated deformation rates compared with their true values (unit: mm/y)

4.5 Conclusions

As a core component of the TCPInSAR technique, a parameter estimation approach with no need of estimating phase ambiguities is presented in this chapter. To increase the density of arcs without phase ambiguities we triangulate the TCP on distributed and overlapped patches over a study area. To remove arcs occasionally having phase ambiguities, an phase ambiguity detector based on the LS residuals is designed. To better consider the quality of the interferograms and to evaluate the precision of the estimated parameters, a VCE approach is proposed for multi-master MT-InSAR system. To deal with SAR data acquired from poorly determined orbits, a simple and reliable method for eliminating orbital errors is suggested. All the methods have been validated by the simulated data where the estimated parameters are accurate in a qualitative sense. It should be noted that although during the simulated test only the modeled deformation (e.g. linear or polynomial) is used, the proposed method also can be potentially used for estimating the full-resolution deformation time series as long as the atmospheric component in the LS residuals have been filtered properly, which is in fact commonly performed in all current InSAR time series estimators. In next Chapter the deformation time series in Los Angeles basin will be presented.

5 Long Term Deformation in Los Angeles Basin from TCPInSAR

In this Chapter we will apply the proposed TCPInSAR method to the Los Angeles basin in southern California where several faults, such as Newport-Inglewood fault, are still structurally active and are believed capable of generating damaging earthquakes. The analysis is based on 55 interferograms from 32 ERS-1/2 images acquired during Oct. 1995 to Dec. 2000. To evaluate the performance of TCPInSAR on a small set of observations, a test with half of interferometric pairs is also performed.

5.1 Introduction

The Los Angeles basin, a polyphase Neogene basin within the San Andreas transform system, has been developed as a result of regional crustal extension associated with the opening of the California Borderlands and the rotation of the Transverse Ranges (Fig.5.1) [*Hauksson*, 1990; *Shaw and Shearer*, 1999]. Since the early Pliocene, the basin has been deformed by numerous decoupled strike-slip and thrust motions within several active fault zones that are capable of generating moderate to large earthquakes. Studies of historic earthquakes including the 1933 Long Beach (Mw=6.4), 1971 San Fernando (Mw=6.7), 1987 Whittier Narrows (Mw=6.0), and 1994 Northridge (Mw=6.7) (Fig.1) revealed that both surface and blind thrust faults represent a significant threat to the Los Angeles metropolitan area (Hauksson, 1987; Hauksson and Jones, 1989; Davis et al., 1989; Hauksson et al, 1995; Shaw and Shearer, 1999; Bawden et al., 2001; Mellors et al., 2004). Hence, understanding the seismotectonic motions in the Los Angeles basin is important for assessing and mitigating earthquake hazards.

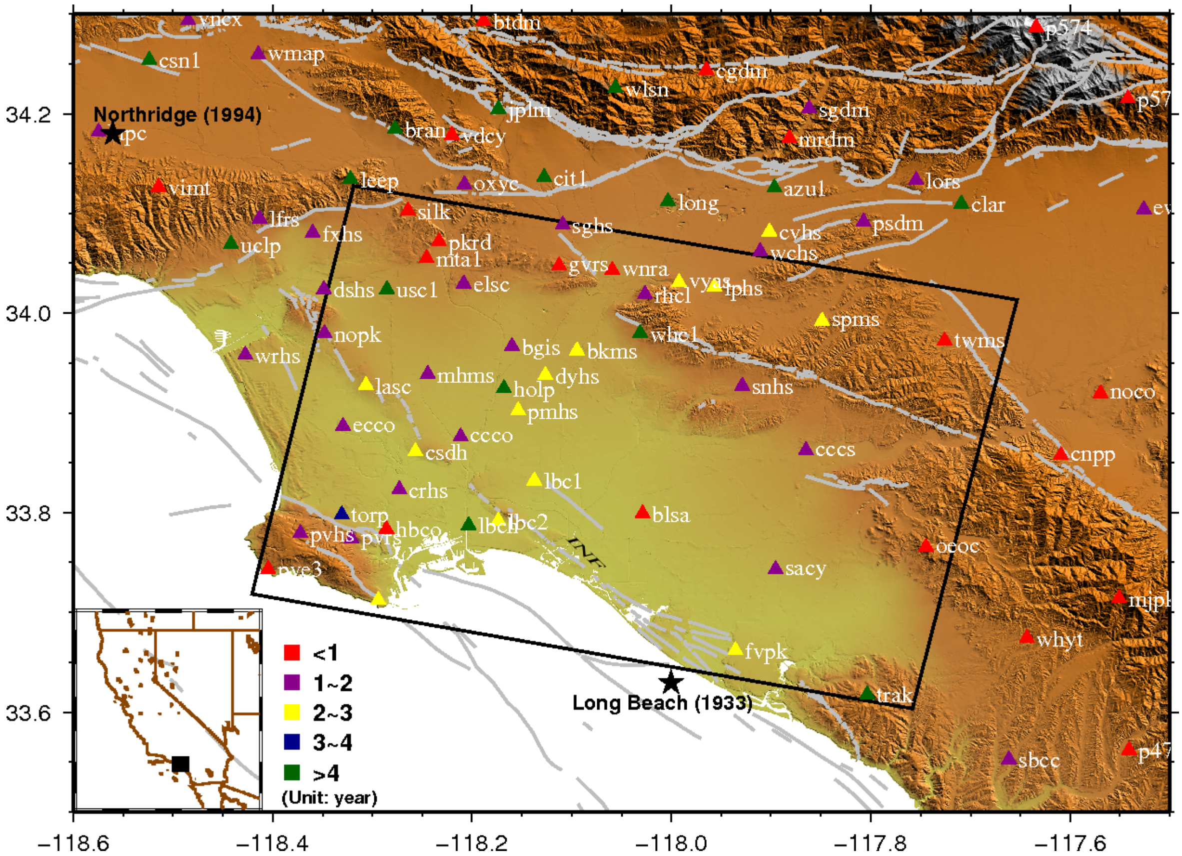

Fig. 5.1: Shaded relief map of Los Angeles basin. Faults appear as gray lines (data source: (U. S. Geological Survey 2010)) . The black box outlines the studied area covered by ERS-1/2 SAR data (track 170,frame 2925). The triangles indicate the location of GPS sites and the corespoinding colors show the overlap time with the SAR data (unit: year). The black stars represent the moderate-size earthquakes occurred in the basin.

The TCPInSAR method is applied to study the Los Angeles basin where moderate tectonic movements and minimum image decorrelation make it very suitable for testing novel InSAR techniques [*Bawden et al.*, 2001; *Watson et al.*, 2002 ; *Lanari et al.*, 2004]. The data processing procedure involved is discussed in this Chapter. Technical issues are addressed to deal with the problem of phase jumps at interferometric fringe edges as well as the effect of long and short arcs on estimating the spatially complex deformation. Moreover the estimation of deformation time series without a priori model is also performed. To evaluate the performance of InSAR modeling with smaller datasets, we have applied the TCPInSAR approach with half of the original interferometric observations. The estimated line-of-sight (LOS) linear deformation rate is consistent with the one estimated from the full dataset. Quantitative comparisons have confirmed the validity of the results achieved from the TCPInSAR method, indicating the TCPInSAR has the potential to provide ground motion data for fault stress inversion and seismic hazard evaluation with significantly reduced computational complexity even in areas without abundant SAR images.

5.2 TCPInSAR analysis

5.2.1 Data selection

We wish to reduce the phase contribution related to topography residuals, atmospheric artifacts as much as possible so that phase differences at a large number of arcs in a limited time span will not have phase ambiguities. To this end, we will only select image pairs with perpendicular spatial baseline less than 300m and temporal baseline less than 2.5yr (Fig. 5.2). In addition, the Doppler centriod frequency differences in the selected pairs are limited to 300Hz allowing us to model the phase difference between two neighboring points caused by the azimuth sub-pixel position of the two points as a random component in a large set of interferograms. We further remove the interferograms that are obviously affected by the rather localized bubble-like atmospheric errors. Finally we select 55 interferograms from 32 ERS-1/2 images (track 170, frame 2925) as the basis of TCPInSAR processing.

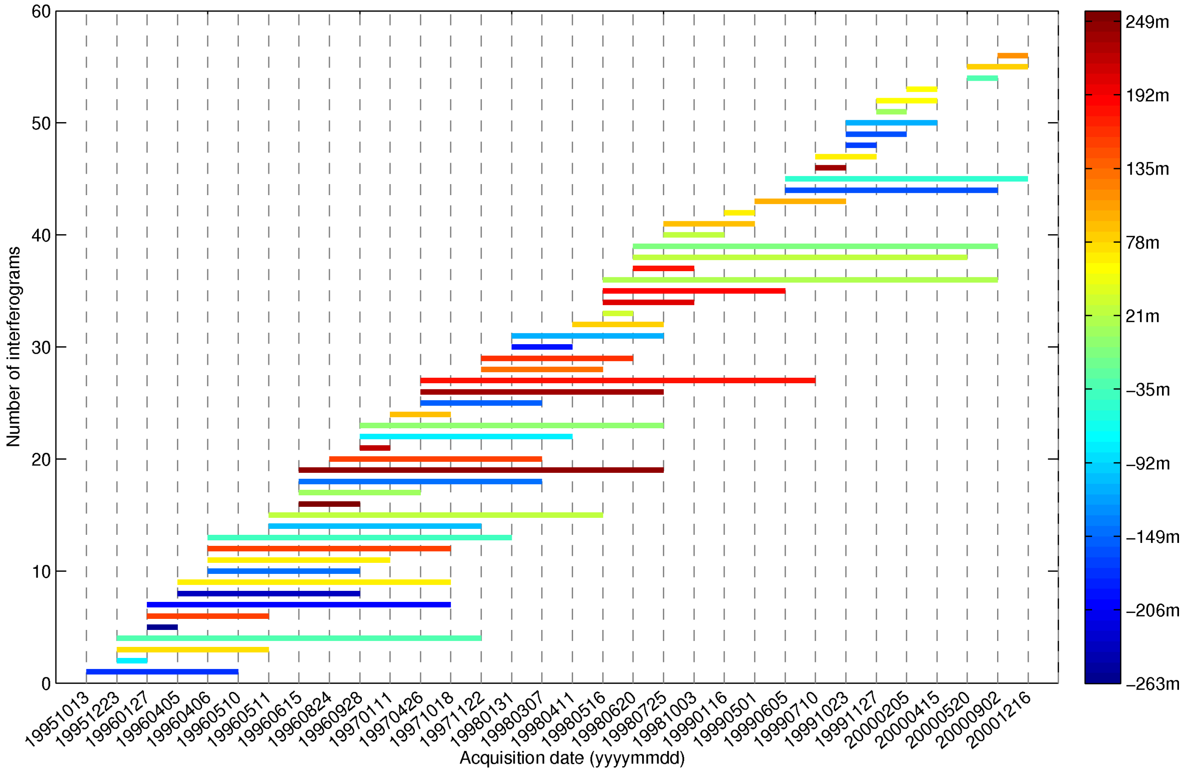

Fig. 5.2: Perpendicular baselines and temporal intervals of the selected InSAR image pairs.

5.2.2 TCP identification and coregistration

As discussed previously, temporarily coherent points (TCPs) are points in the interferograms that maintain coherent during one or several intervals of SAR acquisitions. The detailed description of the method for the identification of TCPs can be found in Chapter 2. Here we propose an improved processing strategy which can accelerate the TCP selection significantly. Using the master image, we first identify the points that can keep almost the same backscattering intensity when processed with different looks with fractional azimuth and range bandwidth as the TCP candidates. Second, the points that have been identified in the last step are considered as the TCP candidates and are further evaluated by changing the size of the patches and oversampling factor in estimating the image cross-correlation. For the sake of simplicity, a fixed oversampling factor can be used. A set of offsets of a given TCP candidate can then be obtained. The TCP candidates whose standard offset errors are less than 0.1 pixels are then selected. Third, a high-order polynomial is used to fit the offsets of TCP candidates and the final TCPs are selected by discarding the pixels whose offsets do not well fit the polynomial.

The precise offsets at TCPs are actually the by-product of TCP identification. If we coregister the slave images based on the polynomial determined from TCP offsets, the coregistration quality can be improved compared with the conventional coregistration method that uses offsets estimated from evenly distributed windows over the whole image. Especially in areas where the TCPs are surrounded by distributed scatterers, like the airport reclaimed from the sea (Zhang, et al., 2011a) and long cross-sea bridges, the improvement of interferometric coherence resulted from TCP coregistration procedure is apparent. Over Los Angeles basin, an average improvement of 0.05 with a standard deviation of 0.04 in interferometric coherence has been gained from TCP coregistration. It should be noted that since a TCP is selected based on image pairs, it can represent two types of point. If it keeps coherent in all image pairs, it can be called a persistently coherent point, while if it only keeps coherent in a subset of image pairs, it is a partially coherent point (Biggs et al., 2007, 2009). In this work we only use the TCPs that are persistently coherent during the whole time span in order to retrieve the full resolution deformation time series. The application of TCPInSAR on changing landscapes where both persistently and partially coherent points are present can be found in (Zhang et al., 2011c).

5.2.3 TCP network and phase jump

Phase differences at arcs constructed from two neighboring pixels are the basic observations for the least squares estimator described in the previous Chapter. In order to ensure that TCP are connected extensively we construct the network by local Delaunay triangulation that places small regular patches over the image and connects the TCPs in each patch if the number of the

TCPs in the patch is larger than 3. A factor should be addressed here is the length of arcs which is vital to reduce the atmospheric artifact and model the relative motion at arcs especially in the areas where the deformation pattern is spatially complex. GPS observations and hydrological study in the area suggested that the deformation pattern in Los Angeles basin is rather complex which includes the tectonic motion as well as the variations in the elevation of the water table[*Argus*, 2005]. The identified coherent points in this study area are abundant and can be connected extensively with short arcs. It has been found that the sensitivity of phase difference to seasonal fluctuations is less at shorter arcs than longer arcs (Fig.5.3). Using this procedure we have identified 201,778 TCPs and constructed 1,176,922 arcs of less than 500m for this study.

When determining the phase difference at the arcs in the network, we should pay attention to the so-called "phase jumps" at the interferometric fringe edges, which are caused by the fact that the observed interferometric phase is limited to the range of $\left(-\pi\,\pi\right]$. Considering two nearby points those phase values of and are near the interferometric fringe edge as indicated in Eq. (5.1), the direct phase difference between these two points should be $-2\pi+\Delta_1+\Delta_2$, which falls outside of $\left(-\pi\,\pi\right]$. Therefore a wrapping operation should be performed to eliminate this artificial error.

$$
\begin{aligned}
\phi_{1,true} &= -\pi+\Delta_1 \\
\phi_{2,true} &= -\pi-\Delta_2 \\
\phi_{1,true}-\phi_{2,true} &= \Delta_1+\Delta_2 \in \left(-\pi\,\pi\right] \\
\phi_{1,observed} &= \phi_{1,true} \\
\phi_{2,observed} &= \pi-\Delta_2 \\
\phi_{1,observed}-\phi_{2,observed} &= -2\pi+\Delta_1+\Delta_2 \\
wrap\left(\phi_{1,observed}-\phi_{2,observed}\right) &= \phi_{1,true}-\phi_{2,true}=\Delta_1+\Delta_2
\end{aligned}
\tag{5.1}
$$

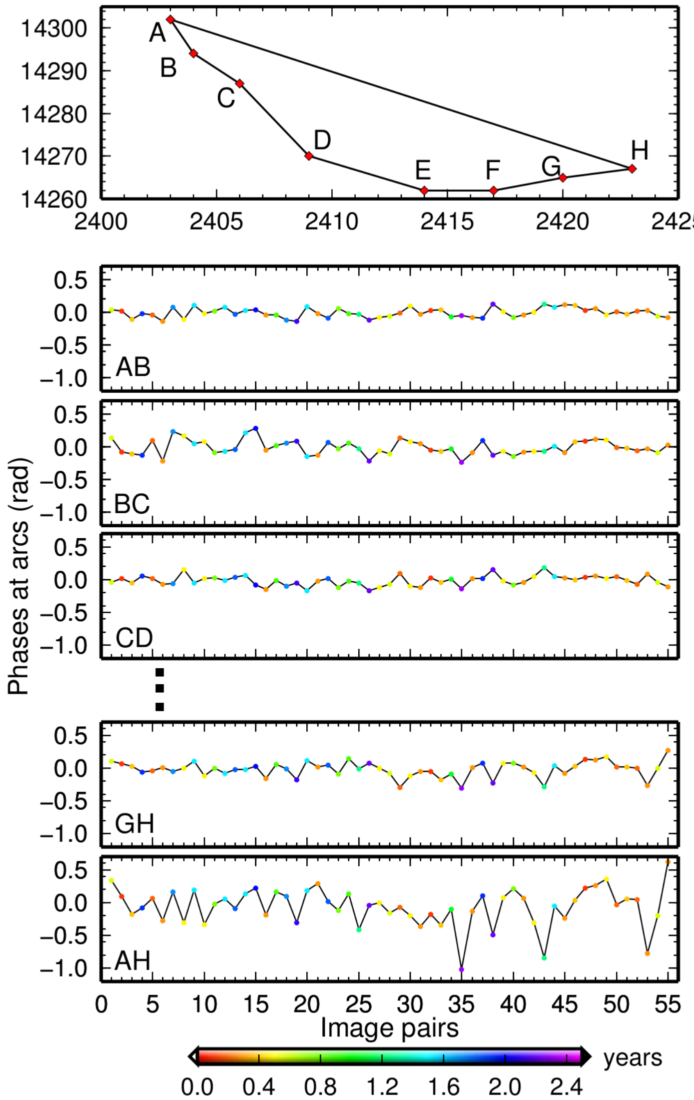

Fig. 5.3:The top figure shows the spatial location of TCPs. The rest figures show the phase differences at short arcs (A-B-C-D-E-F-G) and a long arc (AH) in 55 selected interferograms.

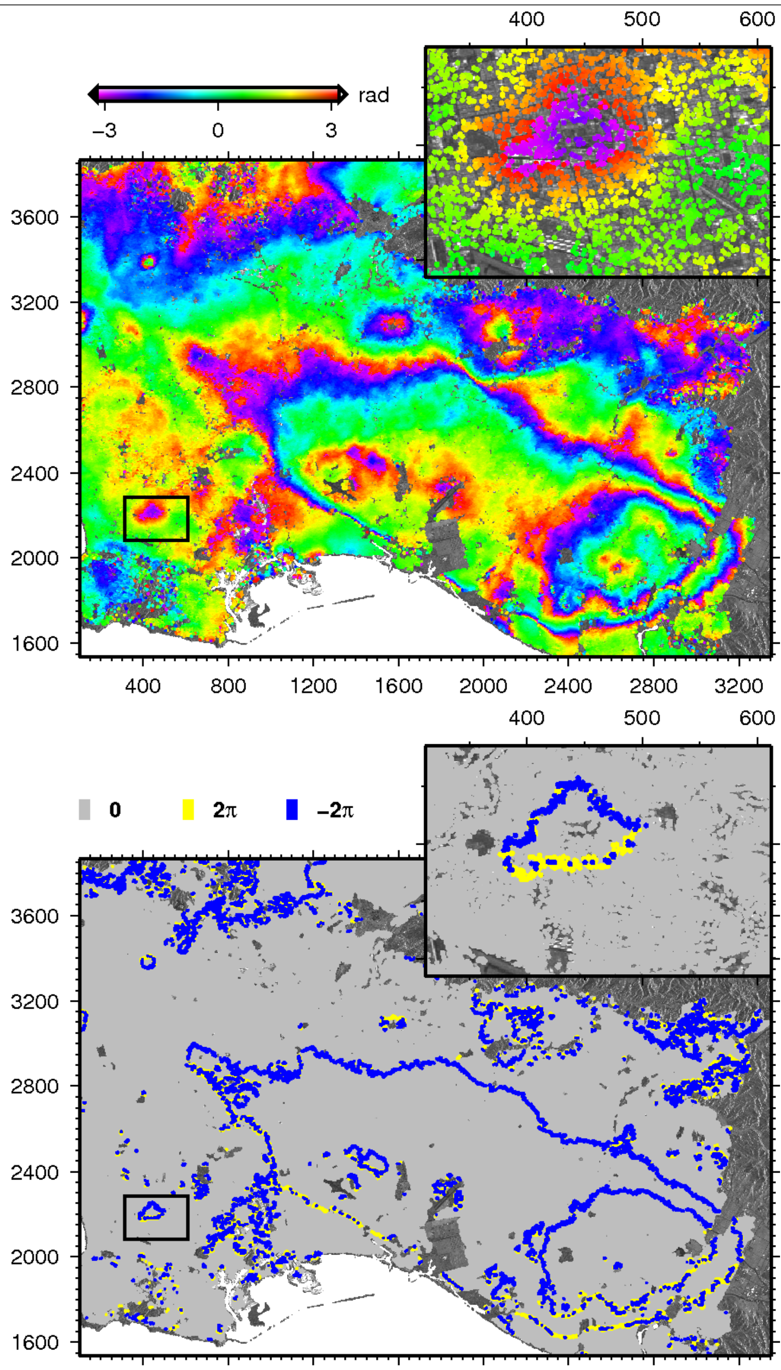

Fig. 5.4: (Top) An InSAR image of 19960406-19971018 and (bottom) phase jumps near the interferometric fringe edges.

The bottom plot in Fig. 5.4 shows the difference between the phase and the wrapped phase at the arcs. The values are represented at the middle points of the arcs. It is clear that all the phase jumps occur at the arcs near the interferometric fringe edges.

5.2.4 TCP Least squares estimator

By selecting interferograms with relatively short spatial and temporal baselines and connecting TCPs with short arcs there will be no phase ambiguity at a large number of the arcs. The deformation rate can then be easily estimated under the framework of least squares as discussed in Chapter 4. It should be noted that TCPInSAR does not rely on the assumption that the true (i.e. unwrapped) phase gradient at all arcs are within $\left(-\pi\,\pi\right]$ Therefore even for areas with rapid subsidence, as long as there are enough coherent points, we can apply TCPInSAR to retrieve deformation signals. There is also no reason to conclude that TCPInSAR technique requires higher point density compared with other multi-tempoal InSAR techniques. In other words, in the areas where other MTInSAR techniques can be successfully applied, the TCPInSAR technique can also work well. After constructing a dense network by the local Delaunay triangulation, we can estimate the parameters from arcs and remove arcs having phase ambiguities. In addition, considering the fact new sensors (e.g. TerraSAR-X and COSMO-Skymed, and future Sentinel-1) can acquire data in rather short repeat intervals, the estimation of phase ambiguities is becoming less necessary in multi-temporal InSAR techniques.

After the LOS linear deformation rate has been resolved from a network with dense and short arcs, we only need focus on retrieving the non-linear components from the least squares residuals in order to determine the full-resolution time series deformation. Since there is no phase ambiguity at the remaining arcs, it is safe to integrate the residuals with respect to a reference point to get the absolute phase residuals. To mitigate the effects of atmospheric errors, it is necessary to apply a spatial and temporal filtering on these phase residuals (Ferretti et al., 2000; Berardino et al., 2001; Mora et al., 2003; Blanco et al., 2008). However when designing the filter, the selection of optimized window length (i.e., the triangular window length for the temporal filter and the averaging window length for the spatial filter) is never an easy task, which largely depends on operator's experience. Once the phase residuals are filtered, the basic observation function for non-linear rate estimation can be written as

$$\boldsymbol{\varphi}_{res} = \boldsymbol{\beta}\,\boldsymbol{v}_{non} + \boldsymbol{w}_{res} \tag{5.2}$$

where $\boldsymbol{\varphi}_{res}$ is the phase residual vector, $\boldsymbol{\beta}$ is the design matrix, $\boldsymbol{v}_{non}$ is the non-linear rate vector containing non-linear rates between time-adjacent acquisitions, and $\boldsymbol{w}_{res}$ is the noise vector in the phase residuals. The non-linear rates are still resolved by least squares. For a given TCP, the final full resolution deformation rates ($\boldsymbol{v}_{full}$) is the sum of linear deformation rate ($\boldsymbol{v}_{linear}$) and non-linear deformation rates ($\boldsymbol{v}_{non}$) i.e.,

$$\boldsymbol{v}_{full} = \boldsymbol{v}_{linear} + \boldsymbol{v}_{non} \tag{5.3}$$

As a summary the steps involved in the TCPInSAR processing are shown in Fig. 5.5

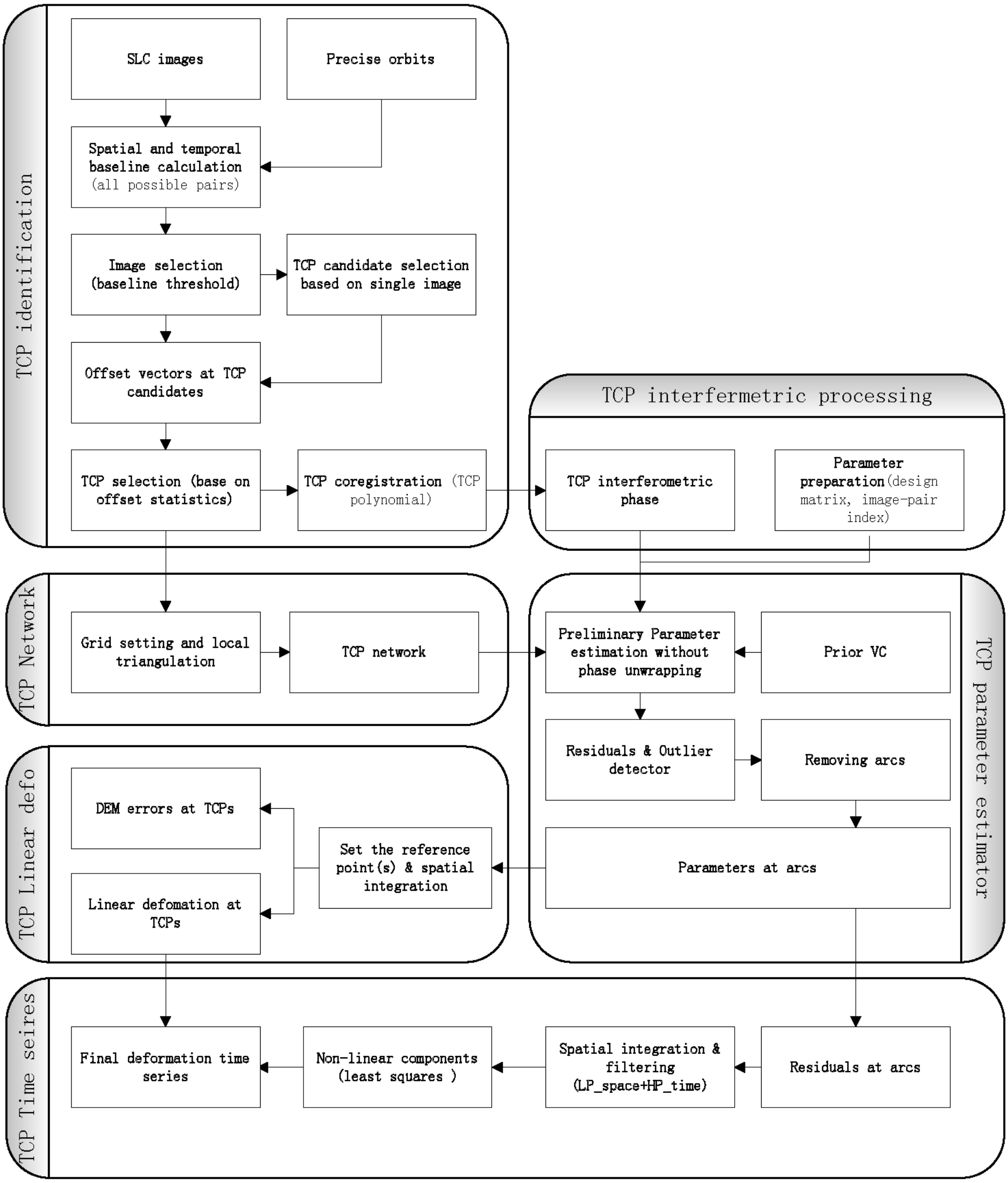

Fig. 5.5: Flow diagram of the TCPInSAR processing chain.

5.3 Results

5.3.1 Linear deformation

The line-of-sight (LOS) linear deformation rate of TCP (Fig. 5.6) was first calculated. To make a visualized comparison with the result estimated by SBAS method , we also select the GPS site ELSC from SCIGN as the reference point. The overall pattern of the estimated deformation rate map is consistent with the results presented in (Casu et al., 2006; Lanari et al., 2004), both of which were resolved from unwrapped phase measurements. The deformation rate map also confirms the conclusion reached by Bawden et al. (2001). In Los Angeles basin long-term deformation rate ranges roughly from 2 mm/yr to 16 mm/yr. Several factors, such as oil and gas extraction, changes in groundwater storage, unrecoverable inelastic compaction as well as the movement of active faults, are known to contribute to the deformation (Argus et al., 2005;Bawden et al., 2001). The largest linear deformation rate (up to 16 mm/yr) occurred in the Wilmington oil field which is the largest oil field in the Los Angeles Basin (Fig. 5.6). The contrast in displacement rate (Fig. 5.7) is apparent at two sides of Newport-Inglewood fault (NIF) which forms the western margin of the Los Angeles basin and has been identified as an active fault zone capable of generating damaging earthquakes. The focal mechanisms and the results of the stress inversion indicate that stress fields along the north and south segments of NIF are different which may be related to an increase in both north-south and east-west horizontal stresses (Hauksson, 1987; Shaw and Suppe, 1996; Yeats, 1973). The increase in horizontal stress can cause uplift along the fault which is confirmed by the high density of measurements of LOS uplift rates ranging from 0.4 to 2.4mm/yr along the west side of NIF (Fig. 5.7). However it should be noticed that since deformation within the Los Angeles basin is complicated by anthropogenic contribution to the overall tectonic signal (Bawden et al., 2001). Using GPS and InSAR measurements jointly to determine the tectonic contraction across Los

Angeles, Bawden et al. (2001) conclude that much of the deformation near the NIF is associated with groundwater pumping rather than slip.

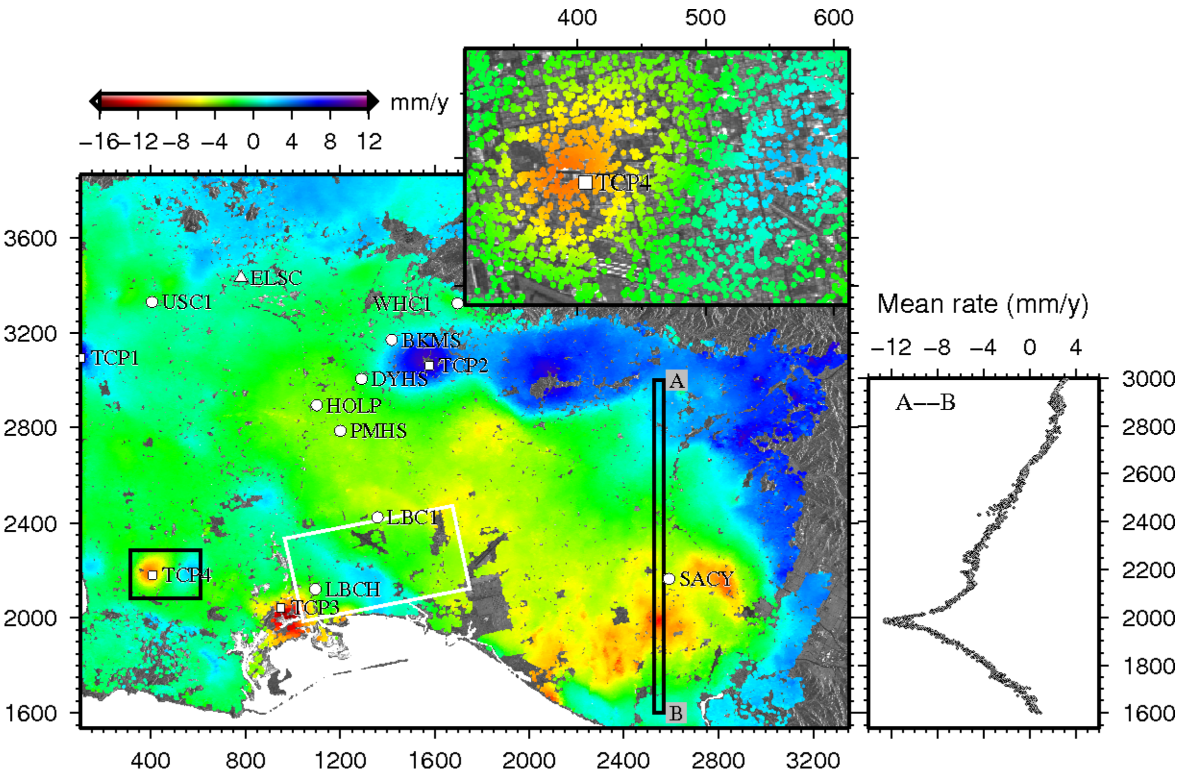

Fig. 5.6:The long-term deformation rate estimated by TCPInSAR technique. The white triangle stands for the reference point and the white dots are the GPS sites used for validation. The white saquares are TCPs located in oilfieds. The inset shows the deformation rate in the black rectangular area. Deformation rate across profile A-B is also shown. The white box outlines an area in NIF.

5.3.2 Short Arc vs. Long Arc

As mentioned previously, shorter arcs have better performance when modeling areas with complex deformation. To understand the effect of arc length on the estimated deformation rate we have conducted here a comparison between the results from longer arcs and short ones. During the network construction, we relax the patch size from 500 m to 1500 m and then perform the local Delaunay triangulation. About 4.9% arcs are longer than 500 m. The difference of deformation rates estimated from these two networks is shown in Fig. 5.8. We can find that generally the results from network with longer arcs underestimate the subsidence. Especially in the Wilmington oil field that suffers large subsidence, the longer arcs can result in an underestimate of subsidence by ~6 mm/yr. This underestimation is mainly due to the seasonal deformation of the Los Angeles basin, which results from periodic groundwater extraction and replenishment (Bawden et al., 2001). The larger seasonal oscillation can be seen at longer arcs (Fig. 5.3), which can bias the least squares estimation. Therefore, in areas with complex spatial-temporal deformation patterns, it is recommended to use relatively short arcs for linear deformation rate estimation.

5.3.3 Solution with smaller dataset

Since the TCPs can be identified interferogram by interferogram, it provides us an opportunity to estimate the deformation parameters with a smaller set of images. This is important for estimating ground surface deformation in areas lacking abundant SAR data. Considering the seasonal oscillation within the Los Angeles basin, we subsample the interferometric observations by a factor of two, resulting in 27 interferograms. The linear deformation rate map estimated from these evenly subsampled interferograms (Fig. 5.9) is in good agreement with the one from all of the selected interferograms. The discrepancy, with a mean of 0.14 mm/yr and a standard deviation of 0.31 mm/yr, suggests that the TCPInSAR approach is also adequate for retrieving deformation signal from a small set of SAR images.

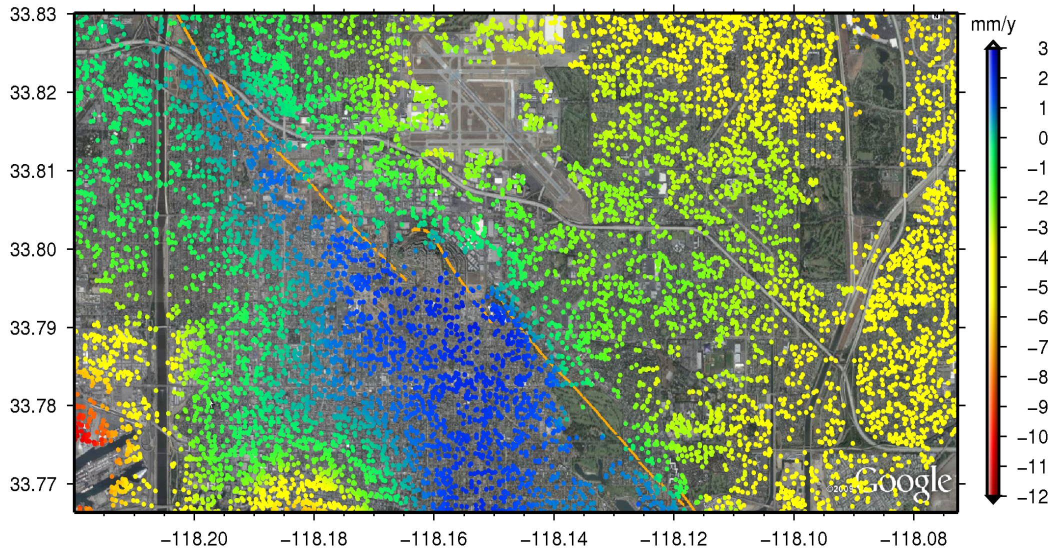

Fig. 5.7:Deformation rates at two sides of Newport-Inglewood fault (the orange line). The scope of the area is shown as in Fig.5.6

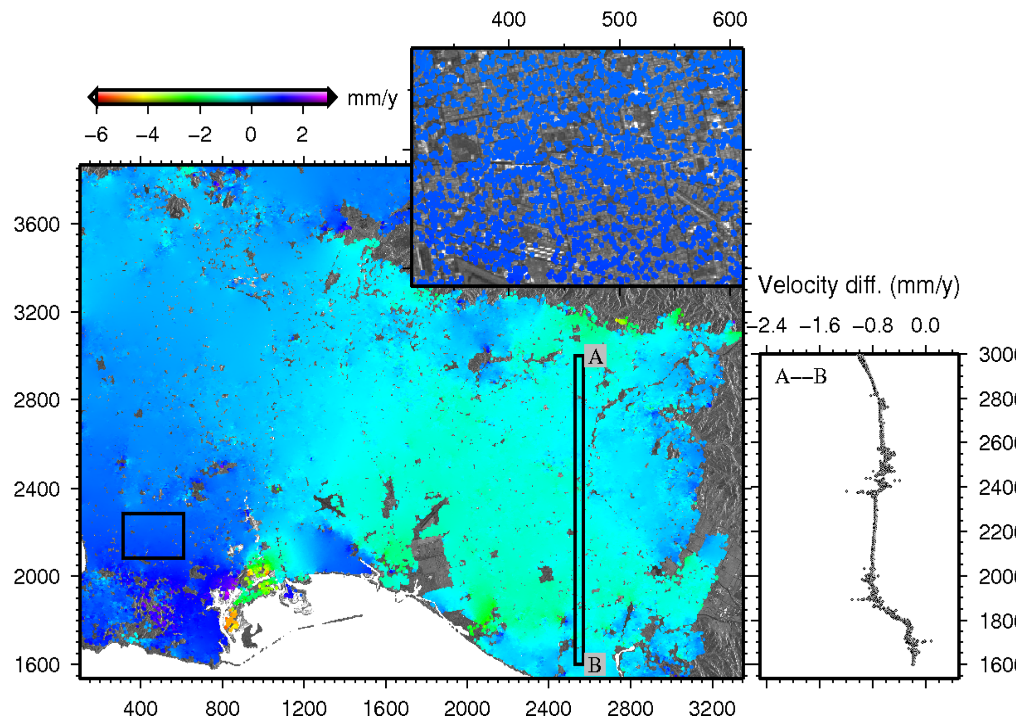

Fig. 5.8:The difference between deformation rates estimated with short-arc network and long-arc network.

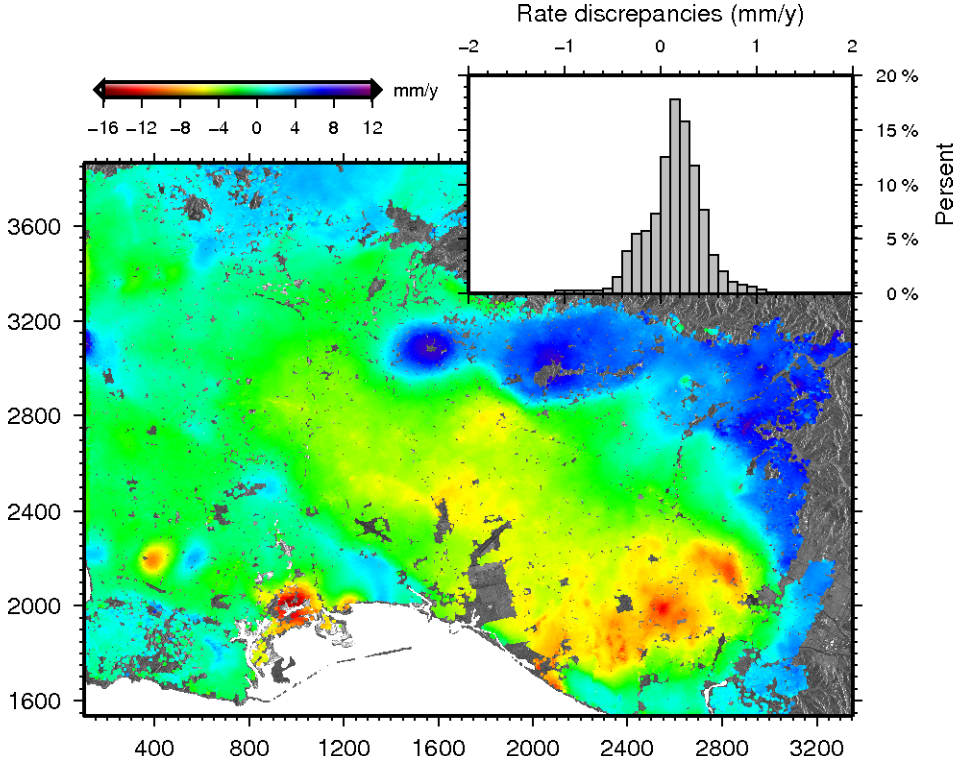

Fig. 5.9:The LOS linear rate map estimated from half sampled interferograms. The inset shows the histogram of deforamtion rate discrepancies compared with those from all the interferograms.

5.3.4 Deformation time series

After the mean (linear) deformation rate has been resolved from a network with dense short arcs, we only need to focus on retrieving the non-linear components from the LS residuals. To determine the full-resolution deformation time series. Space-time filtering is usually performed to suppress the possible effect of the atmospheric delays before estimating the deformation time series. However considering the fact that short arcs have constructed and the periodical deformation pattern in Los Angeles basin is relatively complex, no filtering operation is carried out in this case. The non-linear deformation can be resolved by updating the design matrix and observations in the least squares model. It should be noted that since the GPS observations on the ELSC site started from 1999 only, the time overlap with the selected SAR data is rather limited raising difficulties of unifying the GPS and the TCPInSAR measurements based on this reference site. Therefore when transferring the differential linear and non-linear components at arcs to the parameters at TCPs we select another GPS site USC1 with observations starting from 1994 as the reference site. The final deformation rates between all time-adjacent acquisitions can be obtained by combining the mean and the non-linear deformation rates and the time series of deformation can be obtained according to the deformation rates.

We select 8 GPS sites from the SCIGN network most of which were also used in [Lanari et al., 2004] to validate the estimated result. The GPS measurements have been calculated with respect to the USC1 site. We have calculated the standard deviation of the differences between the TCPInSAR measurements and the corresponding LOS-projected GPS time series (Fig. 5.10). We have selected 32 GPS sites over the study area, all of which have more than 1 year overlapping time with the SAR data (Fig. 5.1). The average standard deviation of the differences is 4.6mm, indicating a good agreement between TCPInSAR-derived time series deformation measurements and daily GPS solutions. Moreover, the deformation at each SAR acquisition time is also compatible with the results presented in [Lanari et al., 2004]. It should be noted that although the InSAR result we estimated is more consistent with GPS observations than that from SBAS method, the improvement has nothing to do with phase unwrapping errors and we believe it mainly comes from the fact that TCPInSAR uses point pairs (arcs) as observations while SBAS uses points. It is clear that point pairs constructed by neighboring TCPs can better suppress the effect of spatially correlated components of atmospheric errors. Besides the GPS sites, we also select 4 TCPs (Fig. 5.6) with large linear deformation rates to investigate their time varying deformation patterns. TCP1 locates near the Inglewood oilfield in Baldwin Hills and shows an upward ground motion due to hydrocarbon recovery effort (Bawden et al., 2001). Uplift trend can also be observed on TCP2 in the Santa Fe Springs oilfield, where fluctuations in surface elevation result from changes in injection rates and declining oilfield operations

(California Department of Conservation, Oil and Gas Statistics, Annual Report, http://www.conservation.ca.gov). TCP3 and TCP4 are in the Wilmington oilfield and experienced an elevation loss of about 60 millimeter from Oct.1995 to Dec. 2000. The deformation time series at TCP3 and TCP4 also indicate that their LOS subsidence rates were occasionally mitigated during the observation time span which might be caused by increasing and realigning water injection (California Department of Conservation, Oil and Gas Statistics, Annual Report, http://www.conservation.ca.gov).

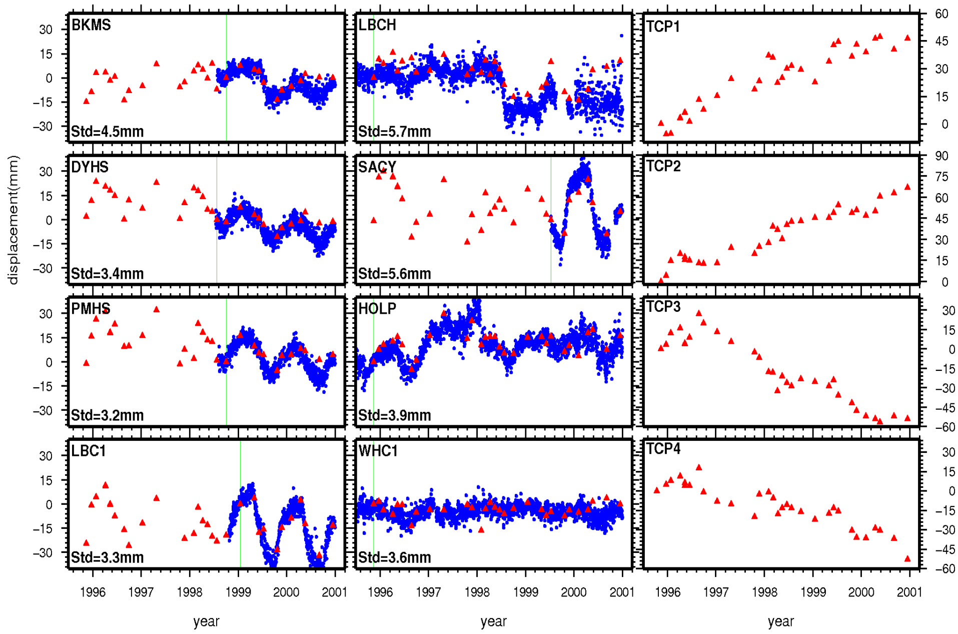

Fig. 5.10:Comparison between TCPInSAR-derived time series deformation and GPS daily observations as well as time varying deformation patterns at 4 TCPs shown in Fig. 5.6. The GPS measurements are first projected onto the LOS direction according to the unit look vector [0.41, -0.09, 0.91] (east, north, up); and then two sets of measurements (InSAR and GPS) are shifted with respect to the same spatial reference point (USC1) and the reference time (i.e., the green lines). The standard deviation of the discrepancies between InSAR and GPS measurements is also reported.

5.4 Conclusions

A multi-temporal TCPInSAR technique, including TCP identification, TCP network and TCP least squares estimator, has been presented in this paper. The technique provides a more reliable way to retrieve ground deformation signals with no need of phase unwrapping. Based on the offset deviation and sub-band SAR image processing, our approach can identify dense coherent points from one image pair only, reducing significantly the requirement on a minimum number (about 20 to 30) of SAR images in most PSInSAR processing methods. With local triangulation network, the selected TCPs can be connected extensively with short arcs. Under the framework of least squares the deformation rate can be estimated from a set of wrapped interferograms. A special attention in TCPInSAR processing is to select proper threshold for the arc length. In areas undergoing complex deformation, if coherent points are densely selected, shorter arcs will render more reliable solutions. However using too short arcs has a risk of separating the network into several blocks, preventing the solution with one reference point. According to the density of TCP and the phase gradient in the interferograms an adaptive arc connection strategy might be a better choice. Finally, we have applied the TCPInSAR technique to retrieve the long-term ground motion in Los Angeles basin. The performance of our method has been examined by the comparison with GPS observations and the previous InSAR results that utilized unwrapped interferograms.

The TCPInSAR measurements, including the linear deformation rate as well as deformation time series, indicate that the deformation pattern in the Los Angeles basin is dominated by the motion associated with seasonal oscillation of ground water table, and the long term anthropogenic deformation related to activities such as oil pumping, water withdrawal and re-injection as well as tectonic motion of both surface and blind thrust faults. The estimated deformation maps with high spatial resolution are expected to be helpful to assess the earthquake hazards for metropolitan Los Angeles.

6 Deformation Rate Estimation on Changing Landscapes

In areas undergoing large scale redevelopments like the cities in most developing countries there are abundant scatterers that are only partially coherent in the observation period. In fact these scatterers still carry high-quality phase information at least in a subset of interferograms allowing us to estimate the deformation rates from them. Here the partially coherent scatterers as well as the persistently coherent scatterers are termed as Temporarily Coherent Points (TCPs). In this chapter we demonstrate the performance of the proposed TCPInSAR method on the retrieval of deformation rates from both persistently and partially coherent points.

6.1 Introduction

There are many urban areas especially in developing countries, undergoing surprisingly rapid development. Urbanization makes the appearance of these areas change frequently, raising difficulties to identify abundant persistently coherent scatterers and thereby hampering us to make better risk assessment over these areas. In fact on these changing landscapes although many scatterers can not keep consistently coherence during the whole observation time span, they still carry high-quality phase signals at least in a certain period, which can be used for deformation estimation. The coherent points on changing landscapes can basically be classified into two types. One type is the persistently coherent scatterers (e.g., PS) and the other type is partially coherent points. Both of these points hereafter are referred to as Temporally Coherent Points (TCPs). Since the coherent point selection method proposed in Chapter 3 can be performed on a single image pairs, under the multi-temporal framework it can be conveniently used to select the TCPs. In this chapter the TCPInSAR method is applied to the retrieval of deformation rate over the southern part of Macao SAR China (Fig. 6.1) which has experienced rapid development in the past ten years.

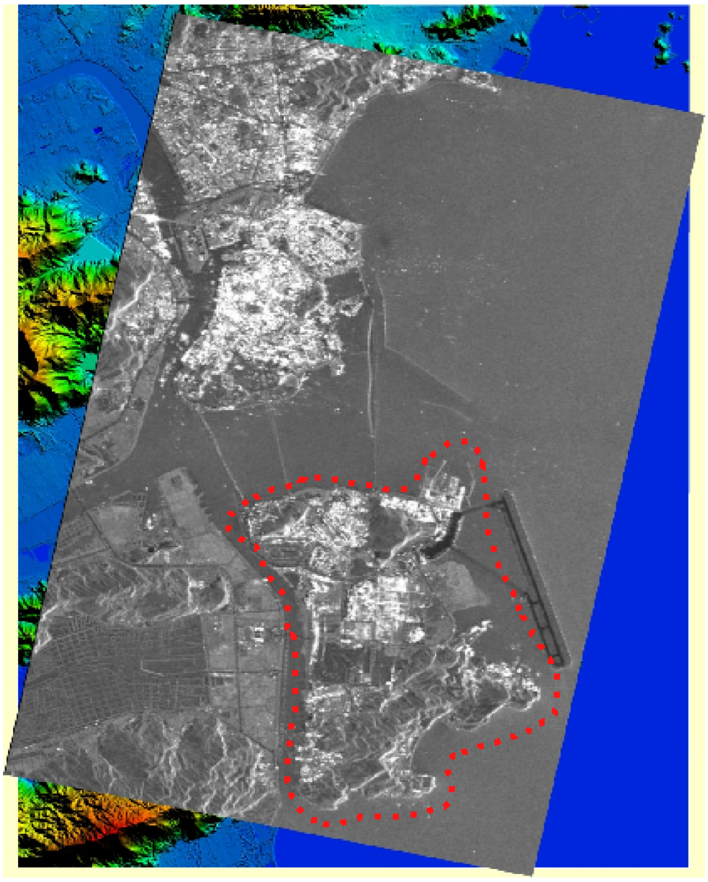

Fig. 6.1: Coverage of the SAR data. The area indicated by the red dots is the test site.

6.2 Data selection

Over the test site we selected 81 interferograms from 38 Envisat/ASAR images acquired in the period of 2003-2010 with a maximum spatial baseline of 300m, a maximum temporal baseline of 250 days. From the generated interferograms, the temporal evolution of the landscapes can be clearly seen. For example, Fig. 6.2 shows two interferograms generated by two image pairs acquired in 2003 and 2009 respectively. In 2003 the land indicated by the black box was just occupied by grass and sands, maintaining very low coherence (i.e., there is no visible signal in the interferometric phase). In the flowing years many buildings have been put up in that area resulting in a rather high coherence in 2009.

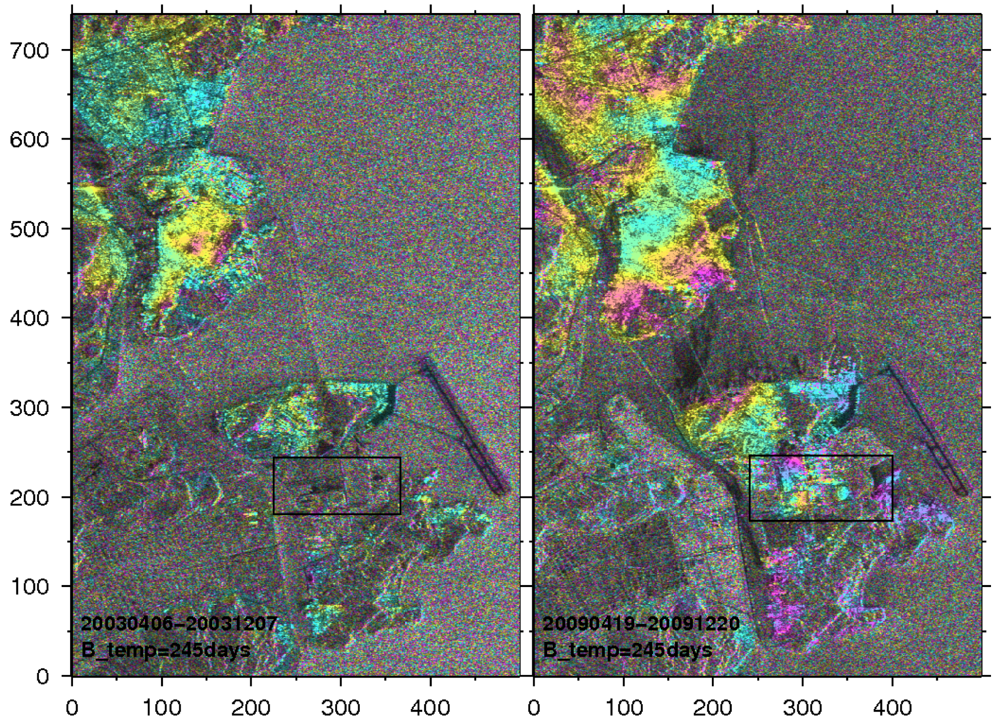

Fig. 6.2: Interferograms generated by image pairs acquired in 2003 (left) and 2009(right). The area included in the box shows an improvement of interferometric quality duo to the renewal of the land.

6.3 TCP selection

Based on the method presented in Chapter 3, the coherent points in an image pair can be identified. Considering a set of SAR images, we can identify the coherent points in each selected image pairs and we also get the exact information on in which image pairs these points keep coherent. Therefore it is not difficult to identify the points that are coherent in more than a certain percent (say,60%) of image pairs. By doing this, more points can be picked up for deformation rate estimation compared with the conventional multi-temporal InSAR techniques where only the persistently coherent points are employed. It should be noted that since some of TCPs keep coherent in a subset of images, it is impossible to get a full-resolution deformation time series on them. Instead we just take the deformation rate as the parameter to be estimated. Over the test site the TCPs selected by the offset deviation method that keep coherent in more than 42 (~52%) out of 81 interferograms are shown in Fig.6.3 (A). As a comparison, the points selected based on coherence map are shown in Fig. 6.3(B). As mentioned before since we exactly know in which interferograms these points keep coherent, we can build up a coherence index for the selection of interferograms where two points at the given arc keep coherent simultaneously. The selection of interferograms is illustrated in Fig. 6.4.

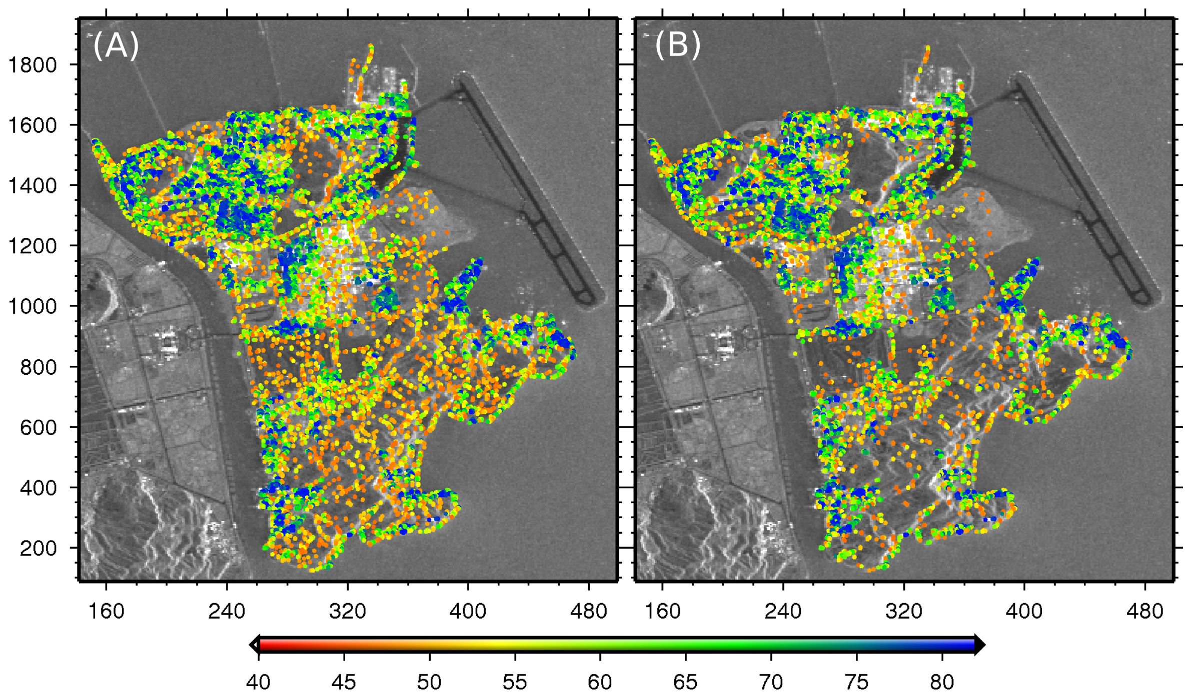

Fig. 6.3: The location of TCPs selected by offset derivation (A) and coherence threshold (B).

6.4 Deformation rate estimation

Once the observation vector is obtained for a given arc, the parameters can be estimated by the method presented in Chapter 4. The retrieved LOS linear deformation rate is shown in Fig.6, which has been validated by the ground measurements provided by DSCC of Macau.

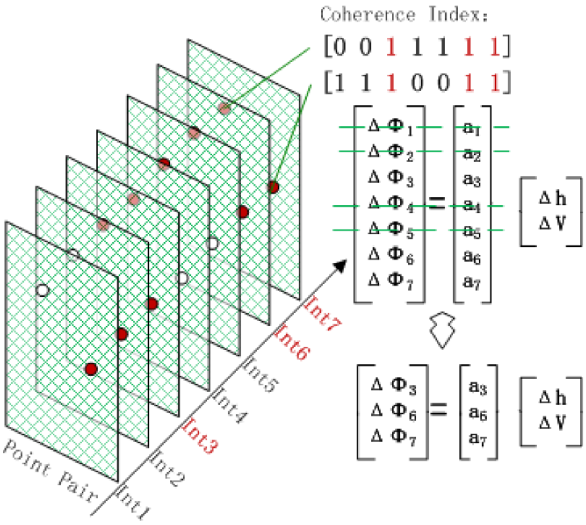

Fig. 6.4: Illustration of interferogram selection for an arc before the parameter estimation

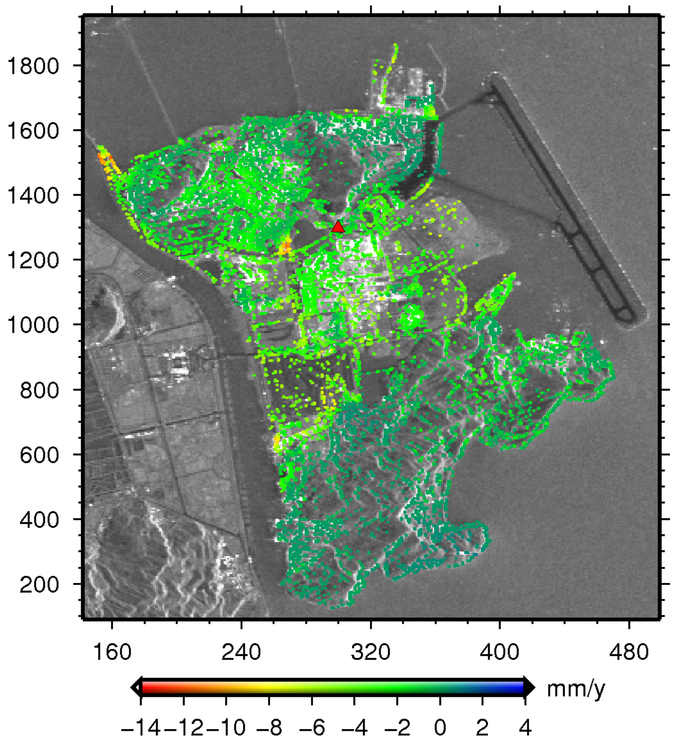

Fig. 6.5: LOS deformation rate over southern part of Macau estimated by least squares with ambiguity detector.

6.5 Conclusions

On changing landscapes, there are abundant scatterers that are not consistently coherent. However these scatterers still carry high quality phases in a subset of interferograms which can be used for the retrieval of deformation rates. In order to identify both the persistently coherent points and partially coherent points and reliably estimate the deformation rate at these points, before the application of the approach presented in Chapter 4, a coherent index should be first generated to select proper interferometric pairs. The method has been applied to the southern part of Macau and the estimated deformation rate map has been validated by the ground measurements.

7 Conclusions and Recommendations

MT-InSAR has proven to be useful in estimating the long term deformation rate and time varying deformation patterns in tectonically active areas as well as urban areas. The existing MT-InSAR algorithms have however some deficiencies that often limit their applications. First, the temporarily coherent points, as the basic observations of all MT-InSAR algorithms, cannot be reliably identified based on a small set of SAR data. Second, phase unwrapping is required to estimate the deformation parameters, while the success of phase unwrapping can hardly be guaranteed. Finally the current MT-InSAR algorithms cannot deal with orbital errors efficiently.

The goals of this dissertation are thus two-fold, to provide an alternative approach for identifying coherent points that are not necessarily to be coherent during the whole time span of observations and to develop an efficient algorithm to estimate the deformation parameters with no need of phase unwrapping.

7.1 Contributions

Since only coherent points carry useful information for MT interferometric analysis, an effective algorithm for identifying these coherent points is a prerequisite for any MT-InSAR methods. While several algorithms for this purpose are available, there currently exits no algorithm that works effectively for a small set of SAR data.

An algorithm for identifying temporarily coherent points has been developed in Chapter 3. The proposed algorithm has a number of important features. First, statistical information on the range and the azimuth offsets of InSAR pairs is used for separating the coherent points from the distributed ones. Second, coregistration of TCPs is optimized to achieve better coregistration accuracy. Third, the parameters used for TCP selection can be easily determined and without relying heavily on experience. Finally, the algorithm can be reliably performed with a small set of SAR data (as few as two).

The development of the new algorithms for estimating the deformation parameters efficiently from phases of TCPs is the central theme of the thesis and represents the most significant contribution of the research. To improve the efficiency and reliability of parameter estimation by avoiding phase unwrapping, the algorithm focuses on neighboring point pairs (arcs) in the interferograms with short spatial and temporal baselines. To increase the density of arcs the triangulation of the TCPs is performed locally. During the parameter estimation, an outlier detector is designed to remove arcs that have phase ambiguities according to the LS residuals. When SAR data have obvious orbital errors, a simple but more precise method for eliminating the effects of orbital error on parameter estimation is proposed, which is almost immune from the effects of the atmospheric artifacts and phase unwrapping errors. All the algorithms have been verified by simulated data sets. Note that the algorithms presented in Chapter 4 for parameter estimation can be employed by other MT-InSAR methods (e.g. PSI).

Finally we applied the TCPInSAR technique to determine the long term linear deformation rate and deformation time series over Los Angeles basin. The results obtained are in good agreement with those published ones as well as GPS results from the SCIGN, indicating the effectiveness of the TCPInSAR in retrieving deformation signals from muti-temporal SAR data.

7.2 Recommendations for future research

There are several possible areas for further research based on this topic. They may include efforts aimed at:

1. **Improving the efficiency of network construction.** Local triangulation is quite easy to be performed but not efficient, since for each grid node, the TCPs located in a circle with a radius of certain length have to be searched. Take the case of Los Angeles for example, the construction of 1,176,922 arcs from 201,778 TCPs takes about 5 hours using a laptop with Intel core2 duo CPU (T9600 @ 2.8GHz 2.8GHz) and 4 GB memory. We notice that there is usually too much redundancy in the constructed arcs. If we only connect the TCP with its N nearest TCPs, the redundant computations might be reduced.

2. **Precise VCE.** During the variance component estimation in the TCPInSAR technique, we only estimated one variance for each image. This is obviously inadequate to describe the noise feature of the image. With the rather abundant arcs, more variance components can be estimated. The appropriate number of variance components to be estimated for an image with due consideration of the quality of the stochastic model and the computation burden still requires further research.

3. **Robust TCPInSAR.** In our original TCPInSAR technique, we employ the LS technique to estimate the deformation parameters and design an outlier detector to remove arcs having phase ambiguities. One drawback of this strategy is the density of arcs might be reduced which will possibly result in isolated sub-networks. The criterion used for choosing high quality arcs is rather strict and can be relaxed to some extent. It has been noticed that given an arc with a series of observations, even though some of observations contain large errors (e.g., phase ambiguities and/or orbital error) it is still possible to estimate the right parameters with a proper estimator. The least absolute deviation (LAD) based estimator may be a potential

choice. LAD or L1 method is widely known as an alternative to the classical least squares (LS) or the L2 method for statistical analysis of linear models. Instead of minimizing the sum of squared errors, it minimizes the sum of the absolute values of the errors. Unlike the LS method, the LAD method is not sensitive to outliers and produces robust estimates. In fact L-1 method has already been used to improve the SBAS technique to reduce the effect of phase unwrapping errors [Lauknes et al., 2011].

4. **Atmospheric signals.** All current solutions for deformation time series depend on the filtering of atmospheric artifacts. When the “true” atmospheric signal fails to meet the basic assumptions of the filter and/or the deformation pattern is complex, the time series of deformation estimated from the filtered residuals may not be optimized and precise. Therefore how to estimate the atmospheric signals accurately still deserves further investigation.

References

Adam, N. (2004), Development of a scientific permanent scatterer system: Modifications for mixed ERS/ENVISAT time series, *ENVISAT & ERS Symposium, Salzburg, Astria*, 6-10 September, 2004, pp. 1-9 (cdrom).

Adam, N., and R. Bamler (2005), Parametric estimation and model selection based on amplitude-only data in PS-interferometry, *in Proceedings of Fringe 2005 Workshop, European Space Agency*.

Adam, N., and A. Parizzi (2009), Practical persistent scatterer processing validation in the course of the Terrafirma project, *Journal of Applied Geophysics*.

Agram, P. S., and H. A. Zebker (2009), Sparse Two-Dimensional Phase Unwrapping Using Regular-Grid Methods, *IEEE Geoscience and Remote Sensing Letters*, *6*(2), 327-331, doi:10.1109/LGRS.2009.2012445.

Amelung, F., S. Jónsson, H. Zebker, and P. Segall (2000), Widespread uplift and “trapdoor” faulting on Galápagos volcanoes observed with radar interferometry, *Nature*, *407*(6807), 993-996.

Argus, D. F. (2005), Interseismic strain accumulation and anthropogenic motion in metropolitan Los Angeles, *Journal of Geophysical Research, 110*(B4), 1-26, doi:10.1029/2003JB002934.

Arikan, M., F. V. Leijen, L. Guang, and R. Hanssen (2007), Improved image alignment under the influence of elevation, in *Proceedings of Fringe 2007 Workshop, European Space Agency*.

Bamler, R. (2000), Interferometric stereo radargrammetry: absolute height determination from ERS-ENVISAT interferograms, in *International Geoscience and Remote Sensing Symposium, IGRASS'00,* pp. 742-745.

Barber, C. B., D. P. Dobkin, and H. Huhdanpaa (1996), The quickhull algorithm for convex hulls, *ACM Transactions on Mathematical Software*, *22*(4), 469-483, doi:10.1145/235815.235821.

Bawden, G., W. Thatcher, and R. Stein (2001), Tectonic contraction across Los Angeles after removal of groundwater pumping effects, *Nature, 412, 812-815.*

Berardino, P., G. Fornaro, R. Lanari, and E. Sansosti (2002), A new algorithm for surface deformation monitoring based on small baseline differential SAR interferograms, *IEEE Transactions on Geoscience and Remote Sensing*, *40*(11), 2375-2383, doi:10.1109/TGRS.2002.803792.

Brooks, B. A., M. A. Merrifield, J. Foster, C. L. Werner, F. Gomez, M. Bevis, and S. Gill (2007), Space geodetic determination of spatial variability in relative sea level change, Los Angeles basin, *Geophysical Research Letters*, *34*(1), 1-6, doi:10.1029/2006GL028171.

Casu, F., M. Manzo, and R. Lanari (2006), A quantitative assessment of the SBAS algorithm performance for surface deformation retrieval from DInSAR data, *Remote Sensing of Environment*, *102*(3-4), 195-210, doi:10.1016/j.rse.2006.01.023.

Colesanti, C., A. Ferretti, F. Novali, C. Prati, and F. Rocca (2003), SAR monitoring of progressive and seasonal ground deformation using the permanent scatterers technique, *IEEE Transactions on Geoscience and Remote Sensing*, *41*(7), 1685-1701, doi:10.1109/TGRS.2003.813278.

Constantini, M. (1998), A Novel Phase Unwrapping Method Based on Network Programming. *IEEE Transactions on Geoscience and Remote Sensing*, 36(3), 813-821. doi: 10.1109/36.673674.

Ding, X.L., Z.W. Li, J.J. Zhu, G.C. Feng, and J.P. Long (2008), Atmospheric Effects on InSAR Measurements and Their Mitigation, *Sensors*, *8*(9), 5426-5448, doi:10.3390/s8095426.

Feng, G.C., E. A. Hetland, X.L. Ding, Z.W. Li, and L. Zhang (2010), Coseismic fault slip of the 2008 Mw 7.9 Wenchuan earthquake estimated from InSAR and GPS measurements, *Geophysical Research Letters*, *37*, L01302, doi:10.1029/2009gl041213.

Ferretti, A., A. Monti-Guarnieri, C. Prati, and F. Rocca (2007), *InSAR Principles: Guidelines for SAR Interferometry Processing and Interpretation*, ESA Publications.

Ferretti, A., C. Prati, and F. Rocca (2001), Permanent scatterers in SAR interferometry, *IEEE Transactions on Geoscience and Remote Sensing*, *39*(1), 8-20, doi:10.1109/36.898661.

Ferretti, A., C. Prati, and F. Rocca (2000), Nonlinear subsidence rate estimation using permanent scatterers in differential SAR interferometry, *IEEE Transactions on Geoscience and Remote Sensing*, *38*(5), 2202-2212, doi:10.1109/36.868878.

Ferretti, A., C. Prati, and F. Rocca (2001b), Permanent scatterers in SAR interferometry, *IEEE Transactions on Geoscience and Remote Sensing*, *39*(1), 8-20, doi:10.1109/36.898661.

Fornaro, G., and M. Manunta (2005), Advances in multipass SAR image registration, in *Internatinal Geoscience and Remote Sensing Symposium, IGARSS'05*, pp. 4832-4835.

Gabriel, A. K., R. M. Goldstein, and H. A. Zebker (1989), Mapping small elevation changes over large areas - Differential radar interferometry, *Journal of Geophysical Research*, *94*(B7), 9183-9191.

Gatelli, F., A. M. Guamieri, F. Parizzi, P. Pasquali, C. Prati, and F. Rocca (1994), The wavenumber shift in SAR inferometry, *IEEE Transactions on Geoscience and Remote Sensing*, *32*(4), 855-865, doi:10.1109/36.298013.

Gray, A. L., K. E. Mattar, P. W. Vachon, R. Bindschadler, K. C. Jezek, R. Forster, and B. Polar (1998), InSAR Results from the RADARSAT Antarctic Mapping Mission Data:Estimation of Glacier Motion using a Simple Registration Procedure, in *Internatinal Geoscience and Remote Sensing Symposium, IGARSS'98*, pp. 1638-1640.

Hanssen, R. F. (2001), *Radar Interferometry: Data Interpretation and Error Analysis*, Kluwer Academic Publishers.

Hauksson, E., and L.M Jones (1989), The 1987 Whittier Narrows Earthquake Sequence in Los Angeles, Southern California: Seismological and Tectonic Analysis, *Journal of Geophysical Research*, 94(B7), 9569–9589, doi:10.1029/JB094iB07p09569.

Hauksson, E. (1990), Earthquakes, Faulting, and Stress in the Los Angeles Basin, *Journal of Geophysical Research*, *95*(B10), 15365-15394, doi:10.1029/JB095iB10p15365.

Hauksson, E., L.M. Jones, and K. Hutton (1995), The 1994 Northridge earthquake sequence in California-seismological and tectonic aspects. *Journal of Geophysical Research-Solid Earth, 100*, 12335-12355.

Hooper, A. (2004), A new method for measuring deformation on volcanoes and other natural terrains using InSAR persistent scatterers, *Geophysical Research Letters*, *31*(23), 1-5, doi:10.1029/2004GL021737.

Hooper, A. (2008), A multi-temporal InSAR method incorporating both persistent scatterer and small baseline approaches, *Geophysical Research Letters*, *35*(16), 1-5, doi:10.1029/2008GL034654.

Hooper, A., and H.A. Zebker (2007), Phase unwrapping in three dimensions with application to InSAR time series., *Journal of the Optical Society of America. A, Optics, image science, and vision*, *24*(9), 2737-47.

Jia, P. Z. (1984), *Optimal estimation and its applications*, Science Press, Beijing, China.

Kampes, B. M., and R. F. Hanssen (2004), Ambiguity resolution for permanent scatterer interferometry, *IEEE Transactions on Geoscience and Remote Sensing*, *42*(11), 2446-2453, doi:10.1109/TGRS.2004.835222.

Kampes, B. M. (2006), *Radar interferometry : persistent scatterer technique*, Springer.

Koch, K. R. (1988), *Parameter Estimation and Hypothesis Testing in Linear Models*, Springer.

Lanari, R., P. Lundgren, M. Manzo, and F. Casu (2004), Satellite radar interferometry time series analysis of surface deformation for Los Angeles, California, *Geophysical Research Letters*, 31, L23613, doi:10.1029/2004GL021294.

Lanari, R., O. Mora, M. Manunta, J. J. Mallorqui, P. Berardino, and E. Sansosti (2004), A small-baseline approach for investigating deformations on full-resolution differential SAR interferograms, *IEEE Transactions on Geoscience and Remote Sensing*, *42*(7), 1377-1386, doi:10.1109/TGRS.2004.828196.

Lauknes, T. R., Zebker, H. A., & Larsen, Y. (2011), InSAR deformation time series using an L1-norm small-baseline approach. *IEEE Transactions on Geoscience and Remote Sensing*, *49*(1), 536-546.

Li, B.F. (2009), Theory and Method of Parameter Estimation for Mixed Interger GNSS Stochastic and Function Models, PhD thesis (in Chinese), Tongji University, Shanghai, China.

Li, Z. W., X. L. Ding, C. Huang, G. Wadge, and D. W. Zheng (2006), Modeling of atmospheric effects on InSAR measurements by incorporating terrain elevation information, *Journal of Atmospheric and Solar-Terrestrial Physics*, *68*(11), 1189-1194.

Li, Z. W., X. L. Ding, C. Huang, G. Wadge, and D. W. Zheng (2010), Modeling of atmospheric effects on InSAR measurements by incorporating terrain elevation information, *Journal of Atmospheric and Solar-Terrestrial Physics*, *68*(11), 1189-1194.

Lin, Q., Vesecky, J. F., & Zebker, H. A. (1992), New approaches in interferometric SAR data processing. *IEEE Transactions on Geoscience and Remote Sensing*, *30*(3), 560-567.

Liu, G., S. M. Buckley, X. Ding, Q. Chen, and X. Luo (2009), Estimating Spatiotemporal Ground Deformation With Improved Persistent-Scatterer Radar Interferometry, *IEEE Transactions on Geoscience and Remote Sensing*, *47*(9), 3209-3219, doi:10.1109/TGRS.2009.2028797.

Lu, Z. (1998), Synthetic aperture radar interferometry coherence analysis over Katmai volcano group, Alaska, *Journal of Geophysical Research*, *103*(B12), 29887-29894, doi:10.1029/98JB02410.

Lu, Z., O. Kwoun, and R. Rykhus (2007), Interferometric synthetic aperture radar (InSAR): its past, present and future, *Photogrammetric Engineering and Remote*, *73*(3), 217-221.

Lu, Z., T. Masterlark, D. Dzurisin, R. Rykhus, and C. Wicks JR (2003), Magma supply dynamics at Westdahl volcano, Alaska, modeled from satellite radar interferometry, *Journal of Geophysical Research*, *108*(B7), doi:10.1029/2002JB002311.

Massonnet, D., M. Rossi, C. Carmona, F. Adragna, G. Peltzer, K. Feigl, and T. Rabaute (1993), The Displacement Field of the Landers Earthquake Mapped by Radar Interferometry, *Nature*, *364*(6433), 138-142.

Mattar, K. E., P. W. Wachon, D. Gedtner, A. L. Gray, I. G. Cumming, and M. Brugman (1998), Validation of alpine glacier velocity measurements using ERS tandem-mission SAR data, *IEEE Transactions on Geoscience and Remote Sensing*, *36*(3), 974-984.

Mellors, R.J., H. Magistrale, P. Earle, and A. Cogbill (2004), Comparison of four moderate-size earthquakes in southern California using seismology and InSAR. *Bulletin of the Seismological Society of America*, *94*, 2004-2014.

Michel, R., and E. Ftignot (1999), Flow of Moreno Glaciar, Argentina, from repeat-pass Shuttle Imaging Radar images: Comparison of the phase correlation method with radar interferometry, *Journal Of Glaciology*, *45*(149), 93-100.

Mora, O., J. J. Mallorqui, and a Broquetas (2003), Linear and nonlinear terrain deformation maps from a reduced set of interferometric sar images, *IEEE Transactions on Geoscience and Remote Sensing*, *41*(10), 2243-2253, doi:10.1109/TGRS.2003.814657.

Rao, C., and S. Mitra (1971), *Generalized Inverse of the Matrix and Its Applications*, John Wiley & Sons Inc.

Rott, H., M. Stuefer, and A. Siegel (1998), Mass fluxes and dynamics of Moreno Glacier, Southern Patagonian Icefield, *Journal of Geophysical Research*, *25*, 1407-1410.

Serafino, F. (2006), SAR image coregistration based on isolated point scatterers, *Geoscience and Remote Sensing Letters, IEEE,* 3 (3), 354-358.

Shanker, A. P., and H. Zebker (2010), Edgelist phase unwrapping algorithm for time series InSAR analysis., *Journal of the Optical Society of America A*, *27*(3), 605-612, doi:10.1364/JOSAA.27.000605.

Shanker, P., and H. Zebker (2007), Persistent scatterer selection using maximum likelihood estimation, *Geophysical Research Letters*, *34*(22), 2-5, doi:10.1029/2007GL030806.

Shaw, J., and P. Shearer (1999), An elusive blind-thrust fault beneath metropolitan los angeles, *Science*, *283*(5407), 1516-1518.

Shen, Z.-K., D. D. Jackson, and B. X. Ge (1996), Crustal deformation across and beyond the Los Angeles basin from geodetic measurements, *Journal of Geophysical Research*, *101*(B12), 27957-27980, doi:10.1029/96JB02544.

Strozzi, T., A. Kouraev, A. Wiesmann, U. Wegmüller, A. Sharov, and C. Werner (2008), Estimation of Arctic glacier motion with satellite L-band SAR data, *Remote Sensing of Environment*, *112*(3), 636-645, doi:10.1016/j.rse.2007.06.007.

Strozzi, T., A. Luckman, T. Murray, U. Wegmuller, and C. L. Werner (2002), Glacier motion estimation using SAR offset-tracking procedures, *IEEE Transactions on Geoscience and Remote Sensing*, *40*(11), 2384-2391.

Teunissen, P. (2000), *Adjustment theory: an introduction*. Delft University Press.

Touzi R., A. Lopes, J. Bruniquel, and P.W. Vachon (1999), Coherence estimation for SAR imagery, *IEEE Transactions on Geoscience and Remote Sensing*, *37*(1), 135-149.

Usai, S. (2000), An analysis of the interferometric characteristics of anthropogenic features, *IEEE Transactions on Geoscience and Remote Sensing*, *38*(3), 1491-1497, doi:10.1109/36.843050.

Usai, S. (2003), A least squares database approach for SAR interferometric data, *IEEE Transactions on Geoscience and Remote Sensing*, *41*(4), 753-760, doi:10.1109/TGRS.2003.810675.

Usai, S. , Hanssen, R. F. (1997), Long time scale INSAR by means of high coherence features, *Third ERS Symposium-Space at the Service of our Environment, Florence, Italy, 17-21 March, 1997.* pp. 225-228.

Watson, K. M., Y. Bock, and D. T. Sandwell (2002), Satellite Interferometric Observations of Displacements Associated with Seasonal Groundwater in the Los Angeles Basin, *Journal of Geophysical ResearchSolid Earth*, *107*(B4), art. no.-2074.

Werner, C., U. Wegmuller, T. Strozzi, and a Wiesmann (2003), Interferometric point target analysis for deformation mapping, in *Internatinal Geoscience and Remote Sensing Symposium, IGARSS'03*, pp. 4362-4364.

Williams, S., Y. Bock, and P. Fang (1998), Integrated satellite interferometry: Tropospheric noise, GPS estimates and implications for interferometric synthetic aperture radar products, *Journal of Geophysical ResearchSolid Earth*, *103*(B11), 27051-27067.

Wright, T.J., B. Parsons, P. C. England, and E. J. Fielding, InSAR observations of low slip rates on the major faults of western Tibet, *Science*, vol. 305, no. 5681, pp. 236–239, Jul. 2004.

Yeats, R.S. (1973), Newport-Inglewood fault zone, Los Angeles, California. American Association of Petroleum Geologists Bulletin, 57, 117-135.

Yerkes, R.F., T.H. McCulloh, J.E. Schoellhamer, and J.G. Vedder, (1965). Geology of the Los Angeles Basin, California: An introduction, *U.S. Geology Survey Professional Paper*, 0420-A, A1 – A57.

Zebker, H. A., and P. A. Rosen (1996), Atmospheric Artifacts in Interferometric SAR Surface Deformation and Topograhic Maps, *Journal of Geophysical Research Solid Earth*, *99*(19), 617-634.

Zebker, H. A., P. A. Rosen, R. M. Goldstein, A. Gabriel, and C. L. Werner (1994), On the derivation of coseismic displacement fields using differential radar interferometry: The Landers earthquake, *Journal of Geophysical Research*, *99*(B10), 19617-19634.

Zebker, H. A., and J. Villasensor (1992a), Decorrelation in interferometric radar echoes, *IEEE Transactions on Geoscience and Remote Sensing*, *30*(5), 950-959.

Zebker, H. A., and J. Villasensor (1992b), Decorrelation in interferometric radar echoes, *IEEE Transactions on Geoscience and Remote Sensing*, *30*(5), 950-959.

Zhang, L., J. C. Wu, L. L. Ge, X. L. Ding, and Y. L. Chen (2008), Determining fault slip distribution of the Chi-Chi Taiwan earthquake with GPS and InSAR data using triangular dislocation elements, *Journal of Geodynamics*, *45*(4-5), 163-168, doi:10.1016/j.jog.2007.10.003.

Zhang, L., X.L. Ding, and Z. Lu (2011a), Ground settlement monitoring based on temporarily coherent points between two SAR acquisitions, *ISPRS Journal of Photogrammetry and Remote Sensing*, *66*(1), 146-152, doi:10.1016/j.isprsjprs.2010.10.004.

Zhang, L., X.L. Ding, and Z. Lu (2011b), Modeling PSInSAR time series without phase unwrapping, *IEEE Transactions on Geoscience and Remote Sensing*, *49*(1), 547-556, doi:10.1109/TGRS.2010.2052625.

Zhang, L., X.L. Ding, and Z. Lu (2011c), Deformation rate estimation on changing landscapes using Temporaily Coherent Point InSAR, *Proceedings of Fringe 2011*, Frascati, Italy.

Zhang, L., Z. Lu, X.L. Ding, H.S. Jung, G.C. Feng and C.W. Lee (2012), Mapping ground surface deformation using temporarily coherent point SAR interferometry: application to Los Angeles Basin, *Remote Sensing of Environment*, 117, 429-439.